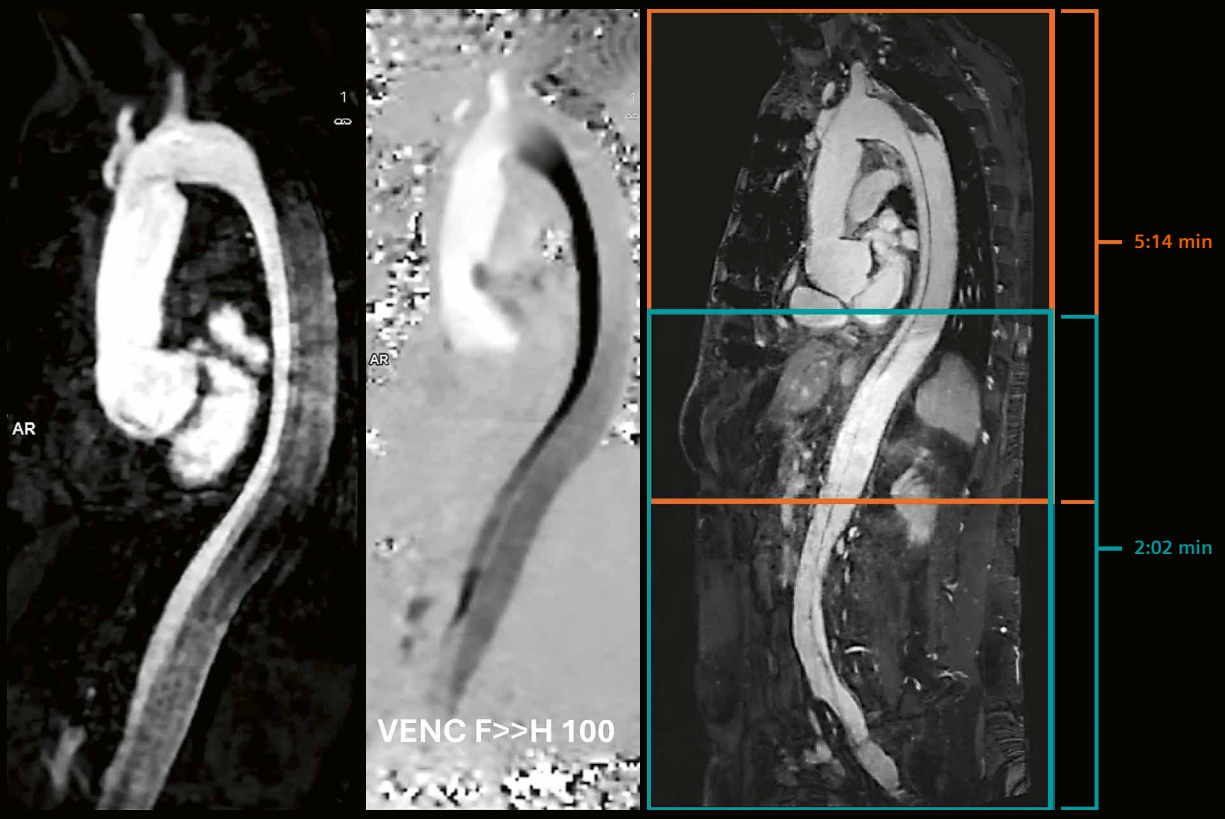

SMRA 2026

Clinical Benefits of MR Angiography

Seeing What We Might Miss: AI-Assisted Inline Detection of Intracranial Aneurysms on TOF-MRA

Bing Tian, et al.
The 1st affiliated hospital of Navy Medical University (Changhai Hospital of Shanghai), Shanghai, China

Imaging Aortic Dissections and Aneurysms with MRI: The Clinical Value of Advanced Angiography and 4D Flow Sequences

Alain Lalande, et al.
Université Bourgogne Europe, Dijon, France

Contrast-Enhanced iNAV MRA for Whole-Chest, Whole-Heart, and Whole-Aortic Imaging: A Single-Center Experience

Jason Craft, et al.
DeMatteis Cardiovascular Institute, St. Francis Hospital & Heart Center, Roslyn, NY, USA

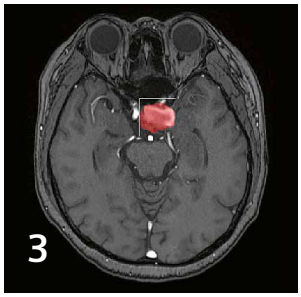

Aneurysm detection[1] as an add-in to the TOF sequence

Asymptomatic severe right MCA M1-segment stenosis

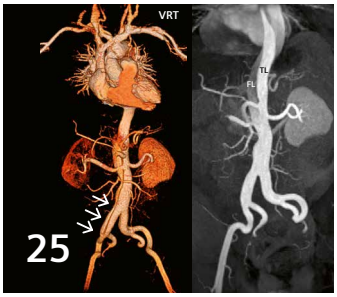

Contrast-enhanced iNAV MRA

Vascular Imaging

3 Seeing What We Might Miss: AI-Assisted Inline Detection[1] of Intracranial Aneurysms on TOF-MRA
Bing Tian, et al.
The 1st affiliated hospital of Navy Medical University (Changhai Hospital of Shanghai), Shanghai, China

6 The Increasing Role of 7T MRI in the Neuroimaging of Cerebral Small Vessel Disease
Zihao Zhang, et al.
State Key Laboratory of Brain and Cognitive Science, Institute of Biophysics, Chinese Academy of Sciences, Beijing, China

12 Depicting the Labyrinthine Artery at 7T: An Ultra-High-Resolution 3D Time-of-Flight Study
Hui Liu, et al.
Siemens Healthineers, China

14 MRA at 7T: Unlocking the Potential of Small Vascular Imaging
Xin Lou, et al.
The First Medical Center, Chinese PLA General Hospital (PLAGH), Beijing, China

Thoracic and Abdominal MRA

17 Imaging Aortic Dissections and Aneurysms with MRI: The Clinical Value of Advanced Angiography and 4D Flow Sequences
Alain Lalande, et al.
Université Bourgogne Europe, Dijon, France

27 Contrast-Enhanced iNAV MRA for Whole-Chest, Whole-Heart, and Whole-Aortic Imaging[1]: A Single-Center Experience
Jason Craft, et al.
DeMatteis Cardiovascular Institute, St. Francis Hospital & Heart Center, Roslyn, NY, USA

42 Non-Contrast Portal Vein Imaging Using *syngo* NATIVE MR Angiography
Marcelo Fernandes Arêas
Siemens Healthineers, Erlangen, Germany

Meet Siemens Healthineers

47 Introducing Jing An
Lead Protocol Developer
Siemens Magnetic Resonance Ltd., Shenzhen, China

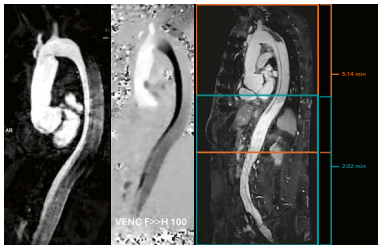

Cover image from Alain Lalande, et al. Imaging Aortic Dissections and Aneurysms with MRI.

[1] *Work in progress. The application is still under development and not commercially available. Its future availability cannot be ensured.*
[2] *The MRI restrictions (if any) of the metal implant must be considered prior to patient undergoing MRI exam. MR imaging of patients with metallic implants brings specific risks. However, certain implants are approved by the governing regulatory bodies to be MR conditionally safe. For such implants, the previously mentioned warning may not be applicable. Please contact the implant manufacturer for the specific conditional information. The conditions for MR safety are the responsibility of the implant manufacturer, not of Siemens Healthineers.*

Seeing What We Might Miss: AI-Assisted Inline Detection of Intracranial Aneurysms on TOF-MRA

Yuxi Hou[1], Caixia Fu[2], Hang Pan[2], Tianxiao Zhang[3], Bing Tian[1]

[1] Department of Radiology, The 1st affiliated hospital of Navy Medical University (Changhai Hospital of Shanghai), Shanghai, China
[2] Frontier Innovation Team, Siemens Shenzhen Magnetic Resonance Ltd., Shenzhen, China
[3] Digital Technology and Innovation, Siemens Healthineers Digital Technology (Shanghai) Co., Ltd., Shanghai, China

Introduction

In our daily practice, time-of-flight magnetic resonance angiography (TOF-MRA) has become one of the most commonly used non-contrast techniques for cerebrovascular screening. It is fast, widely available, and well accepted by patients, especially in routine health examinations and follow-up of suspected vascular disease. Yet every radiologist knows the challenge: Small intracranial aneurysms may be subtle, may arise at complex arterial bifurcations, and may be overlooked when the reading workload is high or image quality varies. Because a missed aneurysm can have serious clinical consequences, we continuously look for tools that can help us read more consistently and with greater confidence.

From clinical need to AI support

To address this clinical need, Siemens Healthineers developed a deep learning solution for automated intracranial aneurysm detection and segmentation on 3D TOF-MRA.[1] The prototype of the aneurysm detection tool[1] is implemented as an add-in attached to the TOF sequence. Once the TOF scan is completed, the add-in automatically launches image analysis to identify potential aneurysms, eliminating the need for a separate post-processing step and making the workflow highly convenient.

From a physician's point of view, the goal is not to replace expert interpretation, but to provide a second set of eyes directly within the imaging workflow. For screening examinations, where sensitivity is particularly important, this kind of inline support could be valuable if it performs reliably across scanners, sites, and patient populations.

[1] *Work in progress. The application is currently under development and is not for sale in the U.S. and in other countries. Its future availability cannot be ensured.*

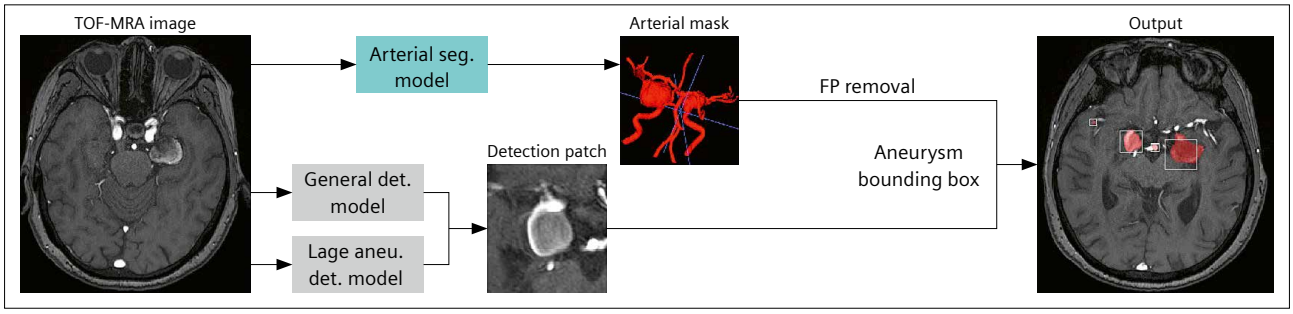

1 A novel 3D deep learning framework with brain vessel constraints [1]. The pipeline consists of three major stages: (1) brain vessel segmentation, (2) aneurysm detection, and (3) false-positive (FP) suppression using vessel priors.

How the model was developed and evaluated

The aneurysm detection model (Fig. 1) was trained using 1,916 3D TOF-MRA scans from patients with at least one unruptured intracranial aneurysm confirmed by experienced radiologists. The development dataset combined images from three clinical sites and public datasets, including ADAM, INSTED2024, and Lausanne, and was divided into training and internal validation sets. All annotations were performed by radiologists with more than five years of TOF-MRA interpretation experience and blinded to patient information. In addition, an internal test cohort from Changhai Hospital included 39 examinations with intracranial aneurysms and 232 examinations without aneurysms, and an external test cohort from RSNA included 555 examinations with intracranial aneurysms and 697 examinations without aneurysms, allowing evaluation in a clinically relevant population with both positive and negative cases.

For us as clinicians, the key question is whether the algorithm can maintain high sensitivity while keeping false positives at a manageable level. In the validation dataset, the model achieved a sensitivity of 96% at two false positives per scan. In the internal test set from Changhai Hospital, it maintained a sensitivity of 95% at two false positives per scan. On the external dataset, the positive predictive value reached 90%, an encouraging result given the screening-oriented setting and the expected challenge of false-positive findings in populations with relatively low disease prevalence. Representative results of aneurysm detection from the validation, internal test, and external test sets are shown in Figure 2. More detailed results can be found in the published ISMRM abstract [1].

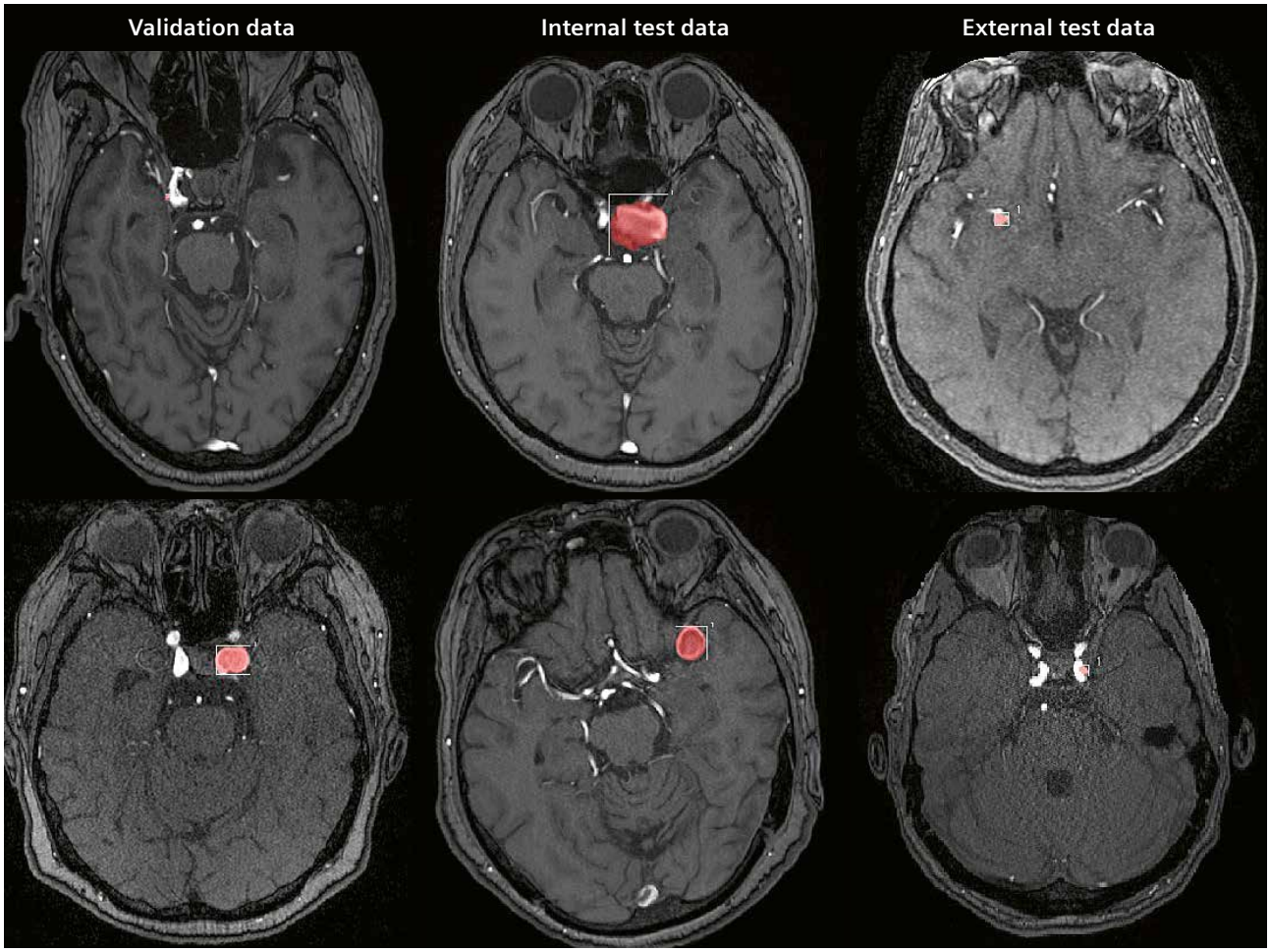

2 Example results of aneurysm detection from the algorithm on validation dataset, internal test dataset, and external test dataset [1]. All six cases are confirmed intracranial aneurysm patients, and the algorithm successfully identified the aneurysmal lesions (marked in red) in each case.

Clinical relevance in routine reading

In a busy reading room, an AI-based aneurysm detection tool may be most helpful when it is integrated seamlessly into the routine TOF-MRA workflow. By highlighting suspicious aneurysm candidates and providing segmentation information, it can draw attention to small or difficult-to-see lesions before the final report is signed. This may be particularly useful for screening examinations, follow-up studies, and cases with complex vascular anatomy. The current results suggest that the prototype has the potential to support radiologists by improving vigilance, reducing oversights, and helping to standardize detection performance across different clinical settings.

Outlook

The next step will be prospective evaluation in real-world clinical workflows. Beyond algorithm performance metrics, future studies should assess reading efficiency, radiologist confidence, case-level decision making, and the practical handling of false-positive findings. For AI to become truly useful in neuroradiology, it must fit naturally into the clinical pathway and provide clear value at the point of care. From this perspective, automated aneurysm detection on TOF-MRA is a promising example of how deep learning can move from technical innovation toward meaningful clinical assistance.

Reference

1 Hou Y, Fu C, Pan H, Lan N, Li H, Zhang T, et al., Deep Learning for Detection of Intracranial Aneurysms on TOF-MRA: A Multi-Center Study with External Validation. Poster session presented at: ISMRM & ISMRT Annual Meeting; 2026 May 9–14; Cape Town, South Africa. Abstract 352-02-016.

Bing Tian, M.D.
Chief Physician of Diagnostic Radiology
Department of Radiology
The First Affiliated Hospital of
Naval Medical University
Changhai Hospital of Shanghai
No. 168 Changhai Road
Shanghai 200433
China
Tel: +86 13818935650
bing.tian@hotmail.com
www.chhospital.com.cn

Contact

Yuxi Hou
Master of Medicine, Attending Physician
of Diagnostic Radiology
The First Affiliated Hospital of
Naval Medical University
Changhai Hospital of Shanghai
No. 168 Changhai Road
Shanghai 200433
China
Tel.: 021-31166666
2279471759@qq.com
www.chhospital.com.cn

The Increasing Role of 7T MRI in the Neuroimaging of Cerebral Small Vessel Disease

Yue Wu[1,2]; Rong Xue[1,2]; Yan Zhuo[1,2]; Zihao Zhang[1,2,3]

[1]State Key Laboratory of Brain and Cognitive Science, Institute of Biophysics, Chinese Academy of Sciences, Beijing, China
[2]University of Chinese Academy of Sciences, Beijing, China
[3]Institute of Artificial Intelligence, Hefei Comprehensive National Science Center, Hefei, China

Introduction

Cerebral small vessel disease (cSVD) is the most common, chronic, and progressive vascular disease [1]. cSVD causes acute symptoms, such as lacunar infarct and intracranial hemorrhage, accounting for 20% of symptomatic strokes. The patients also experience chronic insidious onset, for example, the high prevalence of cSVD in the elderly population was proven to be associated with an increased risk for dementia [2]. Previously, the STandards for ReportIng Vascular changes on nEuroimaging (STRIVE) was proposed to guide the scientific reporting of changes related to cSVD on neuroimaging [3]. It manifests as recent small subcortical infarct, lacune of presumed vascular origin, white matter hyperintensity of presumed vascular origin, perivascular space, cerebral microbleed, and brain atrophy. However, these imaging features were summarized from clinically available 3T and 1.5T MRI scanners. The structure and function of cerebral small vessels, which are directly related to cSVD, could so far not be fully characterized at 3T and lower field strengths. Tiny parenchymal lesions such as cortical microinfarcts are also more difficult to detect at 3T and lower field strength, as spatial resolution can only be pushed to a certain extent in clinical scan times.

In recent years, ultra-high-field (UHF) MRI at 7T has been shown to be effective in diagnosing various neurovascular diseases. Since the signal-to-noise ratio (SNR) of MRI is approximately proportional to the field strength, 7T MRI provides an intrinsic signal-to-noise ratio (SNR) of approximately 2.3 times that of 3T and 4.7 times that of 1.5T, if a linear dependency of SNR to the field strength is assumed. However, literature indicates a supralinear correlation, proportional to B_0 1.65 [4]. Higher SNR supports using higher spatial resolution in the acquisition and enabling the visualization of small vessels and tiny lesions on the brain. On the other hand, relaxation times change as the field strength increases (T1 gets longer and T2 gets shorter), which allows MRI techniques such as angiography based on flow-related enhancement to achieve higher contrast-to-noise ratios (CNRs). Additionally, sequences sensitive to susceptibility effects, such as T2*-weighted imaging and quantitative susceptibility mapping (QSM)[1], benefit from increased susceptibility at 7T, enabling better visualization of venules and microbleeds. These advantages of 7T MRI provide an opportunity to directly evaluate the structure and function of cerebral small vessels.

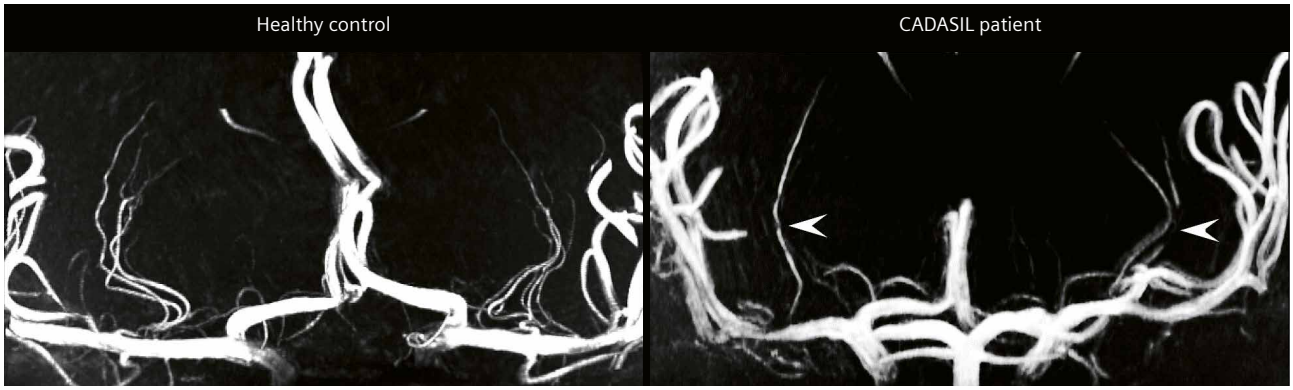

1 Coronal maximum intensity projection of 7T TOF-MRA of a healthy control and a CADASIL patient. The arrowheads point to flow deficits in the lenticulostriate arteries.

[1]*Work in progress. The application is currently under development and is not for sale in the U.S. and in other countries. Its future availability cannot be ensured.*

Angiography

The CNR of TOF-MRA was reported 83% higher at 7T compared to that obtained at 3T [5]. The improved CNR highlighted smaller peripheral vessels, which can be clearly seen at images with high resolution. This in turn allows to e.g. detect stenosis and occlusion in rather small vessels like the lenticulostriate artery (LSA) using 7T TOF-MRA. This finding is a prone cause of cSVD in deep cerebral infarction [6]. On the other hand, the angiography of LSA can be used to assess the establishment of collateral circulation [7]. The vascular density of LSA visualized by 7T TOF-MRA was reported to be comparable to DSA, and significantly superior to 3T TOF-MRA [8].

The visualization of intracranial perforating arteries such as LSA by 7T TOF-MRA expands the horizon for *in vivo* imaging studies of cSVD. In patients with hypertension, the number of stems and branches of LSAs was significantly lower than that in healthy controls, while no difference was found in the curvature and tortuosity of LSA. In a genetic cSVD, called CADASIL (cerebral autosomal dominant arteriopathy with subcortical infarcts and leukoencephalopathy), the correlation between the number of LSA branches and the Mini-Mental State Examination (MMSE) score was confirmed. Meanwhile, an increased proportion of discontinuous flow of LSAs was reported in CADASIL patients [9]. LSAs are also a frequent source of lacunar infarcts. With segmentation and modeling, the culprit LSAs that may cause the lacunar infarct can be identified [10]. In addition, morphological changes in LSA were observed in the early progression of subcortical vascular dementia (SVaD). Lower number of branches and enlarged radius of LSA were found in SVaD patients [11]. These studies confirm that 7T TOF-MRA is an effective and non-invasive method to evaluate the morphological changes of perforating arteries in cSVD.

Flow velocity

By using velocity encoding (VENC) gradients, the flow velocity of blood vessels can be quantified by phase-contrast (PC) MRI. Time-resolved PC-MRI has been validated in measuring blood flow velocity of the aorta, carotid arteries and the circle of Willis (CoW) [12]. Due to the available SNR at 3T, the spatial resolution of PC-MRI cannot measure the flow velocity of arterioles very well. Another reason is that the partial volume effects lead to an underestimation of the flow velocity and miscalculate the flow direction [13]. The increased SNR and flow-related enhancement at 7T breaks down the barrier to measuring the velocity of perforating arteries. The velocity mapping of cerebral small vessels was firstly obtained with a non-time-resolved PC-MRA [14]. A VENC value of 15 cm/s was used to measure the velocity and direction of small arteries on the CoW, including LSA, posterior communicating artery and anterior choroidal artery. In patients with CADASIL, the flow velocity of LSA can be measured in the proximal segments [15]. The velocity was found to be decreasing with progression of the disease and correlated with aging, functional dependence, cognitive impairment and mood disturbance.

When scanned with a single slice technique, the time-resolved PC MRI enables dynamic assessment of flow pulsatility in perforating arteries. The temporal resolution can be set to 57-156 ms with an in-plane resolution of 0.3 mm [16]. In this manner, the flow velocities of LSAs can be measured at two planes: the basal ganglia (BG) and centrum semiovale (CSO). The range of changes in flow velocity within a cardiac cycle can be calculated as the pulsatility index (PI) [17], which represented the arteriole hemodynamics. In patients with cSVD-related stroke, the PIs of LSAs were found to be elevated in both BG and CSO [18]. Nevertheless, a higher PI was also correlated with age

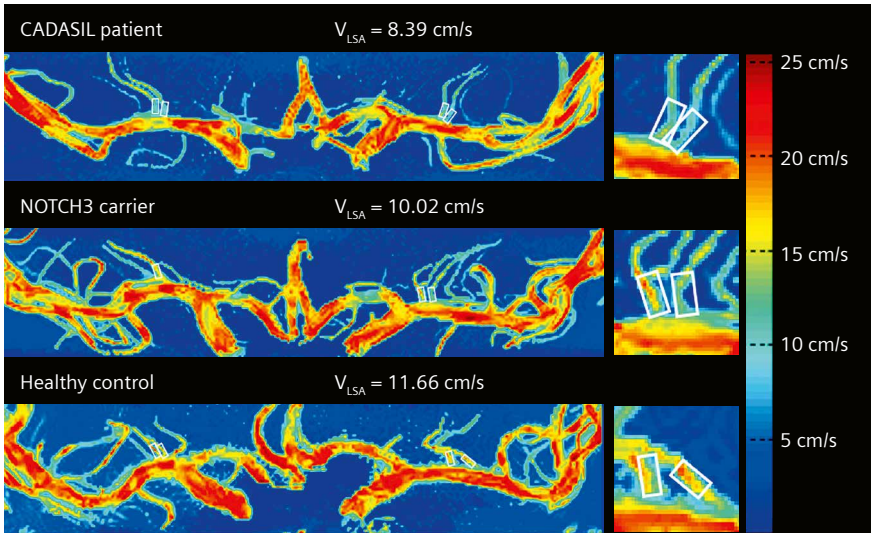

2 The flow velocities of proximal lenticulostriate arteries measured by 7T PC-MRA. The velocity decreased with the progression of cerebral small vessel disease. CADASIL is a form of hereditary stroke disorder and is thought to be caused by mutations in the NOTCH3 gene.

in healthy individuals. The boundary between pathological and physiological changes of PI in cerebral small vessels remains to be clarified in future studies.

Susceptibility imaging

Susceptibility refers to the extent to which a substance becomes magnetized when it is placed in an external magnetic field. Susceptibility weighted imaging (SWI) is a commonly used imaging method reflecting susceptibility contrast, while quantitative susceptibility mapping (QSM) serves as the quantification method. The susceptibility-induced field inhomogeneity is more prone to be detected at UHF, which makes it an ideal choice for SWI and QSM [19]. Deoxyhemoglobin, hemosiderin, and ferritin are rich in iron, which makes the signal of venous blood, cerebral microbleeds, and subcortical nuclei prominent on susceptibility imaging.

Cerebral veins with small calibers can be clearly displayed by 7T SWI, such as the deep medullary veins (DMVs). An automated algorithm to segment and quantify the DMV on 7T SWI was developed [20]. Using this method, the morphology of the DMV was analyzed in dementia likely caused by cSVD [21]. The number and vascular density were similar between patients and healthy controls, while more tortuous DMVs were found in the patient group. The curved DMVs were also more frequently to be found in sporadic cSVD [22]. The impaired integrity of the DMV was reported in CADASIL patients, which may occur before the appearance of white matter hyperintensities (WMH) [23]. The morphology of DMV on 7T SWI may play an important role in the diagnosis and research of cSVD.

The enhanced susceptibility effects at 7T makes QSM highly sensitive to magnetic susceptibility differences between components. Along with the increased SNR, the spatial resolution of QSM can be boosted at 7T. For instance, the higher susceptibility of superficial veins associated with disease progression was reported in CADASIL patients [24]. This increased susceptibility likely reflected decreased venous oxygen saturation. It was also related to the clinical phenotype and the STRIVE imaging features of cSVD.

Cerebral microbleeds (CMBs) are one of the conventional neuroimaging markers of cSVD. It can be detected with a higher sensitivity at 7T than at lower field strengths [25]. Considering the high detection rate of CMBs by 7T MRI, an automated postprocessing tool is needed for a reliable and reproducible detection. The increased CMBs and iron deposits caused by the dysfunction of blood-brain barrier in cSVD can be quantified using 7T QSM [26, 27].

Perivascular space

Perivascular spaces (PVS) are fluid-filled spaces that surround small arterioles, capillaries and venules in the brain. Enlarged PVS are considered one of the MR imaging hallmarks of cSVD and are associated with older age as well as the presence of lacunar infarcts and white matter lesions [28]. Using the increased CNR and spatial resolution, T2-weighted images at 7T were able to show not only the enlarged PVS, but also the physiological PVS in normal states [29]. The feasibility of imaging and quantifying PVS at 7T was first demonstrated in patients with Alzheimer's disease (AD). PVS was spatially correlated to LSA in BG

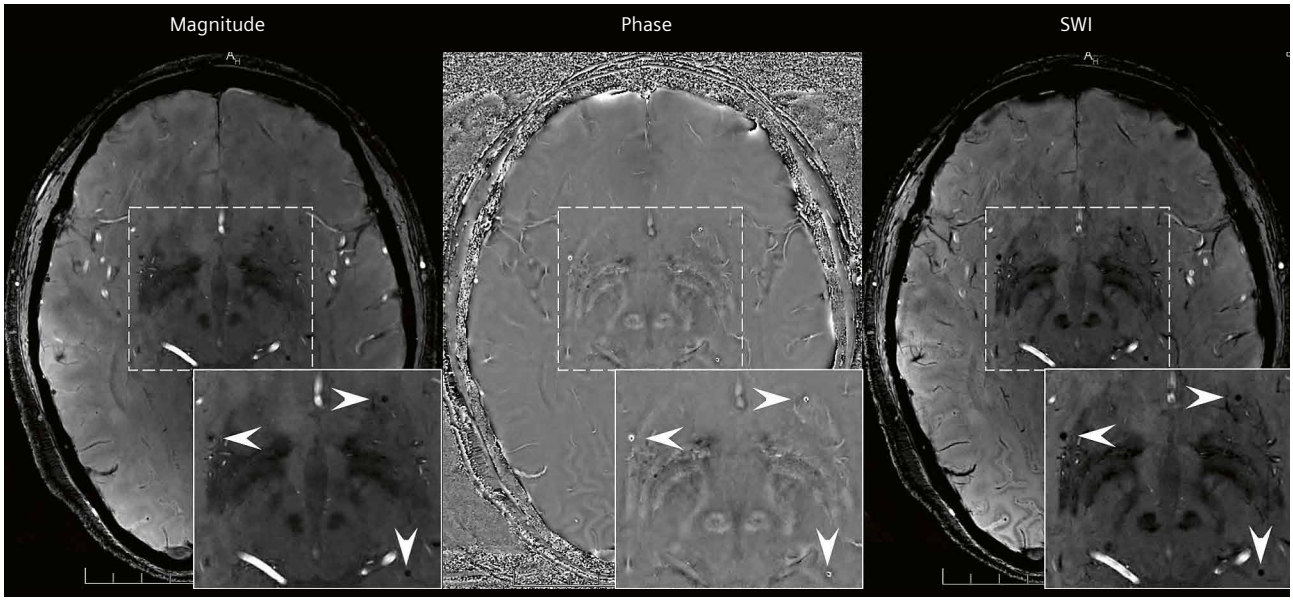

3 Cerebral microbleeds on susceptibility weighted imaging of a CADASIL patient. Arrowheads indicate the microbleeds in the thalamus.

and CSO, but not with veins [30]. Another study described the characteristics of PVS in BG, thalamus, midbrain, and white matter regions in 45 healthy subjects [31]. The number and volume fraction of PVS at BG were shown to increase with age, and largely varied among individuals. Interestingly, the study reported that inhalation of carbon dioxide significantly increased the volume fraction of PVS at BG and white matter, suggesting an association between vasodilation and PVS. The correlation between PVS and other imaging markers related to cSVD was then investigated in 50 community-dwelling individuals over 40 years old [32]. The number of PVS was found to corelate with the presence of CMBs, rather than age or vascular risk factors. Advanced post-processing methods were also developed to improve the visualization and quantification of PVS based on filtering and neural networks [33, 34]. In summary, PVS could be used as an imaging marker to reflect the progression of cSVD. However, the discrimination between physiological and pathological PVS must be answered by cohort studies in larger populations.

Cortical microinfarcts

Cerebral cortical microinfarcts (CMI) are a novel MRI marker of vascular brain injury and need a high spatial resolution to be detected. Using 7T MRI and histopathology on *ex vivo* tissue, cerebral microinfarcts greater than 1–2 mm in the cortical gray matter can be detected by 7T FLAIR with 0.80 mm isotropic resolution [35–37]. In another study, CMIs were also visible on 3T images, but the detection rate of these lesions was only 2% that of 7T [38]. Apart from the field strength, the sensitivity of CMI detection also depends on the imaging parameters and analysis methods: images should be acquired using 3D T1-weighted and 3D FLAIR (or T2-weighted) sequences with isotropic voxels less than 1 mm to avoid missing tiny lesions, preferably with additional T2*-weighted or hemorrhage-sensitive sequences such as SWI to rule out confounding imaging features such as CMBs. Most clinical *in vivo* studies have focused on the detection of intracortical microinfarcts, i.e., CMI, because it has been difficult to distinguish microinfarcts from other lesions in subcortical regions (e.g., WMH, lacunar infarcts, and enlarged PVS). For example, histopathologic examination of juxtacortical regions demonstrated that lesions suspected to be microinfarcts were usually enlarged PVS [36]. Therefore, the consensus was reached that punctate subcortical lesions cannot be classified as cerebral microinfarcts without confirmation by DWI [39].

The high detection rate of CMIs using high resolution structural imaging at 7T should have theoretically promoted the study of CMIs. However, controversy still exists on the prevalence of CMI due to the limited sample size of existing studies. For instance, a higher number of CMIs was found in 14 patients with AD compared with 18 healthy controls, while the incidence of CMI was similar between the two groups [40]. In another study, no difference in the incidence and number of CMI was found between 29 patients with early AD and 22 healthy controls [41]. Further multicenter clinical trials with large populations and definitive diagnosis of cSVD could provide more convincing results on the incidence, etiology, and role of CMIs in cSVD.

Future directions

Technical development

Both the hardware and software of 7T MRI were significantly improved over the recent years. The use of parallel transmitter coils (pTx)[1] has improved the field homogeneity significantly while still allowing simultaneous multiple slice

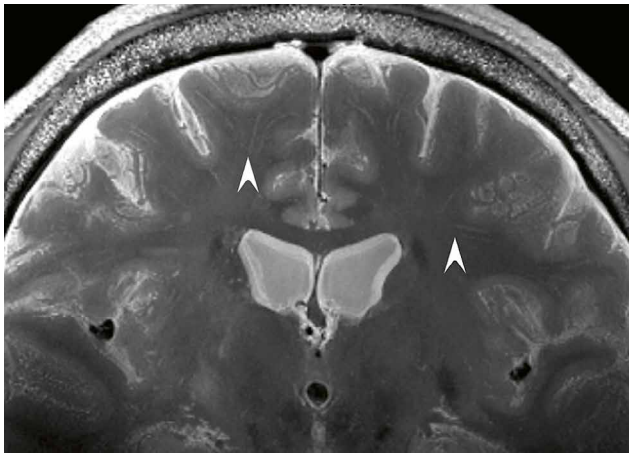

4 Perivascular spaces on a 7T T2-weighted image of a patient with subcortical vascular dementia.

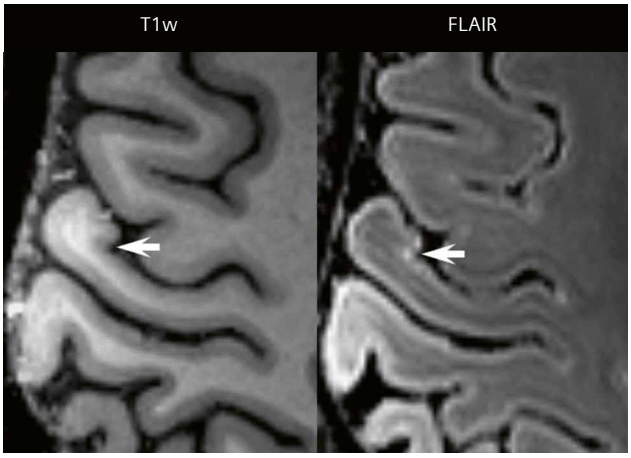

5 The cortical microinfarct on the T1-weighed and FLAIR images of a CADASIL patient.

(SMS) acquisition. The development of new receive coils[1] including combined head and neck coils will allow neurovascular imaging with head-and-neck coverage with higher SNR. The use of compressed sensing, machine learning[1] and Wave-CAIPI acceleration techniques will reduce the scan time or increase resolution further at 7T.

Broader clinical application

With more and more 7T human MRI scanners installed each year in both research centers and hospitals, and more 7T scanners released for clinical use, it is expected that an increasing number of clinical and research studies will be performed at 7T. So far, there were only a few small sampled studies directly comparing between 3T and 7T for different neurovascular diseases. In the near future, it is critical to perform larger scale comparison studies to demonstrate the unique advantage of 7T over 3T. To demonstrate the clinical value of 7T MRI, future large scale multi-center studies are required. Strong collaboration between 7T sites and standardization of techniques across sites and scanners using phantoms are needed to enable such multi center studies.

Conclusion

UHF MRI, especially 7T MRI, has demonstrated its great value in the diagnosis and research of cSVD. Benefiting from the higher SNR and contrast, multi-modality high-resolution imaging methods at 7T, especially those based on the angiography and susceptibility contrasts, reveal various structural and functional changes of cerebral small vessels in cSVD. In the future, large cohort studies are needed to verify the diagnostic power of these imaging features, and determine the thresholds differentiating the physiological and pathological states. Nevertheless, the relative scarcity of 7T MRI scanners, as well as the physical challenges of UHF imaging, still hinder the broad application of 7T MRI in clinical environments. The combination of technology development and clinical research will bring new advances of 7T MRI to neurologists.

[1] *Work in progress. The application is currently under development and is not for sale in the U.S. and in other countries. Its future availability cannot be ensured.*

References

1 Chojdak-Łukasiewicz J, Dziadkowiak E, Zimny A, Paradowski B. Cerebral small vessel disease: A review. Adv Clin Exp Med. 2021;30(3):349-356.

2 Gorelick PB, Scuteri A, Black SE, Decarli C, Greenberg SM, Iadecola C, et al. American Heart Association Stroke Council, Council on Epidemiology and Prevention, Council on Cardiovascular Nursing, Council on Cardiovascular Radiology and Intervention, and Council on Cardiovascular Surgery and Anesthesia. Vascular contributions to cognitive impairment and dementia: a statement for healthcare professionals from the american heart association/ american stroke association. Stroke. 2011;42(9):2672-2713.

3 Wardlaw JM, Smith EE, Biessels GJ, Cordonnier C, Fazekas F, Frayne R, et al. STandards for ReportIng Vascular changes on nEuroimaging (STRIVE v1). Neuroimaging standards for research into small vessel disease and its contribution to ageing and neurodegeneration. Lancet Neurol. 2013;12(8):822-838.

4 Pohmann R, Speck O, Scheffler K. Signal-to-noise ratio and MR tissue parameters in human brain imaging at 3, 7, and 9.4 tesla using current receive coil arrays. Magn Reson Med. 2016 Feb;75(2):801-809.

5 von Morze C, Xu D, Purcell DD, Hess CP, Mukherjee P, Saloner D, et al. Intracranial time-of-flight MR angiography at 7T with comparison to 3T. J Magn Reson Imaging. 2007;26(4):900-904.

6 Kang CK, Park CA, Park CW, Lee YB, Cho ZH, Kim YB. Lenticulostriate arteries in chronic stroke patients visualised by 7 T magnetic resonance angiography. Int J Stroke. 2010;5(5):374-380.

7 Lee YB, Kang CK, Kim KT, Park CA, Kim YB, Cho ZH. A non-invasive technique for visualization of microvessels in asymptomatic patients with middle cerebral artery steno-occlusion. Vasc Med. 2013;18(5):314-317.

8 Cho ZH, Lee YB, Kang CK, Yang JW, Jung IH, Park CA, et al. Microvascular imaging of asymptomatic MCA steno-occlusive patients using ultra-high-field 7T MRI. J Neurol. 2013;260(1):144-150.

9 Ling C, Fang X, Kong Q, Sun Y, Wang B, Zhuo Y, et al. Lenticulostriate Arteries and Basal Ganglia Changes in Cerebral Autosomal Dominant Arteriopathy With Subcortical Infarcts and Leukoencephalopathy, a High-Field MRI Study. Front Neurol. 2019;10:870.

10 Kang CK, Wörz S, Liao W, Park CA, Kim YB, Park CW, et al. Three dimensional model-based analysis of the lenticulostriate arteries and identification of the vessels correlated to the infarct area: preliminary results. Int J Stroke. 2012;7(7):558-563.

11 Seo SW, Kang CK, Kim SH, Yoon DS, Liao W, Wörz S, et al. Measurements of lenticulostriate arteries using 7T MRI: new imaging markers for subcortical vascular dementia. J Neurol Sci. 2012;322(1-2):200-205.

12 Schneiders JJ, Ferns SP, van Ooij P, Siebes M, Nederveen AJ, van den Berg R, et al. Comparison of phase-contrast MR imaging and endovascular sonography for intracranial blood flow velocity measurements. AJNR Am J Neuroradiol. 2012;33(9):1786-1790.

13 Hofman MB, Visser FC, van Rossum AC, Vink QM, Sprenger M, Westerhof N. In vivo validation of magnetic resonance blood volume flow measurements with limited spatial resolution in small vessels. Magn Reson Med. 1995;33(6):778-784.

14 Kang CK, Park CA, Lee DS, Lee YB, Park CW, Kim YB, et al. Velocity measurement of microvessels using phase-contrast magnetic resonance angiography at 7 Tesla MRI. Magn Reson Med. 2016;75(4):1640-1646.

15 Sun C, Wu Y, Ling C, Xie Z, Sun Y, Xie Z, et al. Reduced blood flow velocity in lenticulostriate arteries of patients with CADASIL assessed by PC-MRA at 7T. J Neurol Neurosurg Psychiatry. 2022;93(4):451-452.

16 Bouvy WH, Geurts LJ, Kuijf HJ, Luijten PR, Kappelle LJ, Biessels GJ, et al. Assessment of blood flow velocity and pulsatility in cerebral perforating arteries with 7-T quantitative flow MRI. NMR Biomed. 2016;29(9):1295-1304.
17 Geurts L, Biessels GJ, Luijten P, Zwanenburg J. Better and faster velocity pulsatility assessment in cerebral white matter perforating arteries with 7T quantitative flow MRI through improved slice profile, acquisition scheme, and postprocessing. Magn Reson Med. 2018;79(3):1473-1482.
18 Geurts LJ, Zwanenburg JJM, Klijn CJM, Luijten PR, Biessels GJ. Higher Pulsatility in Cerebral Perforating Arteries in Patients With Small Vessel Disease Related Stroke, a 7T MRI Study. Stroke. 2018 Dec 11;50(1):62–68.
19 Ugurbil K. Magnetic resonance imaging at ultrahigh fields. IEEE Trans Biomed Eng. 2014;61(5):1364-1379.
20 Kuijf HJ, Bouvy WH, Zwanenburg JJ, Razoux Schultz TB, Viergever MA, et al. Quantification of deep medullary veins at 7 T brain MRI. Eur Radiol. 2016;26(10):3412-3418.
21 Bouvy WH, Kuijf HJ, Zwanenburg JJ, Koek HL, Kappelle LJ, Luijten PR, et al.; Utrecht Vascular Cognitive Impairment (VCI) Study group. Abnormalities of Cerebral Deep Medullary Veins on 7 Tesla MRI in Amnestic Mild Cognitive Impairment and Early Alzheimer's Disease: A Pilot Study. J Alzheimers Dis. 2017;57(3):705-710.
22 Shaaban CE, Aizenstein HJ, Jorgensen DR, MacCloud RL, Meckes NA, Erickson KI, et al.; LIFE Study Group. In Vivo Imaging of Venous Side Cerebral Small-Vessel Disease in Older Adults: An MRI Method at 7T. AJNR Am J Neuroradiol. 2017;38(10):1923-1928.
23 De Guio F, Vignaud A, Ropele S, Duering M, Duchesnay E, Chabriat H, et al. Loss of venous integrity in cerebral small vessel disease: a 7-T MRI study in cerebral autosomal-dominant arteriopathy with subcortical infarcts and leukoencephalopathy (CADASIL). Stroke. 2014;45(7):2124-2126.
24 Ling C, Zhang Z, Wu Y, Fang X, Kong Q, Zhang W, et al. Reduced Venous Oxygen Saturation Associates With Increased Dependence of Patients With Cerebral Autosomal Dominant Arteriopathy With Subcortical Infarcts and Leukoencephalopathy: A 7.0-T Magnetic Resonance Imaging Study. Stroke. 2019;50(11):3128-3134.
25 Bian W, Hess CP, Chang SM, Nelson SJ, Lupo JM. Susceptibility-weighted MR imaging of radiation therapy-induced cerebral microbleeds in patients with glioma: a comparison between 3T and 7T. Neuroradiology. 2014;56(2):91-96.
26 Sun C, Wu Y, Ling C, Xie Z, Kong Q, Fang X, et al. Deep Gray Matter Iron Deposition and Its Relationship to Clinical Features in Cerebral Autosomal Dominant Arteriopathy With Subcortical Infarcts and Leukoencephalopathy Patients: A 7.0-T Magnetic Resonance Imaging Study. Stroke. 2020;51(6):1750-1757.
27 Liem MK, Lesnik Oberstein SA, Versluis MJ, Maat-Schieman ML, Haan J, et al. 7 T MRI reveals diffuse iron deposition in putamen and caudate nucleus in CADASIL. J Neurol Neurosurg Psychiatry. 2012;83(12):1180-1185.
28 Potter GM, Doubal FN, Jackson CA, Chappell FM, Sudlow CL, Dennis MS, et al. Enlarged perivascular spaces and cerebral small vessel disease. Int J Stroke. 2015;10(3):376-381.
29 Barisano G, Law M, Custer RM, Toga AW, Sepehrband F. Perivascular Space Imaging at Ultrahigh Field MR Imaging. Magn Reson Imaging Clin N Am. 2021;29(1):67-75.
30 Bouvy WH, Biessels GJ, Kuijf HJ, Kappelle LJ, Luijten PR, Zwanenburg JJ. Visualization of perivascular spaces and perforating arteries with 7 T magnetic resonance imaging. Invest Radiol. 2014;49(5):307-313.
31 Zong X, Lian C, Jimenez J, Yamashita K, Shen D, Lin W. Morphology of perivascular spaces and enclosed blood vessels in young to middle-aged healthy adults at 7T: Dependences on age, brain region, and breathing gas. Neuroimage. 2020;218:116978.
32 Bouvy WH, Zwanenburg JJM, Reinink R, Wisse LEM, Luijten PR, Kappelle LJ, et al.; Utrecht Vascular Cognitive Impairment (VCI) Study group. Perivascular spaces on 7 Tesla brain MRI are related to markers of small vessel disease but not to age or cardiovascular risk factors. J Cereb Blood Flow Metab. 2016;36(10):1708-1717.
33 Hou Y, Park SH, Wang Q, Zhang J, Zong X, Lin W, et al. Enhancement of Perivascular Spaces in 7 T MR Image using Haar Transform of Non-local Cubes and Block-matching Filtering. Sci Rep. 2017;7(1):8569.
34 Jung E, Chikontwe P, Zong X, Lin W, Shen D, Park SH. Enhancement of Perivascular Spaces Using Densely Connected Deep Convolutional Neural Network. IEEE Access. 2019;7:18382-18391.
35 van Veluw SJ, Zwanenburg JJ, Engelen-Lee J, Spliet WG, Hendrikse J, Luijten PR, et al. In vivo detection of cerebral cortical microinfarcts with high-resolution 7T MRI. J Cereb Blood Flow Metab. 2013;33(3):322-329.
36 van Veluw SJ, Zwanenburg JJ, Rozemuller AJ, Luijten PR, Spliet WG, Biessels GJ. The spectrum of MR detectable cortical microinfarcts: a classification study with 7-tesla postmortem MRI and histopathology. J Cereb Blood Flow Metab. 2015;35(4):676-683.
37 van Veluw SJ, Charidimou A, van der Kouwe AJ, Lauer A, Reijmer YD, Costantino I, et al. Microbleed and microinfarct detection in amyloid angiopathy: a high-resolution MRI-histopathology study. Brain. 2016;139(Pt 12):3151-3162.
38 van Veluw SJ, Hilal S, Kuijf HJ, Ikram MK, Xin X, Yeow TB, et al. Cortical microinfarcts on 3T MRI: Clinical correlates in memory-clinic patients. Alzheimers Dement. 2015;11(12):1500-1509.
39 van Veluw SJ, Shih AY, Smith EE, Chen C, Schneider JA, Wardlaw JM, et al. Detection, risk factors, and functional consequences of cerebral microinfarcts. Lancet Neurol. 2017;16(9):730-740.
40 van Rooden S, Goos JD, van Opstal AM, Versluis MJ, Webb AG, Blauw GJ, et al. Increased number of microinfarcts in Alzheimer disease at 7-T MR imaging. Radiology. 2014;270(1):205-211.
41 van Veluw SJ, Heringa SM, Kuijf HJ, Koek HL, Luijten PR, Biessels GJ; Utrecht Vascular Cognitive Impairment study group. Cerebral cortical microinfarcts at 7Tesla MRI in patients with early Alzheimer's disease. J Alzheimers Dis. 2014;39(1):163-167.

Contact

Assistant Professor Zihao Zhang
State Key Laboratory of Brain and Cognitive Science
Institute of Biophysics
Chinese Academy of Sciences
15 Datun Road
Beijing 100101
China
zhzhang@ibp.ac.cn

Depicting the Labyrinthine Artery at 7T: An Ultra-High-Resolution 3D Time-of-Flight Study

Hui Liu, Yuancheng Jiang, Jianxun Qu

Siemens Healthineers, China

The labyrinthine artery is a small end artery that typically arises from the anterior inferior cerebellar artery (AICA) and supplies the cochlear and vestibular structures of the inner ear [1]. Imaging it directly matters clinically: Because the artery has essentially no collateral circulation, any interruption of its flow may injure the auditory and vestibular system, leading to hearing loss and vertigo [2]. Capturing it on imaging is no easy task. The labyrinthine artery runs a short course deep within the internal auditory canal, and at roughly 180 µm in diameter — barely thicker

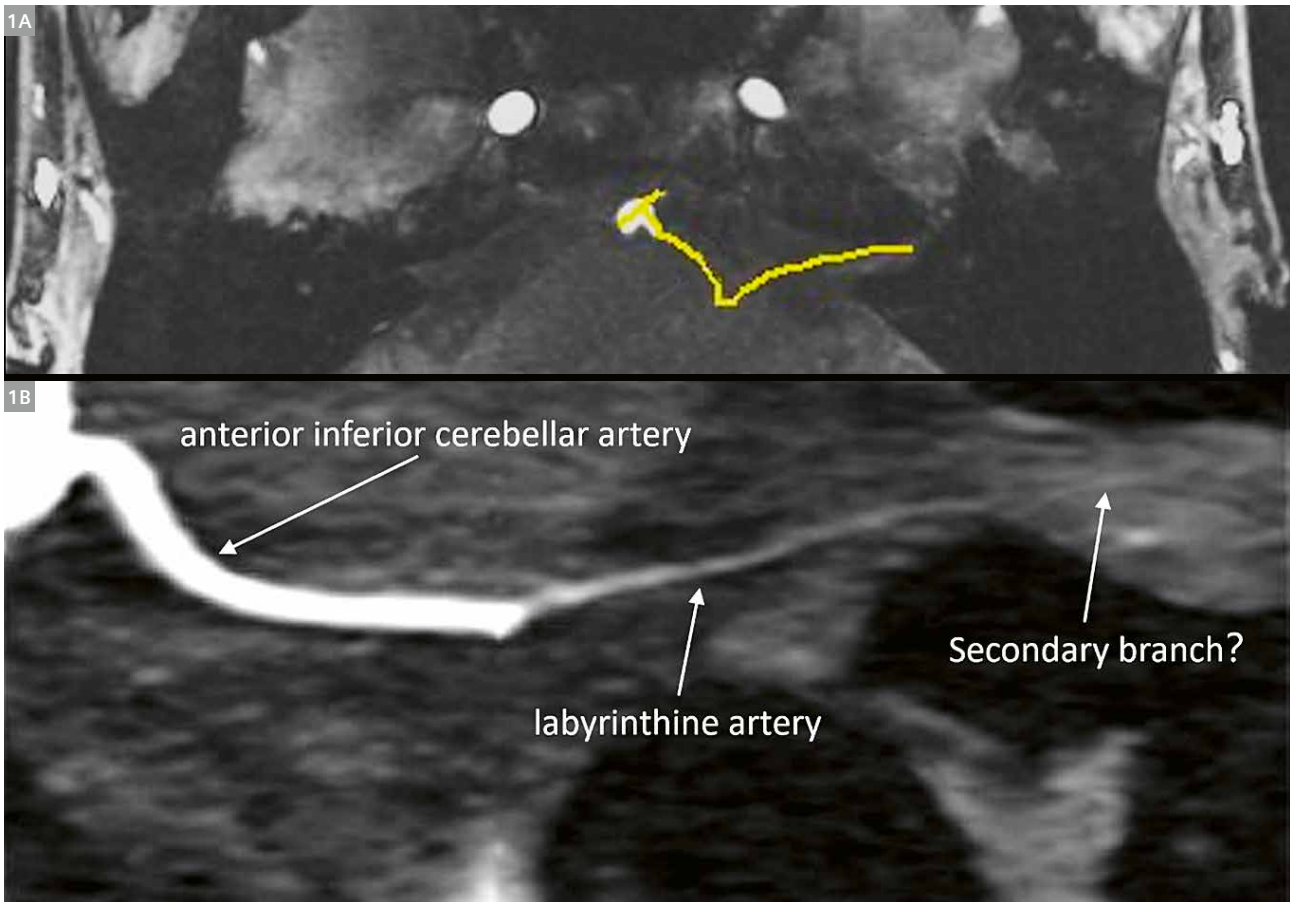

1 Ultra-high-resolution 7T TOF-MRA of the labyrinthine artery. **(1A)** The yellow line indicates the curved reconstruction plane selected to follow the course of the target vessel. **(1B)** The curved planar reconstructed image shows the labyrinthine artery continuous with the anterior inferior cerebellar artery (AICA) and coursing toward the internal auditory canal. A small distal branch-like signal is also visible, possibly representing a secondary branch.

than a human hair (~120 µm) — it demands both extremely high-resolution and strong artery-to-background contrast [3]. This makes ultra-high-field (UHF) 7T an attractive platform [4]. Previous work has demonstrated that the labyrinthine artery can be visualized with 7T time-of-flight magnetic resonance angiography (TOF-MRA) [5], but there remains room for improved clarity. In this case, we set out to show that targeted, ultra-high-resolution 7T TOF-MRA can depict the labyrinthine artery and trace its course precisely and clearly.

The case was conducted on a 7T MAGNETOM Terra system (Siemens Healthineers, Erlangen, Germany) equipped with an 8Tx/32Rx head coil (Nova Medical, Wilmington, MA, USA). We acquired a targeted high-resolution TOF-MRA of the labyrinthine artery with the following parameters: TR/TE = 27/2.38 ms, flip angle = 32°, in-plane resolution = 0.25 × 0.25 mm², slice thickness = 0.15 mm, slab thickness = 16.8 mm, and total acquisition time = 7:15. Curved planar reconstruction was then performed to unfold the vessel along its course. The reconstruction plane is illustrated in Figure 1A, and the reconstructed image is illustrated in Figure 1B. Two physicians independently reviewed the images and identified the depicted vessel as the labyrinthine artery. The artery was clearly visualized and appeared continuous along its expected route — from the basilar arterial system, through the AICA, and toward the internal auditory canal. A small branch-like signal was also visible distally, suggestive of a secondary branch.

Being able to see the labyrinthine artery directly could give clinicians a new window into the vascular perspective when assessing inner-ear disorders. A recent case report, for example, suggested that visualization of changes in the labyrinthine artery may help identify acute labyrinthine ischemia [6]. In this study, the spatial resolution and vessel-to-background contrast of 7T were enough to depict the small artery clearly and to follow its course continuously back to the AICA. This ability to trace the arterial course opens the door to future studies examining the vascular factors in patients with hearing loss or vertigo. The next step is to test this approach in relevant patient populations to establish its clinical value.

References

1 Tempski J, Fibiger G, Majka K, Pękala J, Andrasz O, Wilczek J, et al. Surgical anatomy of the labyrinthine artery — a systematic review and meta-analysis. Neurosurg Rev [Internet]. 2025;48(1):464. Available from: http://dx.doi.org/10.1007/s10143-025-03592-0

2 Kim JS, Lopez I, DiPatre PL, Liu F, Ishiyama A, Baloh RW. Internal auditory artery infarction: clinicopathologic correlation. Neurology [Internet]. 1999;52(1):40–4. Available from: http://dx.doi.org/10.1212/wnl.52.1.40

3 Batts S, Pham N, Tearney G, Stankovic KM. The state of high-resolution imaging of the human inner ear: A look into the black box. Adv Sci (Weinh) [Internet]. 2025;12(28):e00556. Available from: http://dx.doi.org/10.1002/advs.202500556

4 Cosottini M, Calzoni T, Lazzarotti GA, Grigolini A, Bosco P, Cecchi P, et al. Time-of-flight MRA of intracranial vessels at 7 T. Eur Radiol Exp [Internet]. 2024;8(1):68. Available from: http://dx.doi.org/10.1186/s41747-024-00463-z

5 Sato H, Kawagishi K. Labyrinthine artery detection in patients with idiopathic sudden sensorineural hearing loss by 7-T MRI. Otolaryngol Head Neck Surg [Internet]. 2014;150(3):455–9. Available from: http://dx.doi.org/10.1177/0194599813517990

6 Sun X, Chen J, Xu J. Photon-counting CT demonstration of acute labyrinthine ischemia in idiopathic sudden sensorineural hearing loss: a case report. Front Med (Lausanne) [Internet]. 2025;12(1709516):1709516. Available from: http://dx.doi.org/10.3389/fmed.2025.1709516

Contact

Hui Liu, Ph.D.
Siemens Healthineers
SHS CHN CS-CRM APP MR NS
76, Kangning Street
Zhengzhou, HA
Zhengzhou 450000
China

Yuancheng Jiang
Siemens Healthineers
SHS CHN DI MR RCT UHF
No. 7 Wangjing Zhonghuan Nanlu,
Chaoyang District
Beijing 100102
China

Jianxun Qu
Siemens Healthineers
SHS CHN DI MR RCT UHF
No. 7 Wangjing Zhonghuan Nanlu,
Chaoyang District
Beijing 100102
China

MRA at 7T: Unlocking the Potential of Small Vessel Imaging

Qi Duan[1], Jinhao Lyu[1], Jianxun Qu[2], Xin Lou[1]

[1] Department of Radiology, The First Medical Center, Chinese PLA General Hospital (PLAGH), Beijing, China
[2] Siemens Healthineers, MR Research and Collaboration Team, Beijing, China

Introduction: The resolution revolution

Magnetic resonance angiography (MRA) is a mainstay of vascular imaging. Among its techniques, time-of-flight MRA (TOF-MRA) offers particular advantages: It needs no contrast agents, has no ionizing radiation, and uses the natural inflow of blood to map vessel architecture [1, 2]. It is a workhorse for screening, diagnosing, and monitoring cerebrovascular disease in MRI.

At 1.5T and 3T, the voxel size is typically capped at the hundred-nanoliter range (cubes of 0.5–0.8 mm) [3]. This leaves critical small vessels — perforating arteries, collateral networks, and distal branches — blurred or beyond reach. Their signal is diluted across volumes far larger than the structures themselves, and lesions or occlusions that could flag early stroke often risk going unseen.

The arrival of 7T MRI has changed the equation. The jump in signal-to-noise ratio (SNR) and the prolonged T1 relaxation time at 7T enable TOF-MRA to push the voxel size deeper into the 10-nanoliter range (down to 0.3 mm isotropic or even further). The vessel that once had to share its voxel with neighbors now gets one of its own [4].

At the PLA General Hospital (PLAGH), one of China's first centers to bring 7T MRI into clinical use, we have been continuously exploring and maximizing its clinical value since its deployment in 2021. Over the past several years, we have applied TOF-MRA across a spectrum of cerebrovascular conditions, including intracranial atherosclerotic stenosis, small vessel disease, and moyamoya disease, focusing on the brain's most vulnerable small vessels. Here, we present some of our findings.

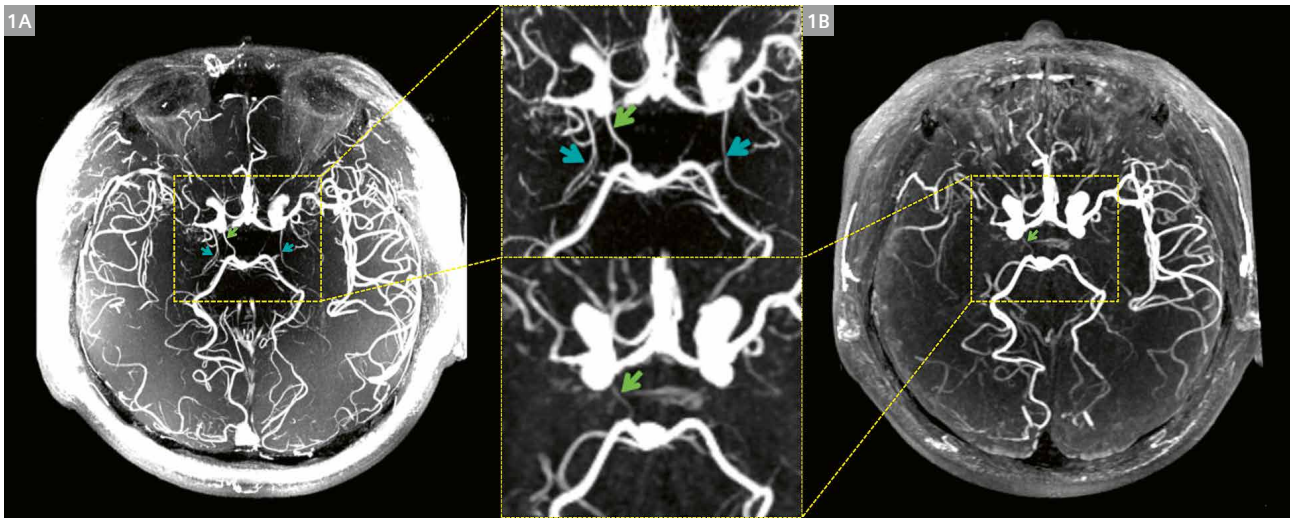

1 Comparison between 7T TOF-MRA **(1A)** and 3T TOF-MRA **(1B)** in the visualization of the anterior choroidal artery and posterior communicating artery. The 7T TOF-MRA demonstrated superior performance to 3T and provided comparable visualization of both the anterior choroidal artery (blue arrows) and posterior communicating artery (green arrows). TOF-MRA = time-of-flight magnetic resonance angiography.

Imaging small vessels in moyamoya disease

Moyamoya disease (MMD) is a chronic, progressive cerebrovascular disorder characterized by steno-occlusion at the terminal internal carotid artery and by the sprouting of abnormal collateral networks. It is a leading cause of stroke in children and young adults. Digital subtraction angiography (DSA) is the gold standard, but its invasiveness and radiation burden make it impractical for repeated monitoring — especially for younger patients.

Two small vessels hold particular prognostic value in MMD: the anterior choroidal artery (AChA) and the posterior communicating artery (PComA) [5]. Dilation and branching of these arteries are strongly associated with hemorrhagic risk. Visualizing them with precision is essential for early risk stratification.

At the PLA General Hospital, we compared 7T TOF-MRA against 3T TOF-MRA in a head-to-head study of 180 patients. The finer spatial precision of 7T allowed more accurate identification of these hemorrhage-risk features. Notably, 42% of the AChA anomalies and 28% of the PComA anomalies detected on 7T were invisible on 3T. In a DSA-validated subset of 37 patients, 7T further demonstrated high concordance with the gold standard [6].

The practical meaning is clear: A completely non-invasive, radiation-free scan can now deliver reliable hemorrhage risk assessment for MMD patients, offering a safer pathway for long-term follow-up.

Imaging small vessels in middle cerebral artery stenosis

The lenticulostriate arteries (LSAs) are slender perforating arteries arising from the middle cerebral artery (MCA) and supplying the basal ganglia. This region lacks robust collateral circulation; when LSAs fail, basal ganglia infarction follows, often with severe neurological consequences. With diameters ranging from 0.08 to 1.5 mm, LSAs have long been among the most elusive targets in neuroimaging, reliably visible only through invasive DSA or in post-mortem anatomy. Even at 3T, their distal branches remain beyond reach.

In a large-sample quantitative study of 161 patients, we found that proximal location, rather than the stenosis

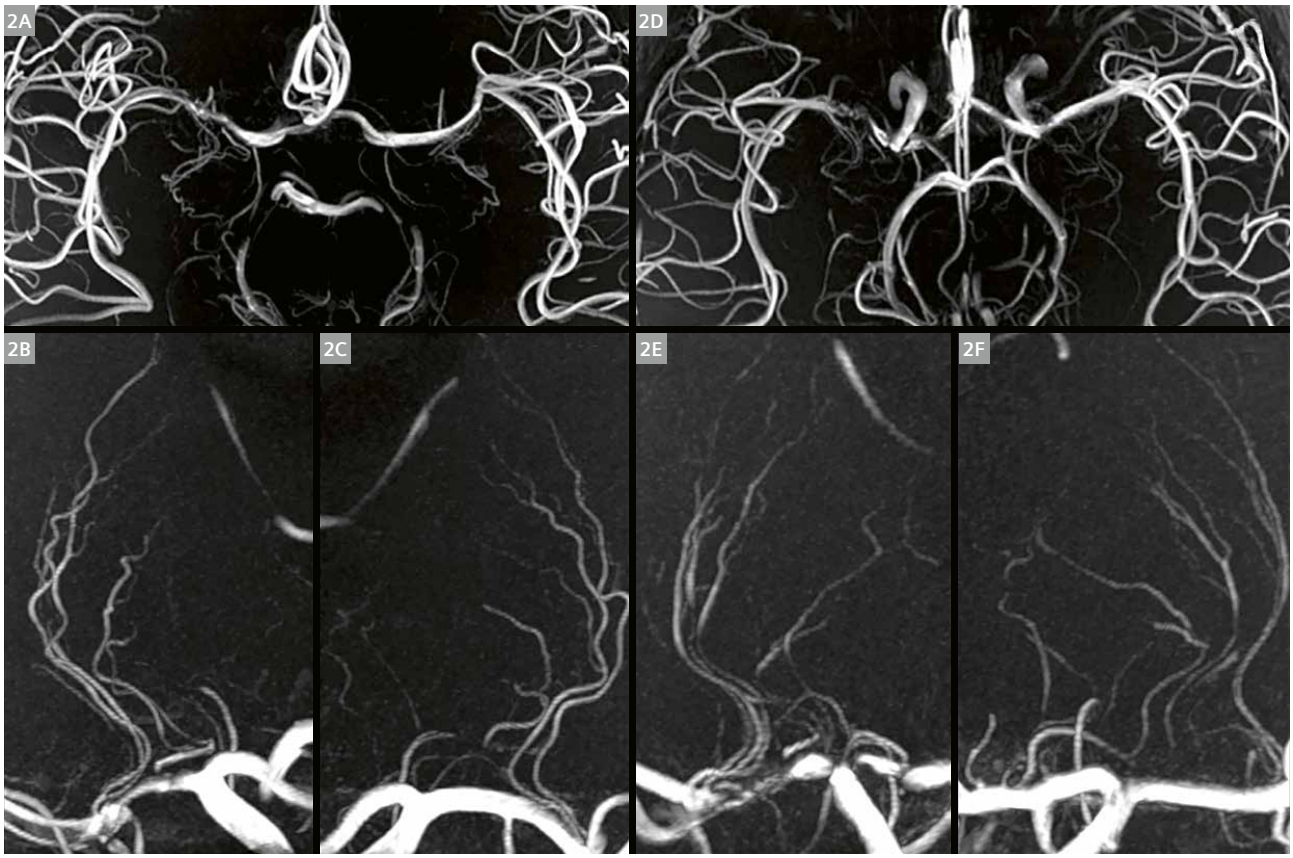

2 Representative images of a 46-year-old man with asymptomatic mild-to-moderate stenosis in the M1 segment of the right MCA **(2A–2C)** and a 30-year-old woman with asymptomatic severe right MCA M1-segment stenosis **(2D–2F)**. Compared to those on the contralateral side, the number of LSA branches on the stenosis side and their length do not decrease **(2B vs. 2C; 2E vs. 2F)**. MCA = middle cerebral artery; LSA = lenticulostriate artery.

severity, of the MCA M1-segment stenosis was the predominant determinant of LSA morphology — a finding established in asymptomatic subgroups and confirmed by multivariable regression [7]. Symptomatic patients showed significantly fewer LSA branches and shorter lengths on the affected side, while asymptomatic patients with proximal MCA M1-segment stenosis similarly exhibited diminished branching compared to those with distal stenosis.

This shifts the clinical approach to risk assessment for basal ganglia stroke. It means that a noninvasive scan, done at sufficient resolution, can now read the anatomical signature that predicts vulnerability — something previously only possible through catheter angiography or autopsy.

Conclusion

The transition from 3T to 7T is not just an improvement in image quality, but a shift in what clinicians can see and therefore in what they can act upon. At the PLA General Hospital, our work with TOF-MRA at 7T has demonstrated that hemorrhage risk stratification in moyamoya disease and morphological assessment of lenticulostriate arteries in MCA stenosis can now be performed noninvasively, reliably, and with high fidelity to the gold standard of DSA. For physicians, this means earlier and more precise risk stratification without exposing patients to radiation or invasive procedures. For patients, particularly children and young adults who face repeated follow-up, it means a safer diagnostic journey.

References

1 Wheaton AJ, Miyazaki M. Non-contrast enhanced MR angiography: physical principles. J Magn Reson Imaging [Internet]. 2012;36(2): 286–304. Available from: http://dx.doi.org/10.1002/jmri.23641

2 Matsushige T, Kraemer M, Schlamann M, Berlit P, Forsting M, Ladd ME, et al. Ventricular microaneurysms in Moyamoya angiopathy visualized with 7T MR angiography. AJNR Am J Neuroradiol [Internet]. 2016;37(9):1669–72. Available from: http://dx.doi.org/10.3174/ajnr.A4786

3 Radojewski P, Piredda GF, Bonanno G, Lövblad K-O, Vargas MI, Sutter R, et al. Assessment of the available evidence for the use of 7-Tesla (T) magnetic resonance imaging (MRI) in neurological and musculoskeletal disorders, with comparison to 3-T and 1.5-T MRI: A systematic scoping review. Eur J Neurol [Internet]. 2025;32(1): e16557. Available from: http://dx.doi.org/10.1111/ene.16557

4 Trattnig S, Springer E, Bogner W, Hangel G, Strasser B, Dymerska B, et al. Key clinical benefits of neuroimaging at 7T. Neuroimage [Internet]. 2018;168:477–89. Available from: http://dx.doi.org/10.1016/j.neuroimage.2016.11.031

5 Morioka M, Hamada J-I, Kawano T, Todaka T, Yano S, Kai Y, Ushio Y. Angiographic dilatation and branch extension of the anterior choroidal and posterior communicating arteries are predictors of hemorrhage in adult moyamoya patients. Stroke [Internet]. 2003;34(1):90–5. Available from: http://dx.doi.org/10.1161/01.str.0000047120.67507.0d

6 Duan Q, Lyu J, Liu Z, Hao F, Li R, Liu S, et al. Noninvasive assessment of the risk features of hemorrhage in moyamoya disease using 7T MRI. Neurology [Internet]. 2025;104(11):e213617. Available from: http://dx.doi.org/10.1212/WNL.0000000000213617

7 Li R, Lyu J, Hu R, Duan Q, Wang W, Bian X, et al. Morphological study on lenticulostriate arteries in patients with middle cerebral artery stenosis at 7 T MRI. J Magn Reson Imaging [Internet]. 2025;62(1):201–12. Available from: http://dx.doi.org/10.1002/jmri.29693

Contact

Xin Lou, M.D.
Chief Physician and Chairman of the Department of Radiology
The First Medical Center of Chinese PLA General Hospital
No. 28 Fuxing Road
Beijing, China, 100853
louxin@301hospital.com.cn

Qi Duan, M.D.
Medical Doctoral Student in the Department of Radiology
The First Medical Center of Chinese PLA General Hospital

Jianxun Qu, M.Eng.
Collaboration Scientist
Siemens Healthineers
Beijing
China
jianxun.qu@siemens-healthineers.com

Jinhao Lyv, M.D.
Attending Physician in the Department of Radiology
The First Medical Center of Chinese PLA General Hospital

Imaging Aortic Dissections and Aneurysms with MRI: The Clinical Value of Advanced Angiography and 4D Flow Sequences

Alain Lalande[1], Marylène Delcey[2], Daniel Giese[3], Ning Jin[4], You Zhou[5], Olivier Bouchot[6]

[1] Université Bourgogne Europe, CHU Dijon Bourgogne, Pôle Imagerie, CNRS, ICMUB UMR 6302, Dijon, France
[2] Siemens Healthineers SAS, Courbevoie, France
[3] Siemens Healthineers AG, Erlangen, Germany
[4] Siemens Medical Solutions USA Inc., Malvern, PA, USA
[5] Université Bourgogne Europe, CNRS, ICMUB UMR 6302, Dijon, France
[6] Université Bourgogne Europe, CHU Dijon Bourgogne, Service de Chirurgie Cardiovasculaire et Thoracique, CNRS, ICMUB UMR 6302, Dijon, France

Introduction

Ascending aortic aneurysms are characterized by dilation of the ascending aorta that progressively develops over several years and may ultimately result in aortic dissection or aortic rupture. The only curative treatment is surgical, involving replacement of the aneurysmal segment with a Dacron prosthetic graft. Currently, surgical recommendations are based on the maximum diameter of the ascending aorta (between 45 and 55 mm depending on the presence of potential associated risk factors for rupture, such as connective tissue disease, bicuspid aortic valve, or rapid aneurysm progression) [1]. However, this criterion is imperfect, and for personalized management of this disease, the generation of new biomarkers (including aorta shape, movement, and constrain flow) that allow personalized treatment of thoracic aortic aneurysms (TAA) is essential. These new biomarkers can be obtained from ex vivo biomechanical tests [2], angiography from MRI, or 4D flow MRI. In this context, MRI of the aorta done at 3T is a cornerstone for assessing these parameters. This is the objective of the MECATHOR project [3] (registered on clinicaltrials.gov under NCT03746964), which is studying 200 patients presenting with an ascending aorta aneurysm.

In addition, aortic dissection is a serious condition in which a tear occurs within the inner layers of the aorta. This allows blood to enter the aortic wall and leads to the formation of a true lumen and a false lumen, with the main risk being aortic wall rupture. According to the Stanford classification, there are two types of aortic dissections depending on the region of the aorta where the tear occurs [1, 4]. In this classification, Type A corresponds to a dissection involving the ascending aorta (immediately after the heart), whereas Type B refers to a dissection affecting the descending aorta. Type A dissections are a surgical emergency. Type B dissections are a medical emergency requiring regular follow-up and are considered to be a chronic aortic dissection. Type A could be present as a residual Type B aortic dissection to the descending aorta. It is now recognized that anatomy, and particularly diameter alone, does not allow prediction of the progression of chronic aortic dissection toward an aneurysm that requires surgical management [5]. The objective of the ADEPT project (registered on clinicaltrials.gov under NCT07315178) is to develop a patient-specific digital twin that enables multifactorial modeling of high-risk regions and prediction of the aneurysmal evolution of chronic aortic dissection. This digital twin will be based on 3D modeling of the aorta from MRI data and will integrate all parameters obtained from biomechanics, histology, imaging, and blood biomarkers.

In these two projects (MECATHOR and ADEPT), the MRI protocol incorporates two key sequences: angiography of the aorta and 4D flow MRI. Angiography is used to obtain basic anatomical information and a precise shape of the aorta, with excellent contrast between the vessel lumen and wall. Flow imaging is used to characterize blood flow and its interaction with the aortic wall (such as wall shear stress (WSS)). However, both techniques are inherently time-consuming and remain sensitive to motion artifacts, particularly due to respiratory variability and prolonged acquisition times, which may lead to heterogeneous image quality in clinical practice. These limitations represent a major barrier, especially in patients requiring repeated longitudinal follow-up. In this context, the compressed sensing (CS) technique is applied to both MR angiography (MRA) and 4D flow imaging to offer a promising solution [6]. By enabling highly accelerated acquisitions, CS has the potential to reduce scan duration, improve robustness

to motion, and increase overall workflow efficiency. Furthermore, CS-based approaches make it feasible to implement the multi-velocity encoding (VENC) acquisition in a clinically acceptable duration. This allows accurate depiction of a broader range of flow velocities, from high-velocity jets to slow recirculating flow, which is particularly relevant in complex aortic pathologies, such as the flow in false lumen in cases of dissection. This paper therefore evaluates the clinical relevance and added value of these advanced CS-accelerated MRA and 4D flow MRI techniques in the initial assessment and longitudinal follow-up of patients with severe aortic diseases and therefore complex anatomy.

Methods and protocols

MRI acquisitions and study population

All examinations were performed on a clinical 3T scanner (MAGNETOM Vida Fit, Siemens Healthineers, Erlangen, Germany) equipped with multi-channel cardiac and thoracic coils (18-channel body coil), allowing extended coverage of the thoracic and abdominal aorta. Acquisitions of the sequences with CS were conducted during free breathing with electrocardiographic (ECG) gating and respiratory motion synchronization.

The overall imaging protocol was designed to enable a comprehensive assessment of both vascular morphology and aortic hemodynamics within a single examination, relying on two research sequences: an advanced MRA sequence (non-CE MRA and CE-MRA)* and an advanced 4D flow MRI acquisition*. Complementary sequences such as 3D T1 SPACE (also called blackblood in cases of dissection) and 2D phase-contrast sequence were included in the protocol. The detailed protocol is illustrated in Figure 1.

To date, over 80 exams for patients with aortic aneurysm (from the total of 200 exams involved in the MERCATHOR project) and 15 exams for patients with aortic dissection (the ADEPT project has just started) have been performed with these sequences.

MR angiography (Advanced MRA*)

Morphological assessment of the aorta was based on a three-dimensional native MRA sequence (non-CE MRA), relying on a T2-prepared gradient-echo acquisition with fat suppression.

To reduce acquisition time and motion-related artifacts, a CS acceleration strategy was implemented. This approach relies on the undersampling of *k*-space combined with iterative reconstruction, enabling high spatial resolution with significantly reduced scan times.

** Work in progress. The application is still under development and not commercially available. Its future availability cannot be ensured.*

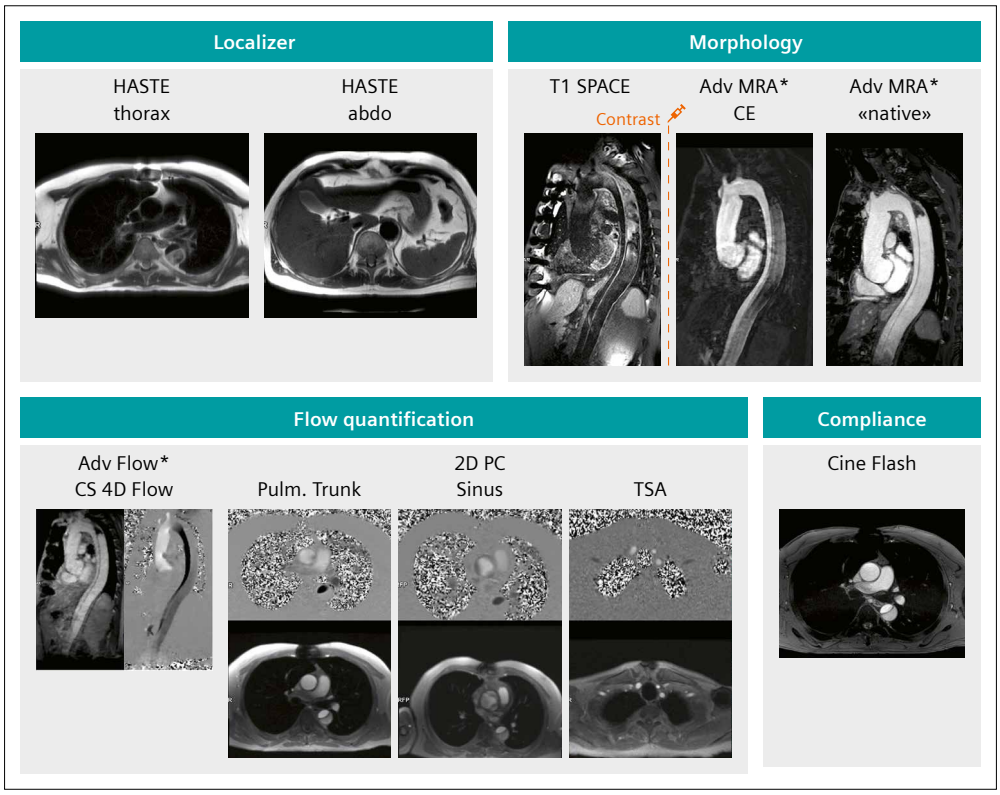

1 Overview of the proposed imaging workflow and sequence acquisition order. When contrast agent administration was indicated, CE-MRA was performed first, followed by CS 4D flow MRI and native MRA acquisitions. This acquisition strategy was designed to take advantage of the residual intravascular contrast enhancement, thereby improving SNR for both native angiographic imaging and subsequent 4D flow analysis.

Fat–water separation was achieved using a two-point Dixon technique, which provides improved robustness to magnetic field (B0) inhomogeneities compared to conventional fat saturation methods.

Native MRA was acquired in two steps to cover both the thoracic and abdominal aorta for Type B aortic dissection while limiting off-center induced artifacts. To reduce overall examination time, abdominal native MRA was acquired without respiratory triggering (ECG gating), as motion artifacts in this region were considered less critical than in the thoracic aorta, where respiratory motion plays a more significant role in image quality degradation.

For patients eligible for contrast material administration, and particularly in the context of initial evaluation of aortic aneurysm or dissection, a CE-MRA acquisition was incorporated into the protocol. The administration of a gadolinium-based contrast agent was leveraged to both improve morphological assessment and enhance the signal characteristics of subsequent native angiographic sequences and 4D flow MRI acquisitions. Although breath-holding would have led to better image quality, CE-MRA was deliberately performed with free-breathing for patient comfort. Acquisition of CE-MRA took between 8 and 12 seconds on average.

4D flow MRI (Advanced Flow*)

Hemodynamic analysis was performed using a time-resolved three-dimensional phase-contrast MRI acquisition, referred to as 4D flow MRI. This technique enables both visualization and quantification of blood flow velocities throughout the entire volume of interest, providing a comprehensive characterization of flow patterns within the aorta and its true and false lumens.

To overcome the conventional limitations of 4D flow MRI — particularly the prolonged acquisition times and restricted velocity sensitivity — a combined strategy using CS and multi-VENC acquisition was implemented. This approach enables simultaneous encoding of multiple velocity ranges (dual VENC in our case), allowing accurate depiction of both high-velocity flow (e.g., in the true lumen or entry jets) and low-velocity flow (e.g., within the false lumen), which may otherwise be underestimated with a single VENC setting.

Sequence parameters for both Advanced MRA and Advanced 4D Flow sequences can be found in Table 1.

** Work in progress. The application is still under development and not commercially available. Its future availability cannot be ensured.*

Sequences	CE-MRA	Native MRA	4D Flow
FOV (readout × phase)	350 × 263 mm	350 × 295 mm	450 × 313 mm
In-plane spatial resolution	1.4 x 1.4 mm (recon. 0.7 mm)	1.0 × 1.0 mm	2.0 × 2.0 mm
Slice thickness	1 mm	1 mm	2 mm
Slice resolution	50%	100%	68%
Phase resolution	100%	100%	75%
Acceleration factor	CS – 9	CS – 7	CS – [7.5-7.8]
Bandwidth	781 Hz/px	799 Hz/px	531 Hz/px
Flip angle	30°	15°	10°
TR/TE	492.8 ms/1.78 ms	219.2 ms/1.48 ms/3.07 ms	45.5 ms/2.41 ms
Segments	128	25	2
Specific parameters	–	Prep. T2 35 ms (2 × MLEV4) Dixon fat saturation	Flow mode: Free VENC: 4 Vit. 1 = 250 cm/s Vit. 2 = 250 cm/s Vit. 3 = 250 cm/s Vit. 4 = 100 cm/s Dir. 1 through plane Dir. 2 A >> P Dir. 3 F >> H Dir. 4 F >> H

Table 1: 3T sequence parameters for Advanced MRA* and Advanced 4D Flow*.

Results

Aortic dissection

An example of Type A aortic dissection (male patient, 77 years old) is shown in Figure 2 with results from T1 SPACE (2A), CE-MRA (2B), and native angiography (acquired after contrast agent, 2C). On CE-MRA, the resulting contrast between perfused and non-perfused regions facilitates more accurate identification of true and false channels, thereby improving diagnostic confidence. In addition, T1 SPACE imaging provides complementary information to further refine morphological assessment. The arrowhead shows the area of stagnant flow in the false lumen. These findings are consistent with observations from computed tomography angiography (CTA, 2D), supporting the robustness and clinical reliability of CE-MRA and non-CE MRA for initial assessment. The longitudinal follow-up of this patient after surgery is shown in Figure 2E. False lumen is no longer visible.

Another example of residual Type B aortic dissection after surgery for Type A (male patient, 55 years old, ascending aorta replacement) is reported in Figure 3, showing T1 SPACE (3A), CE-MRA (3B and 3C, maximum intensity projection (MIP)), native MRA (3D, acquired after contrast injection), and CS 4D flow (3E). Here again, the combination of angiographic imaging and blackblood acquisition strengthens the anatomical characterization of aortic dissections and contributes to a more accurate evaluation of disease extent and morphology. Of note, T1 SPACE demonstrates areas of incomplete blood signal suppression within the false lumen (arrowheads), corresponding to stagnant flow and resulting in a heterogeneous or partially blurred appearance. In addition, the use of contrast agent contributes to increased signal-to-noise ratio (SNR) in 4D flow MRI acquisitions, which may be advantageous for the analysis of complex flow patterns. A fused reconstruction combining native MRA of the thoracic and abdominal

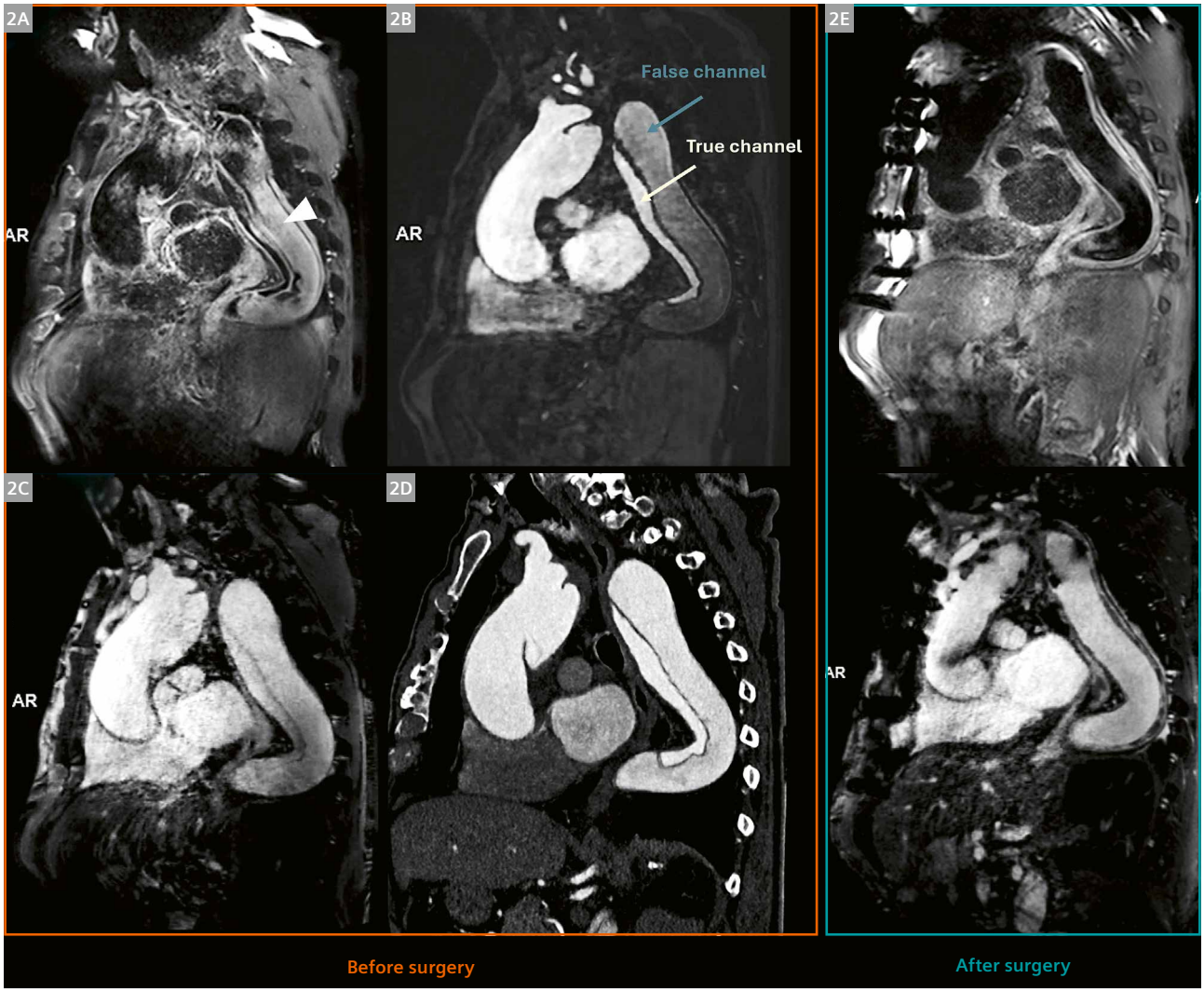

2 Example of aortic dissection of Type A before surgery **(2A–2D)** and after surgery **(2E)**.

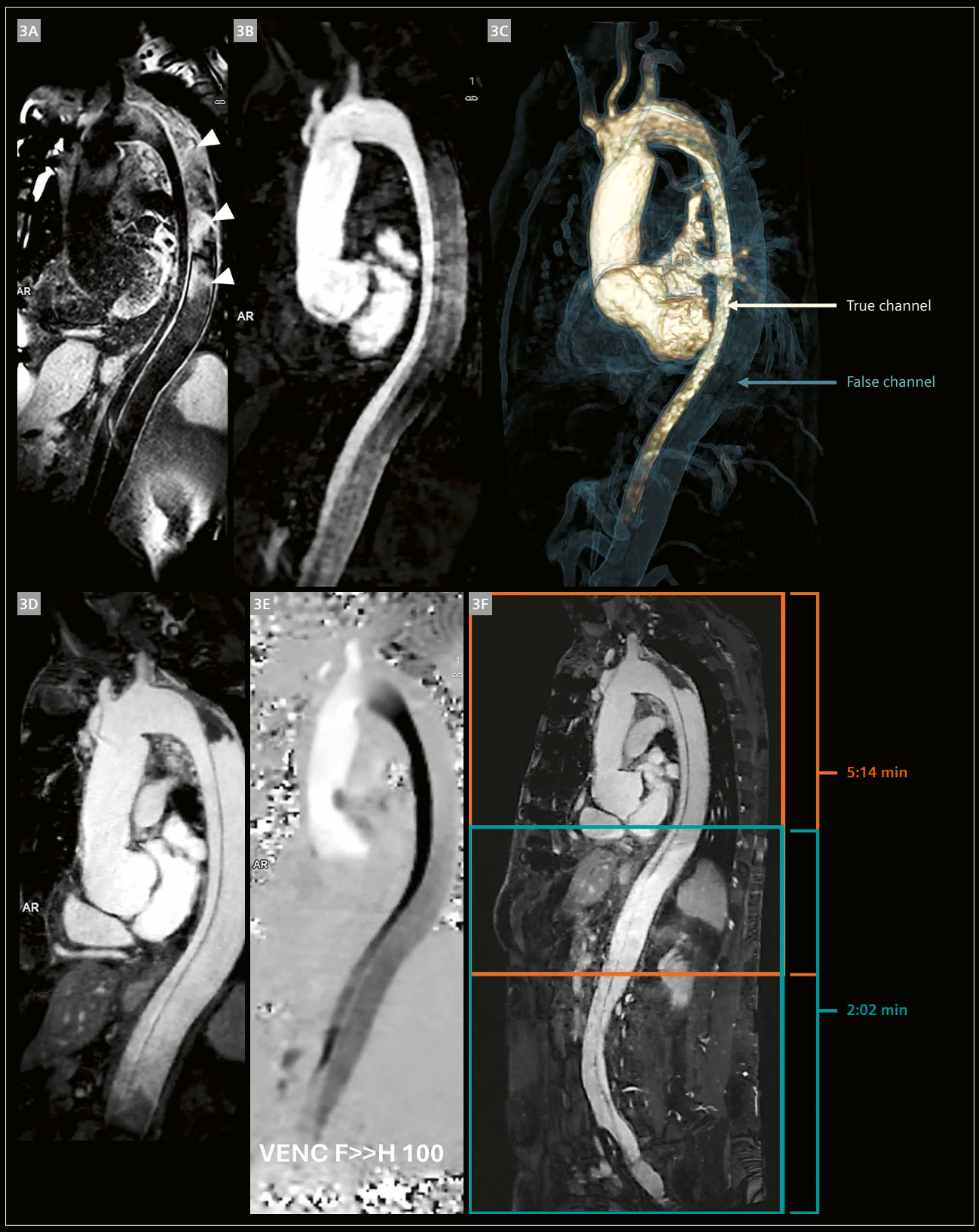

3 Example of residual Type B aortic dissection after surgery for Type A. T1 SPACE **(3A)**, CE-MRA **(3B and 3C MIP)**, and native MRA **(3D)** acquired after contrast injection and CS 4D flow **(3E)** are displayed. The two-step native MRA (thoracic and abdominal aorta **(3F)**) was acquired in approximately 7 minutes.

aorta (3F) highlights the full extent and longitudinal propagation of the dissection in this patient, along with the acquisition time of each step.

A third example of dissection is provided in Figure 4, which illustrates the case of a 41-year-old male patient with a de novo acute Stanford Type B aortic dissection and pathogenic MYH11 gene mutation [7]. The acceleration provided by CS allowed acquisition of thoraco-abdominal native MRA within a scan time of approximately 5 minutes, while maintaining sufficient image quality. Such coverage is particularly valuable in patients with extensive aortic dissections, where accurate visualization of the longitudinal propagation of the disease is essential for diagnosis and follow-up.

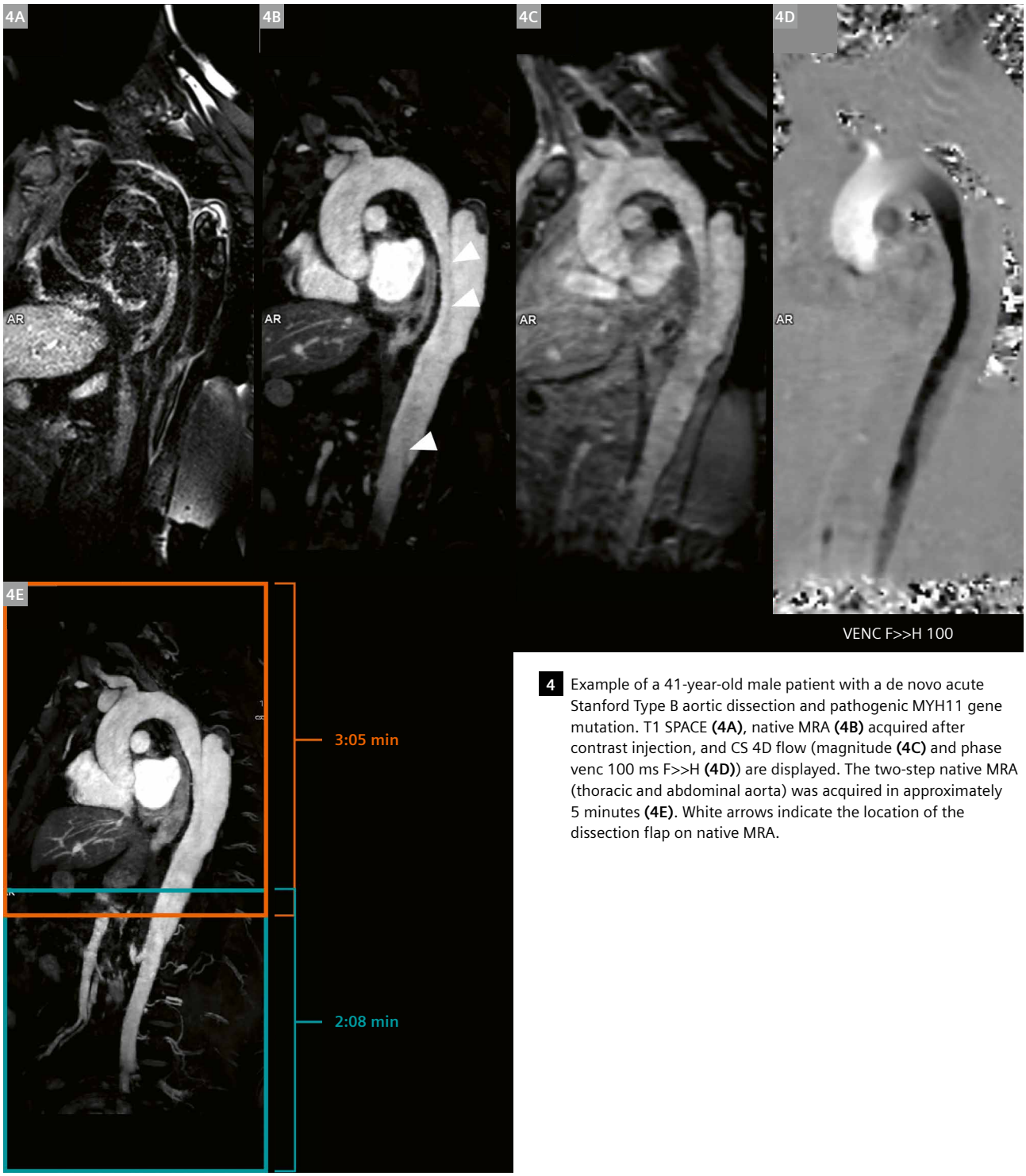

4 Example of a 41-year-old male patient with a de novo acute Stanford Type B aortic dissection and pathogenic MYH11 gene mutation. T1 SPACE **(4A)**, native MRA **(4B)** acquired after contrast injection, and CS 4D flow (magnitude **(4C)** and phase venc 100 ms F>>H **(4D)**) are displayed. The two-step native MRA (thoracic and abdominal aorta) was acquired in approximately 5 minutes **(4E)**. White arrows indicate the location of the dissection flap on native MRA.

Thoracic aortic aneurysm

Figure 5 illustrates a patient (female, 82 years old) with an aneurysm of 51 mm, a bicuspid valve (seen on the 2D phase-contrast image in 5E) and a Grade 1 aortic insufficiency. The exam was performed the day before surgery. This figure shows native angiography (non-CE MRA without contrast agent, 5A), CE-MRA (5B), CS 4D flow MRI (magnitude and phase, 5C and 5D), with the segmentation automatically done on the native angiography and on the CS 4D flow MRI. It clearly depicts the strength of the native angiography with CS. In addition, our method for automatic segmentation of the aorta, which is based on deep learning, allows for a precise segmentation of the aorta on this sequence (Fig. 6) but also on the magnitude images of the CS 4D flow MRI [8] (6B). Figure 7 displays the resulting blood velocity at peak systole (7A) as the wall

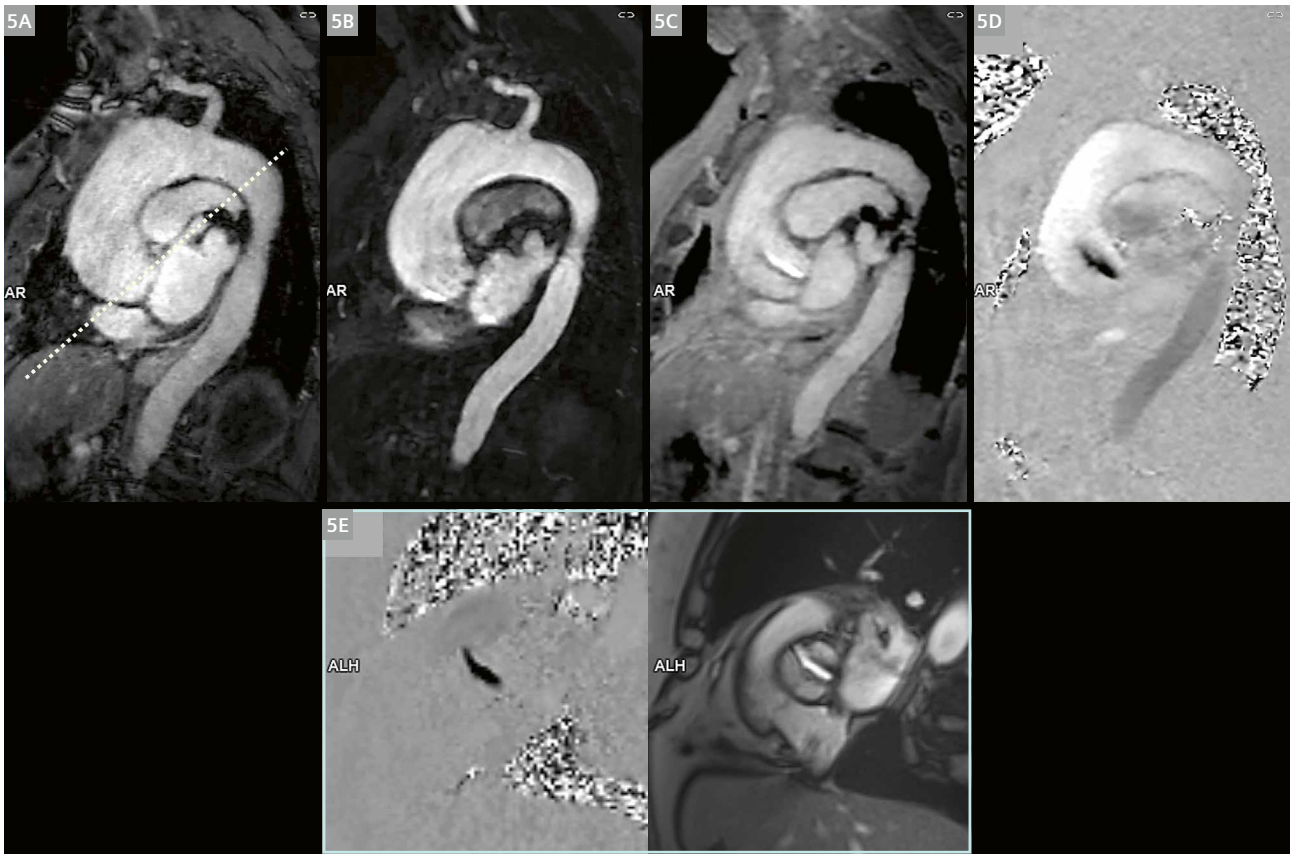

5 An 82-year-old female patient with an aneurysm of 51 mm, a bicuspid valve (seen on the 2D phase-contrast image, **5E**) and a Grade 1 aortic insufficiency.

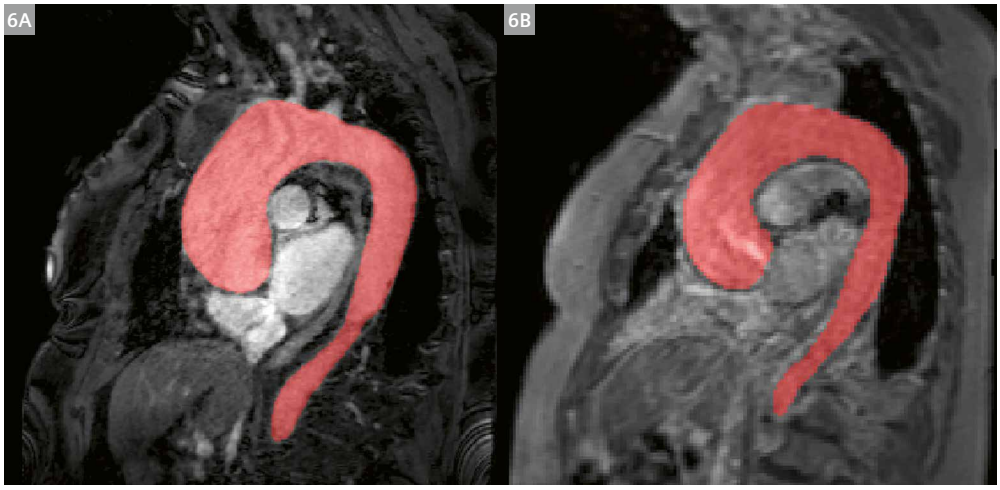

6 Automatic segmentation of the aorta on native angiography **(6A)** and on magnitude images of 4D flow MRI **(6B)** in the same patient as in Figure 5 (female, 82 years old, aneurysm with bicuspid valve).

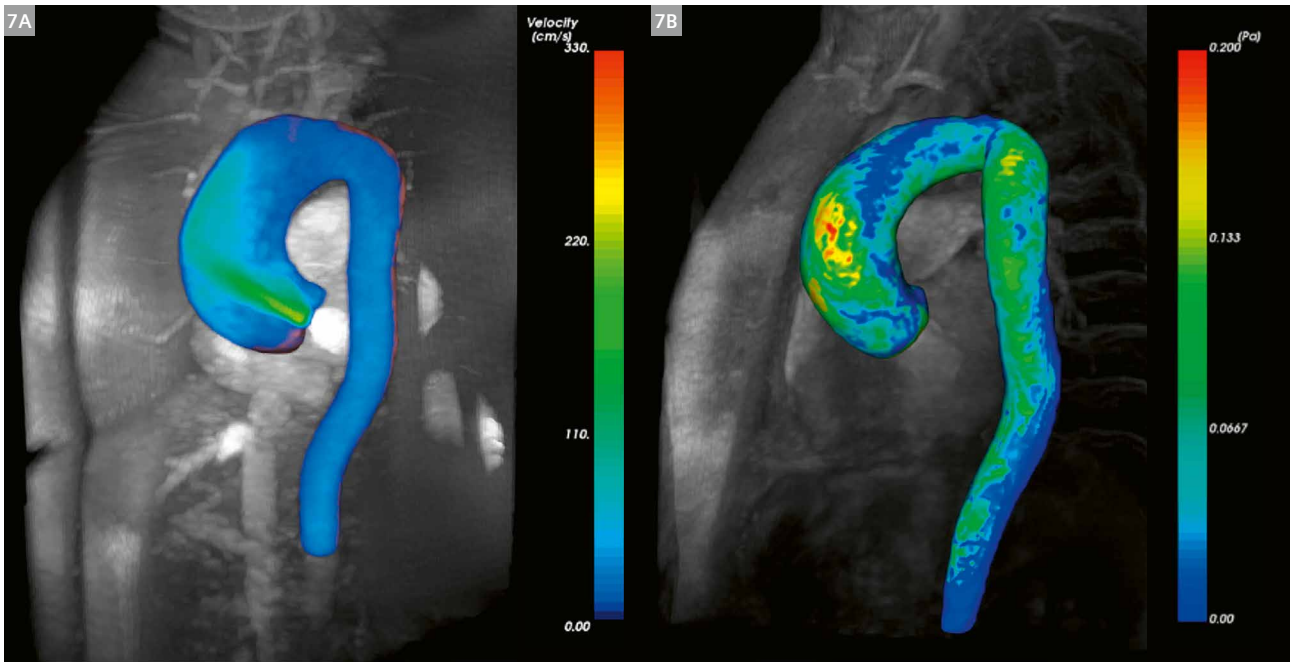

7 Display of the blood velocity at peak systole (**7A**, scale [0–330] cm/s) as the wall shear stress (**7B**, pressure scale [0–0.2] Pa), in the same patient as in Figure 5 (female, 82 years old, aneurysm with bicuspid valve).

shear stress (7B) computed from the CS 4D flow series. Figure 8 illustrates the reduction in acquisition time (almost 50%) that was achieved with the CS 4D Flow* (6:31 min vs 12:46 min) while maintaining satisfactory image quality.

A further example of aortic root aneurysm is presented in Figure 9, in a patient with associated aortic regurgitation and Grade 2 aortic insufficiency. CE-MRA (9A) and native MRA with contrast material (9B and 9E) demonstrate the aneurysmal dilatation and provide comprehensive anatomical assessment of the thoracic aorta. Aortic dimensions could be measured on axial cine flash images (9D), although this sequence is used for aortic compliance assessment, while flow images magnitude (9F) and phase, venc 250 in-plane (9G) clearly depict the regurgitant jet associated with aortic valve insufficiency. Beyond conventional flow visualization, advanced hemodynamic biomarkers can also be derived from CS 4D flow MRI. Figures 9G and 9I illustrate the peak velocity distribution and WSS, respectively, providing complementary information on the interaction between blood flow and the aortic wall that may contribute to a more comprehensive assessment of aneurysmal disease.

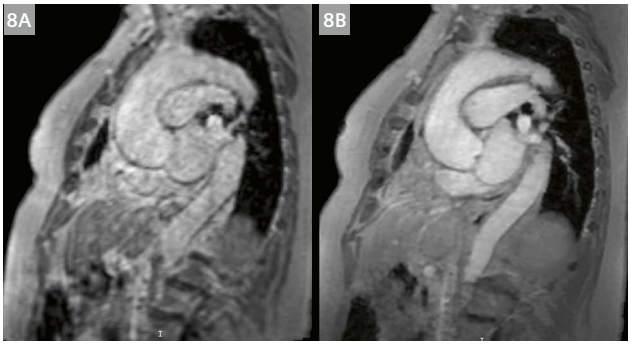

8 Difference between the 4D flow sequence without CS (**8A**, acquisition time 12:46 min) and with CS (**8B**, acquisition time 6:31 min) in the same patient during the same examination.

Clinical value of Compressed Sensing

The application of CS to both MRA and 4D flow MRI represents a significant advancement in aortic imaging. By enabling substantial acceleration of data acquisition through undersampling of *k*-space combined with iterative reconstruction, CS effectively reduces scan duration, which is a critical limitation of conventional techniques. This reduction in acquisition time not only improves patient comfort and workflow efficiency but also mitigates the impact of respiratory variability and motion artifacts, which are common sources of image degradation in aortic imaging. Although acquisition time remains dependent on the patient's physiological condition, particularly their heart rate and respiratory pattern, in our experience the mean acquisition time for both MRA and 4D flow imaging was approximately 7 minutes, with the shortest acquisitions around 5 minutes. In addition, the intrinsic regularization associated with CS reconstruction contributes to improved image consistency and robustness, particularly in patients with complex or tortuous aortic anatomy. As a result,

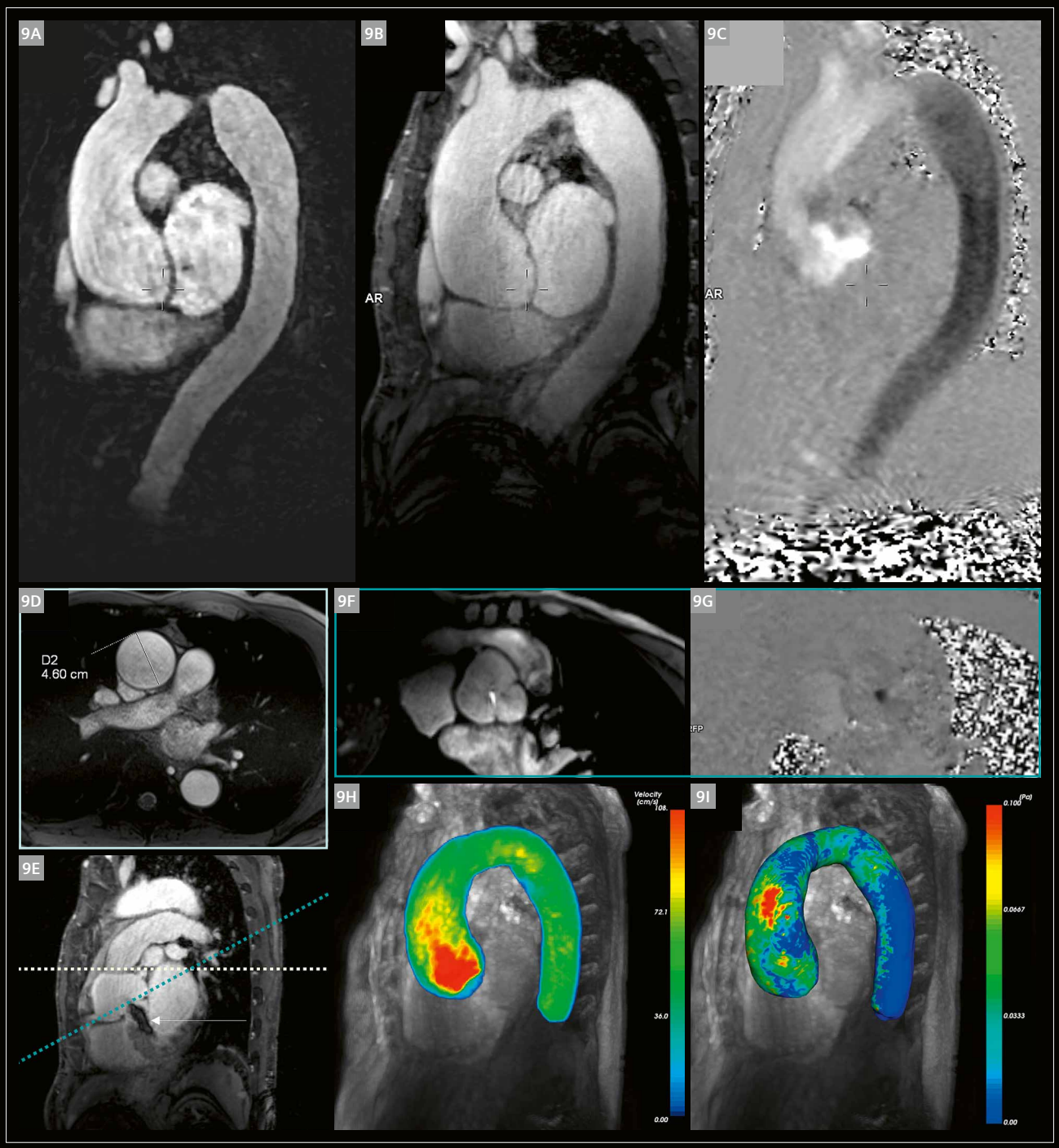

9 A 72-year-old male patient with an aneurysm of 46 mm and an aortic insufficiency. CE-MRA **(9A)**, native MRA **(9B and 9E)** acquired after contrast material, CS 4D flow venc 250 F>>H **(9C)**, transversal cine flash **(9D)**, 2D flow phase contrast (PC) (magnitude **9F** and phase venc 250 in-plane **9G**), peak velocity (**9H**, scale [0–108] cm/s), and wall shear stress (**9I**, scale [0–0.1] Pa). White arrow on native MRA **(9E)** depicts the regurgitant jet associated with aortic valve insufficiency.

high-quality morphological and hemodynamic datasets can be obtained even in challenging clinical scenarios.

Combination of native MRA and 4D flow

The isotropic resolution of the native angiographic sequence makes it easy to perform registration with 4D flow images (considering the diastolic phase). This may be relevant for evaluating parameters such as wall shear stress or for computational fluid dynamics (CFD) applications. Indeed, for the latter, the 3D modelling could be obtained from the native angiographic sequence, and the inlet as outlet conditions from 4D flow MRI. Plus, the advent of artificial intelligence (AI) should make it possible to automatically segment different structures (non-dissected aorta with or without aneurysm, true and false lumen), but it requires a sufficiently large database with the corresponding annotations to train a deep learning model. Our experience shows very good results [9] (Fig. 6).

Conclusion

The combination of CS-accelerated MRA and 4D flow MRI represents a major step forward in the comprehensive imaging of complex aortic diseases, both for initial assessment and longitudinal follow-up. Compared to conventional contrast-enhanced MRA, the native angiographic sequence offers several key advantages: high signal-to-noise ratio, excellent lumen-to-wall contrast, no requirement for gadolinium-based contrast agents, free-breathing acquisition, and high isotropic spatial resolution. The addition of 4D flow MRI with multi-VENC acquisition further extends the diagnostic value of the examination. Beyond flow visualization, this sequence supports the quantification of biomechanical parameters such as wall shear stress — key biomarkers for predicting aneurysmal progression and guiding personalized surgical decision-making. The complementarity between these two sequences, combined with deep learning-based automatic segmentation, opens the door to a fully integrated workflow, from morphological assessment to hemodynamic quantification and wall-shear-stress mapping, within a single, clinically feasible examination. This dual-sequence approach has consistently demonstrated its clinical relevance across a broad spectrum of pathological presentations.

Contact

Alain Lalande, Ph.D., MCU-PH Deputy Director
Laboratoire ICMUB (UMR CNRS 6302)
UFR Sciences de Santé
Université Bourgogne Europe
21000 Dijon
France
alain.lalande@u-bourgogne.fr

From a practical standpoint, the use of CS reduces mean acquisition time to approximately 5 to 7 minutes per sequence, improving both patient comfort and robustness to motion. Beyond their value in the MECATHOR and ADEPT research projects, these techniques are mature enough to be considered for broader clinical deployment, both at 1.5T and 3T, offering a reproducible, patient-friendly, and information-rich alternative to CT angiography-based follow-up in patients with severe aortic pathology.

Acknowledgments

Financial support for these studies was provided by the PO FEDER-FSE Bourgogne 2012–2020 program, and for the ADEPT project, co-financed by the European Regional Development Fund (FEDER-FSE+ Bourgogne-Franche-Comté 2021-2027).

References

1 Authors/Task Force Members, Czerny M, Grabenwöger M, Berger T, Aboyans V, Della Corte A, et al. EACTS/STS Guidelines for Diagnosing and Treating Acute and Chronic Syndromes of the Aortic Organ. Ann Thorac Surg [Internet]. 2024;118(1):5–115. Available from: http://dx.doi.org/10.1016/j.athoracsur.2024.01.021

2 Lin S, Morgant MC, Marín-Castrillón DM, Walker PM, Aho Glélé LS, Boucher A, et al. Aortic local biomechanical properties in ascending aortic aneurysms. Acta Biomater [Internet]. 2022;149:40–50. Available from: http://dx.doi.org/10.1016/j.actbio.2022.06.019

3 Morgant M-C, Lin S, Marin-Castrillon D, Bernard C, Laubriet A, Cochet A, et al. Comparison of two techniques (in vivo and ex-vivo) for evaluating the elastic properties of the ascending aorta: Prospective cohort study. PLoS One [Internet]. 2021;16(9):e0256278. Available from: http://dx.doi.org/10.1371/journal.pone.0256278

4 Daily PO, Trueblood HW, Stinson EB, Wuerflein RD, Shumway NE. Management of acute aortic dissections. Ann Thorac Surg [Internet]. 1970;10(3):237–47. Available from: http://dx.doi.org/10.1016/s0003-4975(10)65594-4

5 Kim JB, Kim K, Lindsay ME, MacGillivray T, Isselbacher EM, Cambria RP, Sundt TM 3rd. Risk of rupture or dissection in descending thoracic aortic aneurysm. Circulation [Internet]. 2015; 132(17):1620–9. Available from: http://dx.doi.org/10.1161/CIRCULATIONAHA.114.015177

6 Zeilinger MG, Giese D, Schmidt M, May MS, Janka R, Heiss R, et al. Highly accelerated, Dixon-based non-contrast MR angiography versus high-pitch CT angiography. Radiol Med [Internet]. 2024; 129(2):268–79. Available from: http://dx.doi.org/10.1007/s11547-023-01752-0

7 Zhu L, Vranckx R, Khau Van Kien P, Lalande A, Boisset N, Mathieu F, et al. Mutations in myosin heavy chain 11 cause a syndrome associating thoracic aortic aneurysm/aortic dissection and patent ductus arteriosus. Nat Genet [Internet]. 2006;38(3):343–9. Available from: http://dx.doi.org/10.1038/ng1721

8 Zhou Y, Decourselle T, Barrera-Naranjo A, Bouchot O, Christophe JJ, Lalande A. Automatic Segmentation of the Aorta from 4D-flow MRI Using Deep Learning. Presented at: 17th Congress of Asian Society of Cardiovascular Imaging; September 12–14, 2024; Shanghai, China.

9 Zhou Y, Barrera-Naranjo A, Decourselle T, Marin-Castrillon DM, Presles B, Delcey M, et al. Evaluation of the Automatic Segmentation of Aorta considering Aortic Diameter Measurements from Native MRI Angiographic Images. Presented at: 2025 ISMRM & ISMRT Annual Meeting & Exhibition; May 10–15, 2025; Honolulu, USA

Contrast-Enhanced iNAV MRA for Whole-Chest, Whole-Heart, and Whole-Aortic Imaging: A Single-Center Experience

Jason Craft[1], Timothy Carter[2], Joshua Y. Cheng[1], Christopher J. Moran[3], Karl P. Kunze[4], Michaela Schmidt[5], Rene M. Botnar[6,7,8], Claudia Prieto[6,7]

[1]DeMatteis Cardiovascular Institute, St. Francis Hospital & Heart Center, Roslyn, NY, USA
[2]Department of Cardiothoracic Surgery, Good Samaritan University Hospital, West Islip, NY, USA
[3]Department of Radiology, Good Samaritan University Hospital, West Islip, NY, USA
[4]MR Research Collaborations, Siemens Healthcare Limited, Camberley, United Kingdom
[5]Research & Clinical Translation, Magnetic Resonance, Siemens Healthineers, Erlangen, Germany
[6]School of Biomedical Engineering and Imaging Sciences, King's College London, London, United Kingdom
[7]School of Engineering, Pontificia Universidad Católica de Chile, Santiago, Chile
[8]Institute for Biological and Medical Engineering, Pontificia Universidad Católica de Chile, Santiago, Chile

Introduction

Undersampled 3D whole-heart inversion recovery (IR) Dixon gradient echo (GRE) accelerated by variable-density spiral-like Cartesian trajectory (VD-CASPR) with image-based navigators (iNAVs) for motion estimation and nonrigid motion-corrected iterative sensitivity-encoding (SENSE) reconstruction with 100% respiratory scan efficiency has the potential for integration into workflows for left atrial and left ventricular delayed enhancement [1]. Our initial aim was to develop an iNAV-compatible method to provide complementary contrast-enhanced (CE) pulmonary vein magnetic resonance angiography (MRA) for registration with delayed enhancement and high-quality left atrial segmentation, while being insensitive to flow and off-resonance artifacts. The need was compounded by the shortage of iohexol and iodixanol intravenous contrast media products for computed tomography angiography (CTA) from May to June 2022. Single-contrast saturation-recovery (SR) and IR GRE have been widely used for this purpose with excellent results [2, 3], although experience is relegated to diaphragmatic navigator prospective motion correction. Widespread clinical adoption has been constrained by commonly recognized limitations to this approach, including an unpredictable scan duration, and residual respiratory motion due to the inaccurately assumed slab tracking ratio. As a solution, we collaborated with our partners at Siemens Healthineers, at Pontificia Universidad Católica de Chile, and at King's College London to configure both SR and IR GRE for iNAV pulmonary vein CE-MRA, later adapting the IR GRE method for whole-chest angiography (iNAV CE-MRA) [4].

For the majority of patients, 3D non-contrast-enhanced T2-prepared balanced steady-state free precession (bSSFP) provides highly diagnostic image quality. However, iNAV CE-MRA has several key advantages that warrant consideration for use. These include a lack of dependency on chemically selective fat saturation preparatory pulses, which may inadvertently saturate the water signal in the aortic arch and proximal descending aorta [5]; and demonstrably superior blood pool signal uniformity, allowing performance consistency of threshold-based anatomical segmentation used to generate centerline semi-automated aortic measurements (CSAMs). iNAV CE-MRA can also be combined with time-resolved angiography with interleaved stochastic trajectories (TWIST) for comprehensive dynamic 4D angiography. Given the rapidly shifting landscape of modern MR imaging, referral patterns, provider needs, and the increase in patient complexity, it is also increasingly important to have techniques that are robust to susceptibility artifacts from sources such as internal cardiac defibrillators (ICDs)/pacemakers[1], thoracic endovascular aortic repairs (TEVAR)[1], and hybrid aortic repairs. That being said, the technical downside to iNAV CE-MRA is variation in image

[1] *The MRI restrictions (if any) of the metal implant must be considered prior to patient undergoing MRI exam. MR imaging of patients with metallic implants brings specific risks. However, certain implants are approved by the governing regulatory bodies to be MR conditionally safe. For such implants, the previously mentioned warning may not be applicable. Please contact the implant manufacturer for the specific conditional information. The conditions for MR safety are the responsibility of the implant manufacturer, not of Siemens Healthineers.*

contrast with irregular rhythms (which can degrade image quality), more elaborate MRA planning, and risk of MR acquisition mistiming in relation to the delivery of gadolinium-based contrast agent (GBCA). To partially alleviate these shortcomings, the artificial intelligence cardiac scan companion (AICSC)[2] WIP and auto resting-phase detection [6] are promising tools to reduce efficiency overhead, and can be used for automated whole-chest slab placement, navigator placement, and alignment of the data window duration. We also favor the use of a simplified injection scheme that is practical for everyday clinical use without contrast dilution, manipulation of extra tubing, syringes, and/or stopcocks. Lastly, it is feasible to monitor GBCA arrival using the low-resolution 2D iNAV images to minimize the possibility of sequence mistiming error.

Protocols

Exams are performed on a MAGNETOM Sola or MAGNETOM Aera 1.5-Tesla scanner (Siemens Healthineers, Erlangen, Germany) with a dedicated 32-channel spine coil and an 18-channel phased array torso coil. In order to minimize confusion and simplify communication across multiple sites where remote scanning is used, a minimal number of core protocols were developed for use regardless of patient complexity.

To date, we have performed over 300 iNAV CE-MRA exams, over 250 of which were whole-chest or whole-aorta imaging. We have three core protocols for whole-chest and whole-aorta MRA imaging:

1) TWIST followed by iNAV CE-MRA: Appropriate for patients with aortic disease limited to the thoracic aorta.
2) First-pass abdominopelvic MRA followed by iNAV CE-MRA: Used in patients with extensive thoracic and abdominal aortic dissection and surgical repair.
3) TWIST followed by iNAV CE-MRA, then first-pass abdominopelvic MRA: Appropriate for patients with extensive thoracic and abdominal aortic dissection, but with TEVAR or hybrid repairs.

Sequence parameters for TWIST and iNAV CE-MRA can be found in Table 1. Before administering GBCA, we test the fidelity of the vectorcardiogram (VCG) gaiting and perform prescan adjustments to be copied to subsequent iNAV scans by running a copy of the sequence for several seconds.

Separate from the test scan, we create identical pairs of iNAV CE-MRA program steps to be run roughly 10 seconds after TWIST completes, which is enough time to give the patient instructions. As our experience matured, we found it was no longer necessary to insert an injector pause between the bolus and continuous GBCA infusion.

[2] *Work in progress. The application is currently under development and is not for sale in the U.S. and in other countries. Its future availability cannot be ensured.*

MRA sequence	TWIST	iNAV CE-MRA	iNAV CE-MRA$_{Isotropic}$
FOV (coronal)	400 × 300 × 160 mm	380 × 380 × 157 mm	360 × 360 × 153 mm
In-plane spatial resolution	1.13 × 1.62 mm	1.31 × 1.31 mm	1.25 × 1.25 mm
Phase oversampling	50%	30%	30%
Slice thickness	2 mm	1.4–1.5 mm	1.2 mm
Slice resolution	54%	90%	100%
Acceleration factor	GRAPPA 3	3.2*	4.1*
Sampling distribution	Elliptical scanning 15% (region A), 20% (region B)	Elliptical scanning	Elliptical scanning
Bandwidth	676 Hz/px	755 Hx/px	755 Hx/px
Flip angle	23°	18°	18°
Inversion time	N/A	200–290 ms	200–290 ms
TE/TR	.9 ms/2.4 ms	1.1 ms/3.34 ms	1.17 ms/3.44 ms
Data window duration	N/A	130 ms**	130 ms**

Table 1: Imaging parameters for whole-chest TWIST and iNAV CE-MRA.
*Acceleration factor is increased as needed to fit an acquisition duration of ≤ 5 minutes.
**Data window duration is adjusted as needed according to the optimal cardiac rest period.

The first program step is run to completion if continuous infusion peaking is already evident on the low-resolution inline-display 2D images (this makes the second program step unnecessary). Otherwise, the second program step is run to completion and will need to be triggered at the peak of the continuous infusion via the stop-and-continue function on the inline display (Fig. 1).

iNAV CE-MRA can also be acquired without TWIST for single-station whole-chest angiography. It is the experience of others and our own intuition that 0.075 mmol/kg bolus of a 1-molar agent at 1 mL/s, followed by 0.075 mmol/kg at 0.10 mL/s, and 20–30 mL/saline at 0.10 mL/s provides excellent results [3]. In this case, the first program step is used only for testing the VCG gating fidelity, making pre-scan adjustments, and monitoring the passage of contrast with the image navigator. The second program step, which will run to completion, is triggered at the peak of the continuous infusion.

1 **Option 1:** TWIST MRA: 0.05 mmol/kg at 2 ml/s of 1 molar GBCA followed by 30 ml saline **or** **Option 2:** First pass MRA abdomen and pelvis: 0.1 mmol/kg at 2 ml/s of 1 molar GBCA followed by 20–30 ml saline

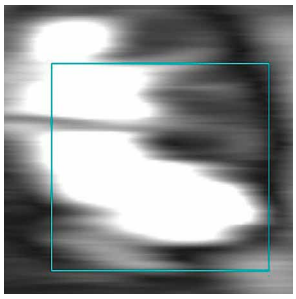

2 Continuous infusion: 0.16 ml/sec GBCA, 20–30 ml saline

3 iNAV CE-MRA

1 molar GBCA dose: 0.1 mmol/kg

1 Method for whole-chest image-based navigator contrast-enhanced magnetic resonance angiography (iNAV CE-MRA). Two identical 3D whole-chest program steps are created in the workflow. **(1)** Following TWIST (Option 1) or first-pass CE-MRA (Option 2), a continuous infusion of gadolinium-based contrast agent (GBCA) begins **(2)**. The first iNAV program step **(3)** commences afterwards and is run to completion only if the continuous infusion arrival is evident on 2D low-resolution images. Otherwise, the required second program step is triggered as the continuous infusion peaks. If TWIST was performed initially (Option 1), first-pass abdominopelvic MRA can be added after iNAV CE-MRA using 0.05 mmol/kg of 1-molar GBCA.

Use of iNAV CE-MRA in challenging patients

Obesity

From 1990 to 2022, obesity rates more than doubled among women and nearly tripled in men. It is estimated that over 1 billion people worldwide are obese, including 159 million children [7].

In the United States alone, obesity-related healthcare expenditures are estimated to be more than $385 billion in 2024 [8].

High-quality MR imaging in this population poses challenges, such as decreased signal-to-noise ratio (SNR) from reduced radiofrequency penetration, larger acquired voxel dimensions, and increased patient-specific field inhomogeneity as magnetic bore sizes are pushed to the limit. The latter directly contributes to phase incoherency artifacts from T2 and fat saturation preparatory pulses, with large-volume shimming having reduced effectiveness across the whole-chest 3D field of view.

Other modalities are also negatively impacted: Echocardiography with poor acoustic windows and inadequate ultrasound penetration depth, and CT with increased beam attenuation resulting in photon starvation and low SNR.

Although GRE generally has an overall lower SNR in several applications, Tandon et al. demonstrated higher intravascular SNR for gadofosveset-enhanced IR GRE compared to 3D T2-prepared bSSFP [9]. It is yet to be determined if this observation translates to weak albumin-binding GBCAs.

In a single-center study consisting of 65 patients with atrial fibrillation referred for CMRI, mean BMI was 30 ± 6 kg/m^2. However, good or excellent quality pulmonary-vein iNAV CE-MRA was obtained in 95% of exams. Additionally, good or excellent left atrial segmentation was seen in 97% of exams [10].

This helps support the use of MRA in a population that is vulnerable to higher effective radiation doses needed for routine medical imaging [11].

High-quality whole-chest iNAV CE-MRA may also be realized in this patient population. Figure 2 demonstrates two examples where iNAV CE-MRA produced high-quality imaging despite body habitus.

Endografts and implantable cardiac devices[1]

TEVAR is considered first-line therapy for the treatment of complicated Type B aortic dissection (TBAD) and descending thoracic aortic aneurysms [12]. Although the metallic frame structure is readily visible on CT imaging, time-resolved MRA has higher sensitivity for the detection of endoleaks [13]. It is common to encounter intravascular dephasing within the TEVAR using iNAV CE-MRA, but not with TWIST. This signal loss is related to metallic artifact, non-laminar flow, and thus intravoxel velocity heterogeneity. Therefore, TWIST and iNAV CE-MRA are combined for arterial, venous, and delayed phase imaging (Figs. 3, 4). While a TEVAR nitinol exoskeleton composition produces relatively small susceptibility artifacts, the opposite is true regarding ICDs and pacemakers.

Over 200,000 ICDs and 1 million cardiac pacemakers are implanted every year worldwide [14]. Approximately 200,000 cardiac pacemakers are implanted in the United States alone [15], posing a challenge to conventional CMR imaging.

MRA imaging in device patients has historically been an underexplored topic of interest, possibly due to many existing systems containing non-MR-conditional generators or leads. As a consequence, this population may be exposed to recurring doses of ionized radiation (i.e., for annual aortic surveillance).

For these patients, a modified wideband IR pulse with a spectral bandwidth of 2–6 kHz has shown benefit for 3D delayed enhancement, and may have a role in whole-chest angiography [16]. An IR frequency offset may be helpful in shifting artifacts away from pertinent anatomical structures, at the cost of IR efficiency and loss of image contrast. Examples of iNAV CE-MRA with and without wideband IR are found in figures 5, 6, and 7. In contrast, TWIST is more robust due to lack of IR pulse and shorter repetition time, and can provide diagnostic information in areas affected by artifacts on iNAV CE-MRA.

[1] *The MRI restrictions (if any) of the metal implant must be considered prior to patient undergoing MRI exam. MR imaging of patients with metallic implants brings specific risks. However, certain implants are approved by the governing regulatory bodies to be MR conditionally safe. For such implants, the previously mentioned warning may not be applicable. Please contact the implant manufacturer for the specific conditional information. The conditions for MR safety are the responsibility of the implant manufacturer, not of Siemens Healthineers.*

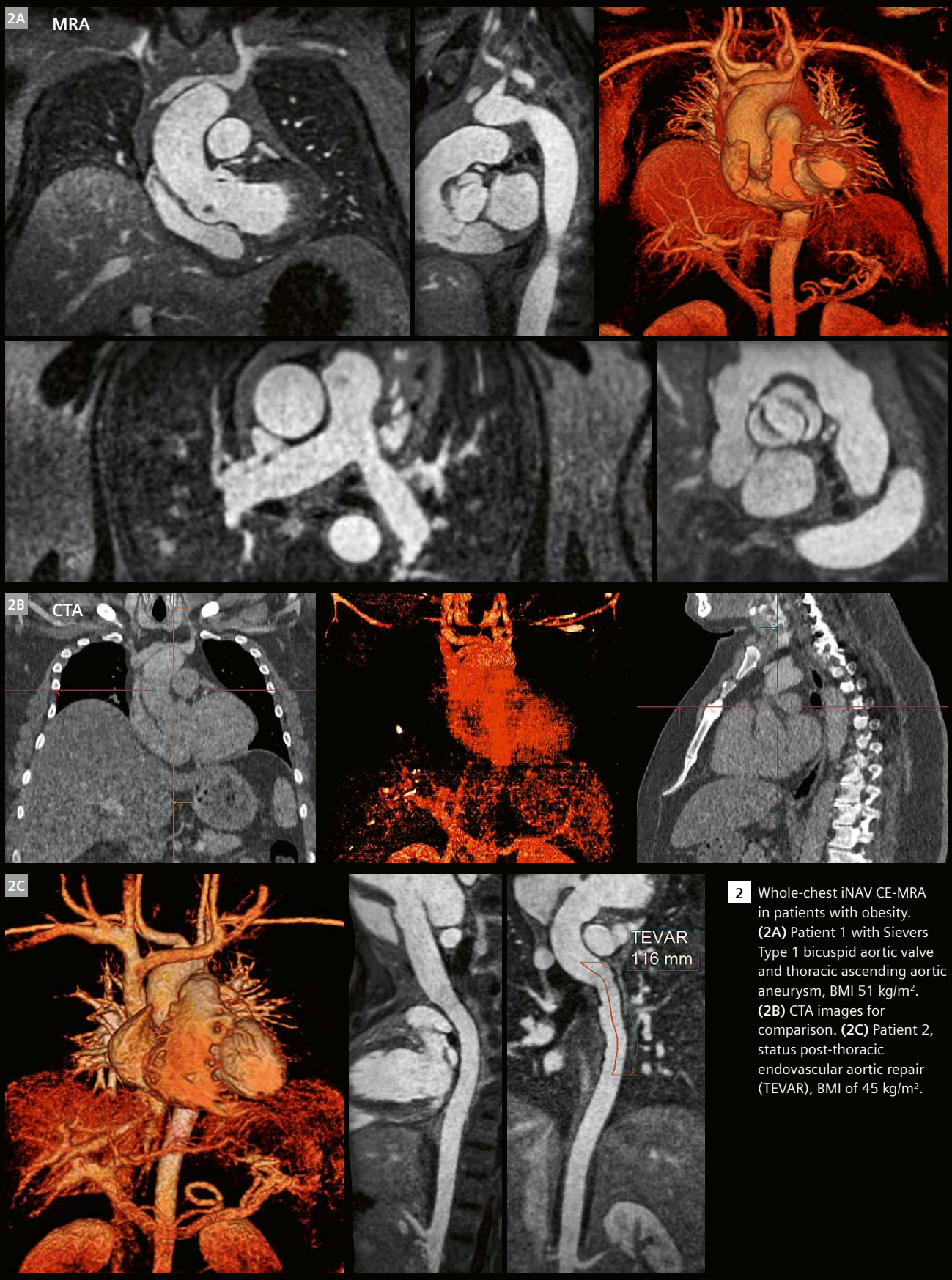

2 Whole-chest iNAV CE-MRA in patients with obesity. **(2A)** Patient 1 with Sievers Type 1 bicuspid aortic valve and thoracic ascending aortic aneurysm, BMI 51 kg/m². **(2B)** CTA images for comparison. **(2C)** Patient 2, status post-thoracic endovascular aortic repair (TEVAR), BMI of 45 kg/m².

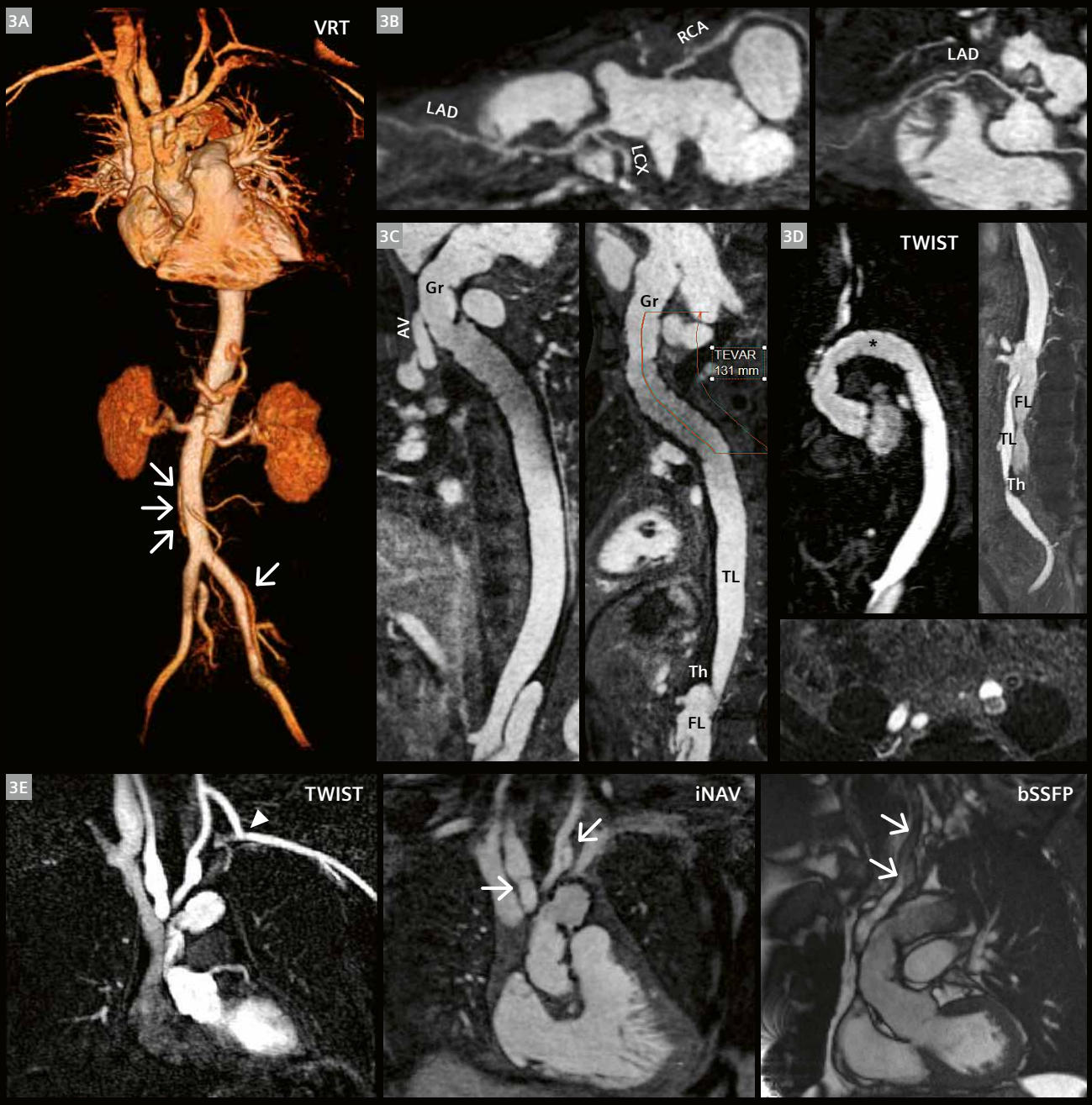

3 A 57-year-old male, Type A aortic dissection, status post-hybrid repair with debranching of the supra-aortic vessels, left common carotid to left subclavian bypass. **(3A)** Composite volume rendering (VRT) of the iNAV and first-pass CE-MRA. **(3B)** The left anterior descending (LAD) artery, right coronary artery (RCA), and left circumflex coronary artery (LCX) are free from dissection. **(3C)** An interposition graft (Gr) is present in the ascending aorta with composite reconstructed arch vessel (AV). The thoracic endovascular aortic repair (TEVAR) graft spanning 131 mm is present in the thoracic descending aorta. Loss of intravascular signal intensity is appreciated within the TEVAR graft. Residual aortic dissection is present in the abdominal aorta, where the true lumen (TL) and false lumen (FL) containing thrombus (Th) can be identified. **(3D)** Compared to iNAV CE-MRA, there is no appreciable signal loss within the TEVAR graft (black asterisk) on arterial phase TWIST. First-pass abdominopelvic CE-MRA redemonstrates the true lumen, false lumen, thrombus, and dissection extension to the level of the common iliac artery. **(3E)** TWIST demonstrates patent left common carotid to left subclavian bypass (white arrowhead). iNAV CE-MRA depicts residual dissection in the brachiocephalic and left common carotid arteries (white arrows). In contrast, balanced steady-state free precession (bSSFP) images are affected by dephasing artifacts in the supra-aortic vessels.

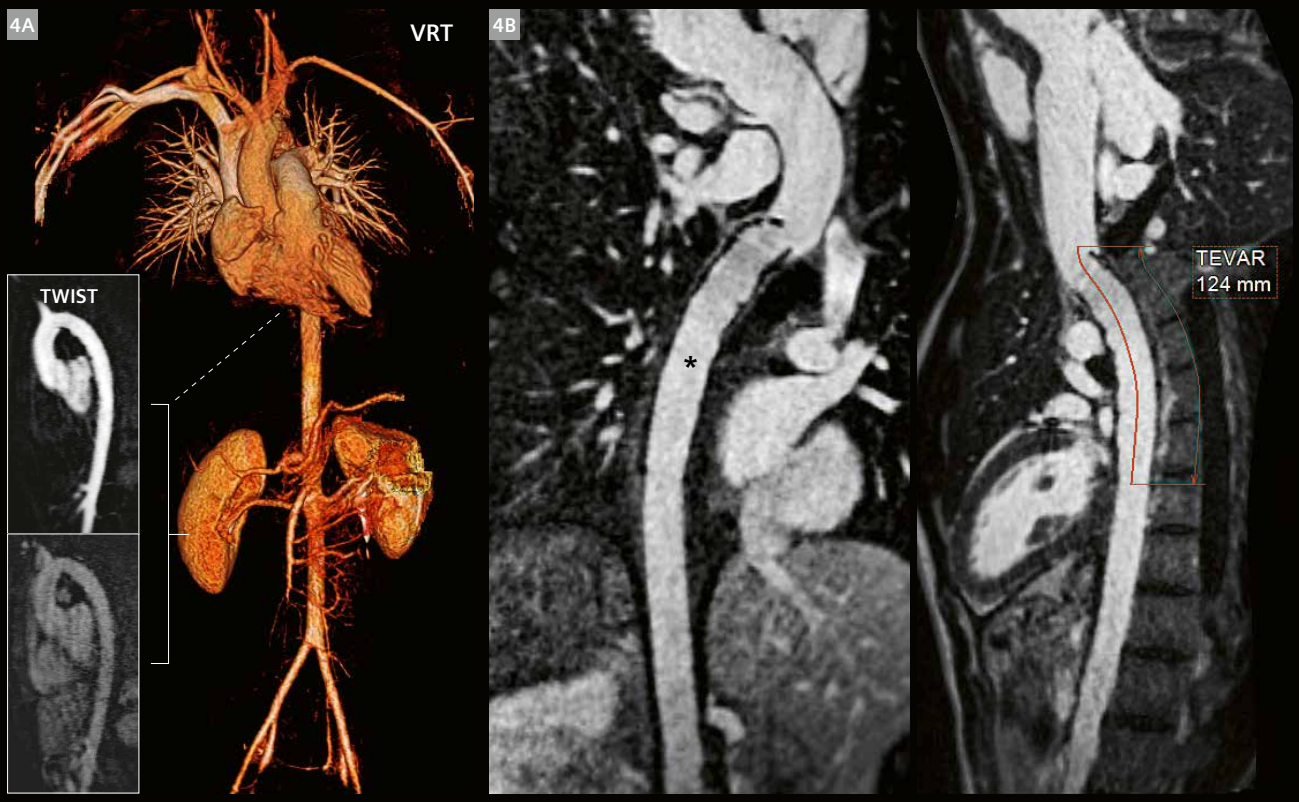

4 iNAV CE-MRA in a patient status post-thoracic endovascular aortic repair (TEVAR). **(4A)** Composite volume rendering (VRT) of iNAV and first-pass abdominopelvic CE-MRA. The inset images demonstrate arterial and venous TWIST phases. There is no evidence of endoleak. **(4B)** Curved multiplanar reconstructions (MPRs) demonstrate the TEVAR graft spanning 124 mm. Minor signal intensity loss is present within the graft (asterisk). **(4C)** Coronal and sagittal maximal intensity projections (MIPs) of the abdominal aorta, which is free from pathology.

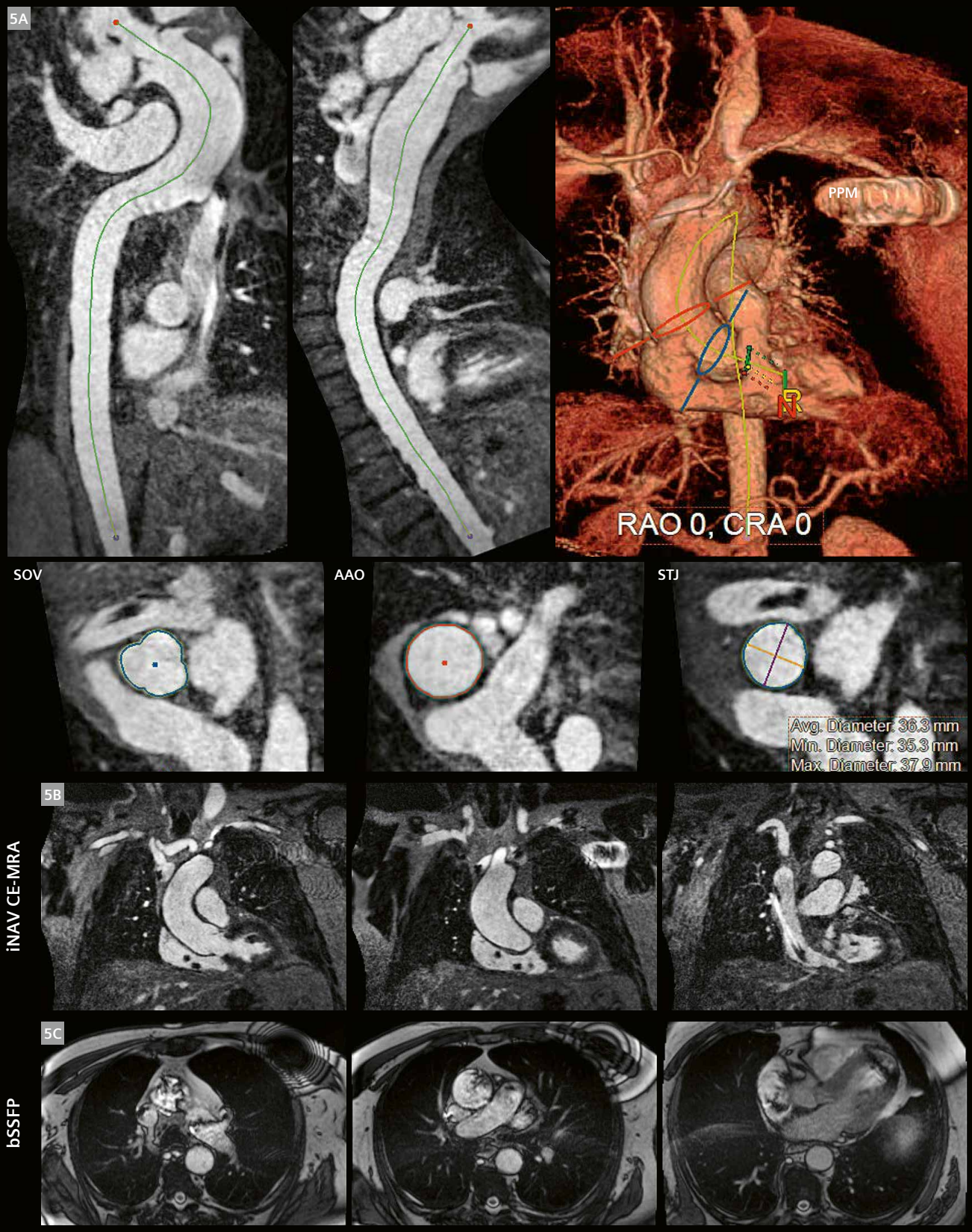

5 **(5A)** iNAV CE-MRA without wideband inversion recovery. Centerline semiautomated aortic measurements (CSAM) in a patient with permanent cardiac pacemaker. **(5B)** iNAV CE-MRA is free from significant artifact in the pertinent anatomical structures compared to balanced steady-state free precession (bSSFP) **(5C).**

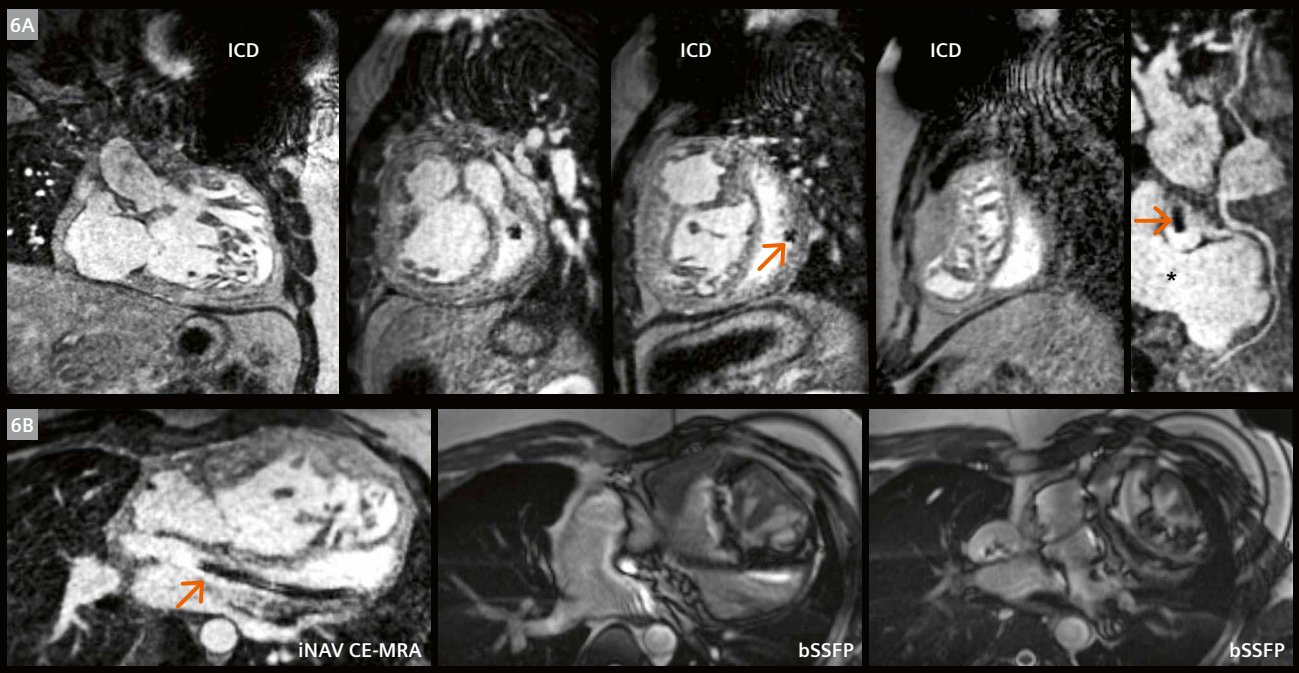

6 A 46-year-old male with a history of D-transposition of the great arteries, status post-atrial switch procedure. Systemic outflow tract **(6A)** and short-axis views demonstrate enlargement of the systemic ventricle and large signal void artifact from the internal cardiac defibrillator (ICD). The coronary artery origins are normal, with demonstration of systemic venous baffle patency and ICD lead within (orange arrows). The pulmonary venous baffle (asterisk) is also widely patent. Extensive artifact is present on balanced steady-state free precession (bSSFP) images compared to wideband iNAV CE-MRA **(6B)**.

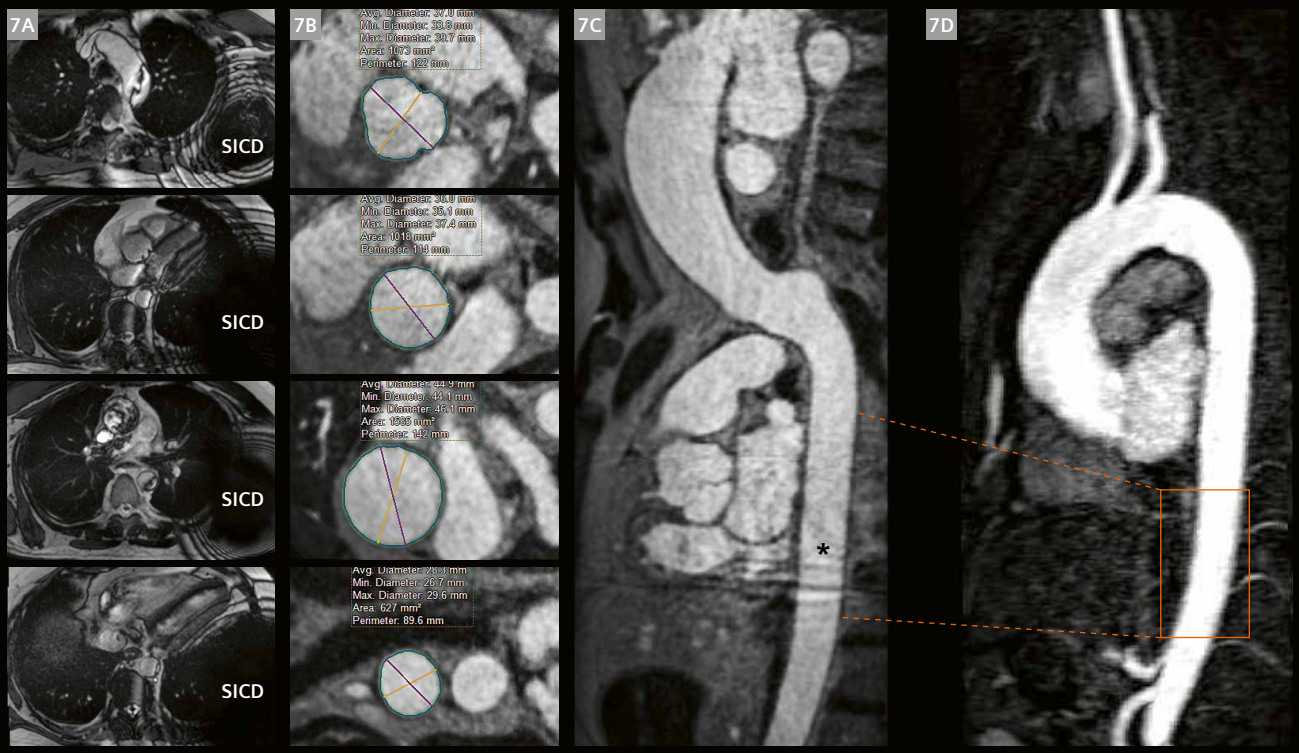

7 A 59-year-old male with subcutaneous internal cardiac defibrillator (SICD). **(7A)** Balanced steady-state free precession (bSSFP) axial images contain extensive artifacts. **(7B)** Centerline semiautomated aortic measurements (CSAM) of the sinus of Valsalva, sinotubular junction, ascending aorta, and arch are still feasible. **(7C)** With use of wideband iNAV CE-MRA, rippling artifacts (asterisks) were still present, overlaying the thoracic descending aorta; however, **(7D)** time-resolved MRA is free from artifacts.

Full aortic imaging

Lifelong aortic surveillance is needed after surgical repair or for medically treated disease. Full-field-of-view coronal imaging is not adequate to capture the entire aorta, arch vessels, and iliofemoral vessels in all patients. Therefore, a combination of acquisitions is often necessary.

Several non-contrast techniques have been used for abdominopelvic MRA. IR inflow techniques are most suitable for small-volume acquisitions. Quiescent-interval single-shot (QISS), with bSSFP, or radial FLASH readout can be acquired with breath-hold or free breathing, respectively, although the former is susceptible to inhomogeneity artifacts. Furthermore, all the above techniques require cardiac gating, which reduces acquisition efficiency. More recent developments include ungated 3D T2-prepared Dixon GRE. However, navigator gating and a comparatively longer repetition time likewise decrease the efficiency of the technique. While large-volume non-contrast techniques require an acquisition duration that spans several minutes, first-pass CE-MRA can be performed in a single breath-hold.

First-pass CE-MRA can be readily combined with iNAV CE-MRA with or without TWIST (Figs. 3, 4, 8, and 9) to provide extended coverage since aortic dissection and manifestations of systemic illnesses may not be isolated to the thoracic region (Fig. 10). Without TWIST, arterial and venous phase high-resolution abdominopelvic CE-MRA images are acquired with Care Bolus, immediately followed by iNAV CE-MRA. Without injector pause, the 0.1 mmol/kg GBCA continuous infusion is administered after the initial contrast/saline bolus combination. Because first-pass MRA is acquired with 0.1 mmol/kg of GBCA, (instead of the standard TWIST dose of 0.05 mmol/kg), the extra intravascular signal is used to acquire iNAV CE-MRA at 1.2 mm isotropic spatial resolution with higher acceleration factor and no overall increase in acquisition duration. Figure 9 is an example of full aortic imaging acquired using first-pass abdominopelvic MRA followed by iNAV CE-MRA at 1.2 mm isotropic spatial resolution.

For TEVAR hybrid repairs, TWIST is important for evaluation of the endograft. For this protocol, we start with the standard TWIST using 0.05 mmol/kg of 1-molar contrast agent with 30 mL saline, followed by 0.1 mmol/kg GBCA infusion for iNAV CE-MRA without delay. This is followed by Care Bolus and first-pass CE-MRA of the abdomen and pelvis with the remaining 0.05 mmol/kg GBCA.

Combined iNAV CE-MRA and LGE imaging

Many conditions, such as hypertension, vasculitis, and atherosclerotic disease, affect the thoracic vasculature and have downstream effects on the myocardium. Depending on the indication or clinical question, both thoracic MRA and cardiac MRI may be required within the same exam (Fig. 11). Tissue characterization with delayed enhancement imaging and extracellular volume fraction provide highly desirable information; therefore, it may be preferable to acquire gated MRA using GBCA. iNAV CE-MRA is compatible with the typical workhorses of the CMR imaging suite, such as bSSFP cine, post-contrast T1 parametric mapping, and late gadolinium enhancement.

Assessing intracardiac anatomy

4D flow has proven effective in quantifying hemodynamic properties across a large volume of anatomical coverage, given the ability to retrospectively prescribe any slice plane for analysis. Characterization of relatively low intracardiac velocities is most impacted by limited velocity-to-noise ratio (VNR) without GBCA at 1.5T. Technical adjustments may be required to increase acquired voxel size and to lower the acceleration factor and/or the receiver bandwidth as compensation. The proposition of highly undersampled *k*-space acquisition with Compressed-Sensing reconstruction is especially attractive, given the significantly shorter acquisition time. Compared to conventional 4D flow, there is significant underestimation of mitral-valve forward and net volumes, early-to-active left ventricular filling velocity ratio [17], aortic-valve forward volume, peak aortic systolic velocity [18], and higher noise values with increasing acceleration factors [19]. As a contrast-enhanced technique, iNAV CE-MRA provides the secondary benefit of boosting 4D flow SNR by up to 1.8× [19], which can be traded for higher spatiotemporal fidelity. Additionally, a key advantage of gated iNAV CE-MRA is the assessment of intracardiac structure and anatomical defects. These include atrial and ventricular septal defects, and arteriovenous connections. The high-resolution anatomic information is complementary to phase-contrast MRI quantitative flow data (Fig. 12).

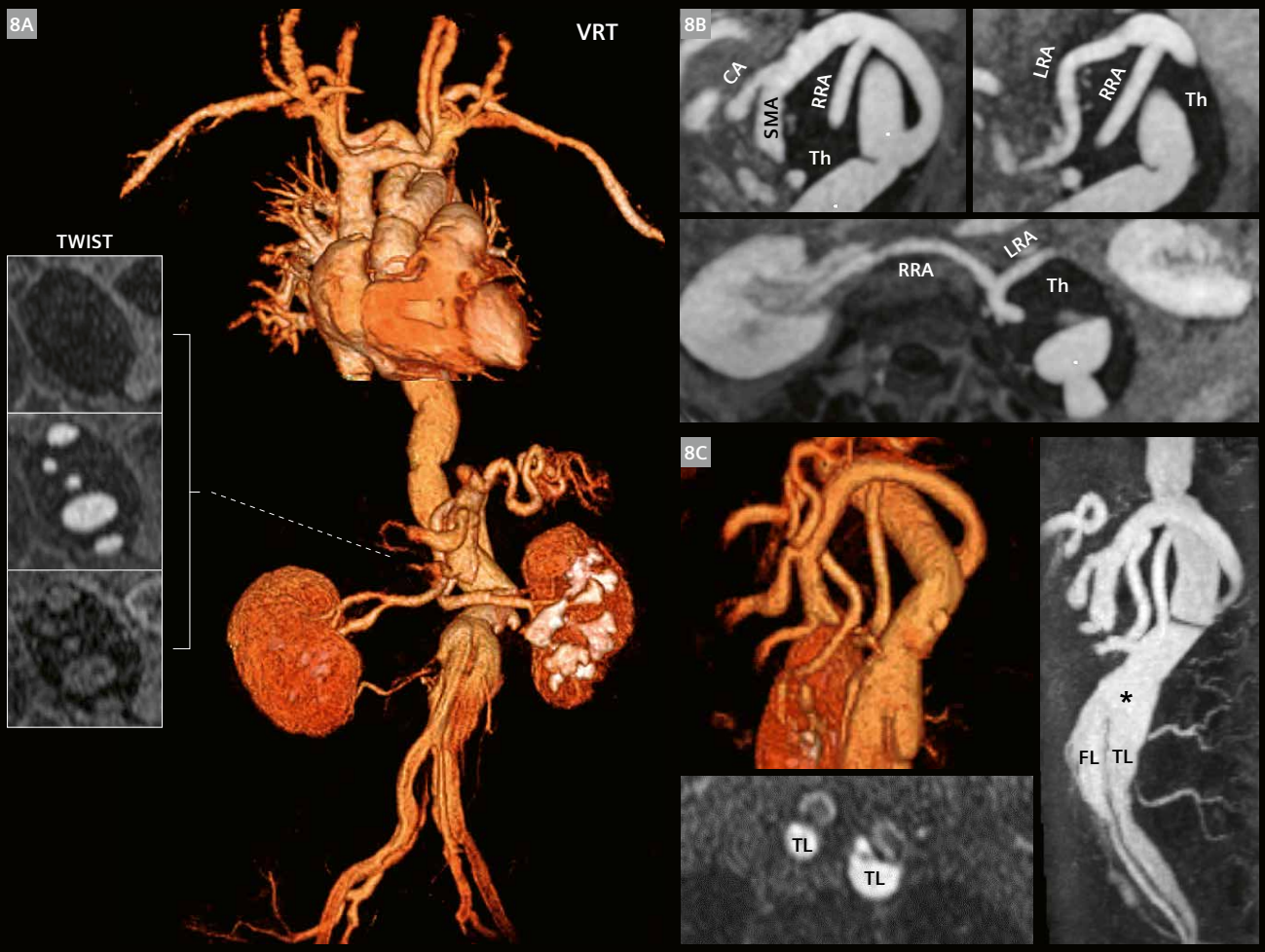

8 A 57-year-old male, history of extensive Type A dissection, status post-repair of the ascending aorta, aortic arch repair with debranching of the supra-aortic vessels, debranching of the abdominal aorta, repair of dissecting abdominal aortic aneurysm with inclusion graft and anastomosis of the celiac, superior mesenteric, and renal arteries. **(8A)** Combined volume rendering (VRT) of the chest and abdominopelvic stations. (Inset) TWIST confirms exclusion of the aneurysmal sac on arterial and venous phase imaging. **(8B)** The celiac artery (CA), superior mesenteric artery (SMA), right renal artery (RRA), and left renal artery (LRA) as depicted by iNAV CE-MRA maximum intensity projection (MIP). Thrombus (Th) is present in the excluded aneurysmal sac. **(8C)** First-pass abdominopelvic MRA VRT and MIP. There is residual infrarenal dissecting abdominal aortic aneurysm (asterisk) with identification of the true lumen (TL) and false lumen (FL). The dissection continues to the level of the common iliac arteries. **(8D)** iNAV CE-MRA demonstrates that the left anterior descending (LAD) artery and the right coronary artery (RCA) are free of dissection. Mild aortic regurgitation is present (orange arrow). Interposition grafts are present in the ascending aorta and arch (Gr) with reconstruction of a composite arch vessel (AV). The inclusion graft (white arrows) and excluded aneurysmal sac with thrombus are redemonstrated in the abdominal aorta.

9 A 58-year-old male with a history of Type A aortic dissection, status post-repair. Whole-chest acquisition duration was 4.84 minutes with 1.2 mm isotropic acquired spatial resolution. **(9A)** Volume rendering (VRT) of the combined iNAV and first-pass CE-MRA with coverage to the level of the femoral vessels. Residual aortic dissection extending to the right common iliac artery and infrarenal aortic aneurysm is visible (white arrows). **(9B)** Complex to-and-fro flow patterns across the dissection flap (white asterisk) result in dephasing artifacts on balanced steady-state free precession (bSSFP) images. Susceptibility artifacts from sternal wires also encroach into the aortic arch intravascular space (white arrows). **(9C)** The right coronary artery (RCA), left anterior descending (LAD) artery, and left circumflex (LCX) artery are free from dissection. **(9D)** In comparison to bSSFP, iNAV CE-MRA curved multiplanar reconstructions (MPRs) are free from significant artifacts. Distal to the ascending aortic graft (Gr) insertion, the dissection flap (black asterisk), false lumen (FL), and true lumen (TL) can be visualized. **(9E)** Maximal intensity projection (MIP) of first-pass abdominopelvic MRA demonstrates continuation of aortic dissection of true lumen (TL) and false lumen (FL) to the abdominal aorta.

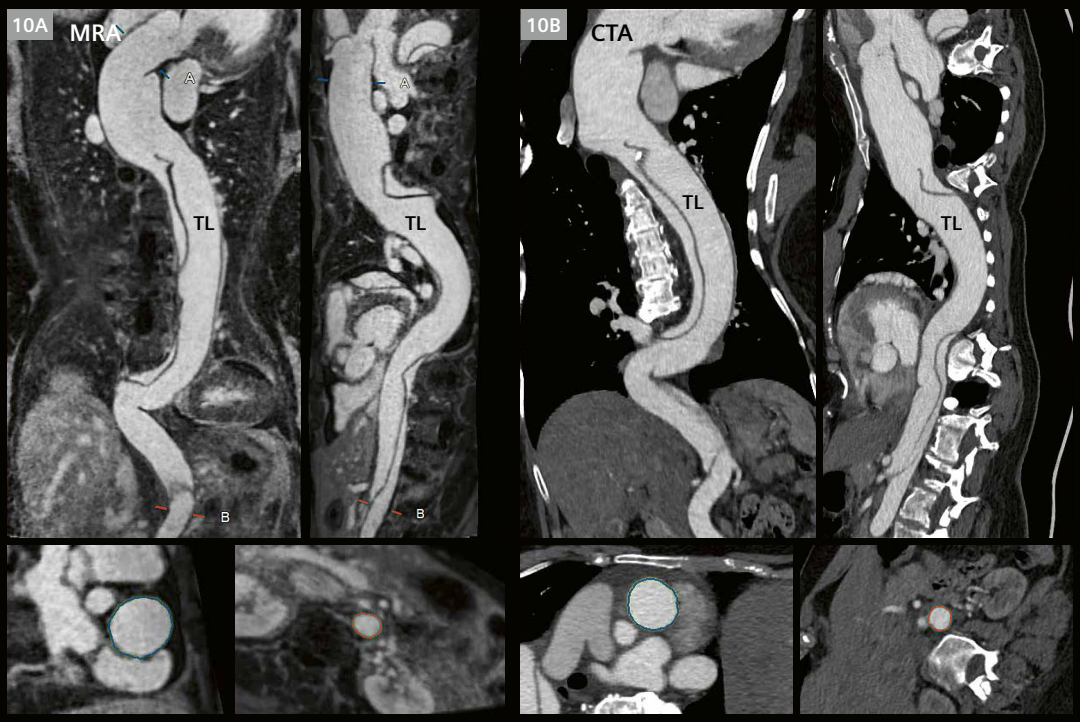

10 Comparison of iNAV CE-MRA **(10A)** and CTA **(10B)** curved multiplanar reconstruction (MPR) images in a patient with Type A aortic dissection extending beyond the thoracic station.

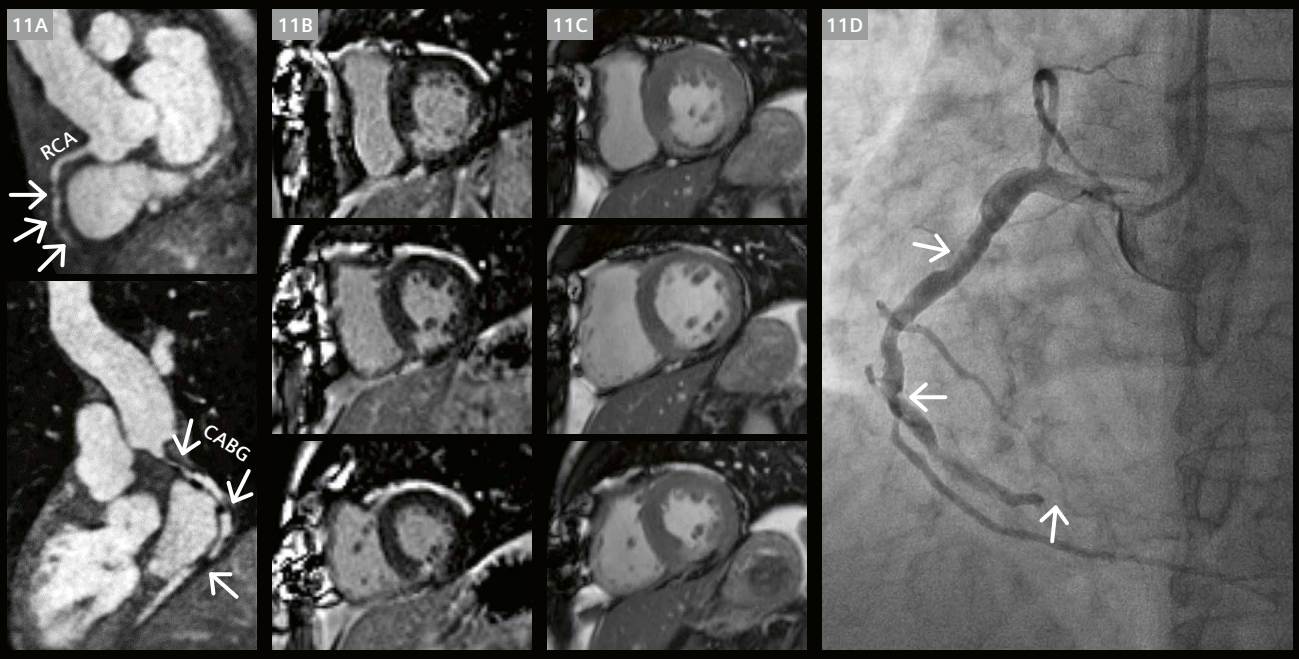

11 A 62-year-old male with a history of coronary artery disease and coronary artery bypass grafts. **(11A)** Multifocal stenosis and midvessel occlusion (white arrows) are present in the right coronary artery (RCA), with severe disease of the coronary artery bypass graft (CABG) to posterior descending artery (white arrows). **(11B, 11C)** Late gadolinium enhancement and cine images respectively demonstrate inferior wall myocardial infarction. **(11D)** Invasive coronary angiogram in the same patient with corresponding stenosis and occlusion of the mid-RCA (white arrows).

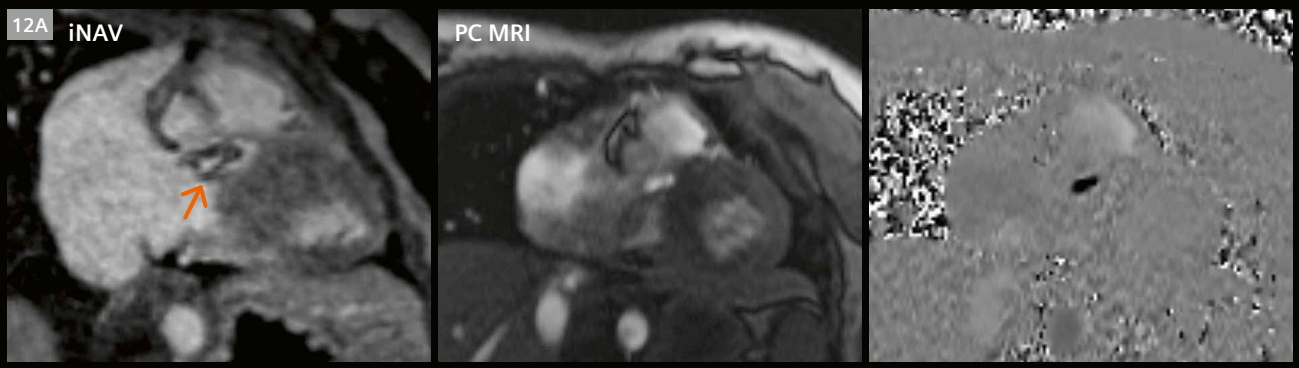

Right lower | Left upper | Left lower | Right upper

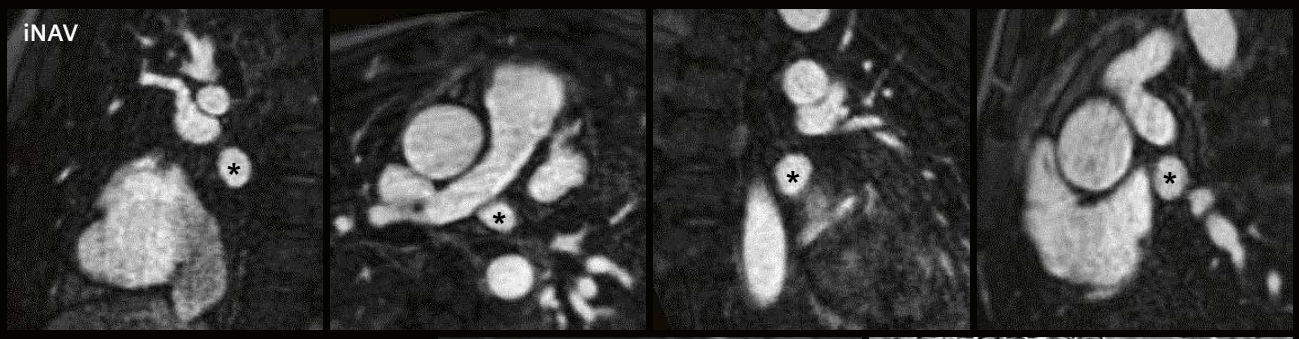

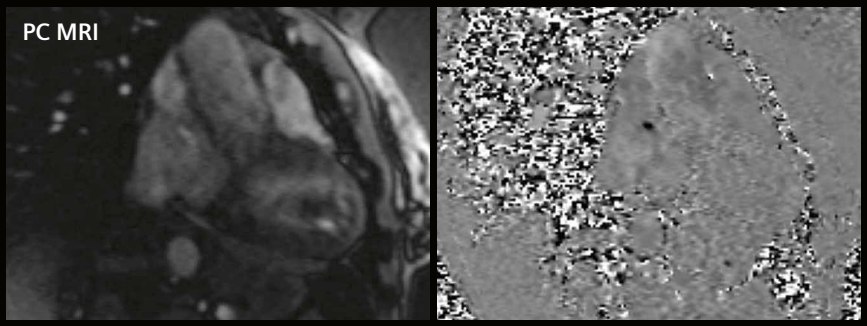

12 iNAV CE-MRA example cases of simple congenital heart disease. **(12A)** Membranous ventricular septal defect and **(12B)** large secundum atrial septal defect as seen with iNAV CE-MRA and phase contrast (PC) MRI. **(12C)** Small secundum atrial septal defect with normal right-lower, left-upper, left-lower, and right-upper pulmonary venous return (asterisk).

In summary, with the iNAV/VD-CASPR framework gated MRA can be performed with 100% respiratory efficiency and thus with a predictable acquisition duration. Both non-contrast and contrast-enhanced techniques have been used, each with its own distinct advantages and disadvantages. iNAV CE-MRA can be combined with TWIST and abdominopelvic first-pass CE-MRA for dynamic information and/or extended coverage, respectively. Based on our single-center experience, this allows for versatile and efficient imaging that shows promise in complex patients with extensive aortic repairs, obesity, and implantable cardiac devices and is robust to magnetic field inhomogeneity and local susceptibility artifacts.

References

1 Munoz C, Bustin A, Neji R, Kunze KP, Forman C, Schmidt M, et al. Motion-corrected 3D whole-heart water-fat high-resolution late gadolinium enhancement cardiovascular magnetic resonance imaging. J Cardiovasc Magn Reson. 2020;22(1):53.
2 Groarke JD, Waller AH, Vita TS, Michaud GF, Di Carli MF, Blankstein R, et al. Feasibility study of electrocardiographic and respiratory gated, gadolinium enhanced magnetic resonance angiography of pulmonary veins and the impact of heart rate and rhythm on study quality. J Cardiovasc Magn Reson. 2014;16(1):43.
3 Siebermair J, Kholmovski EG, Sheffer D, Schroeder J, Jensen L, Kheirkhahan M, et al. Saturation recovery-prepared magnetic resonance angiography for assessment of left atrial and esophageal anatomy. Br J Radiol. 2021;94(1123):20210048.
4 Craft J, Parikh R, Cheng JY, Diaz N, Kunze KP, Schmidt M, et al. Isotropic, high-resolution, whole-chest inversion recovery contrast-enhanced magnetic resonance angiography in under 4.5 min using image-based navigator fluoro trigger. Front Cardiovasc Med. 2025;12:1549275.
5 Bley TA, Wieben O, François CJ, Brittain JH, Reeder SB. Fat and water magnetic resonance imaging. J Magn Reson Imaging. 2010;31(1):4–18.
6 Wood G, Pedersen AU, Kunze KP, Neji R, Hajhosseiny R, Wetzl J, et al. Automated detection of cardiac rest period for trigger delay calculation for image-based navigator coronary magnetic resonance angiography. J Cardiovasc Magn Reson. 2023;25(1):52.
7 NCD Risk Factor Collaboration (NCD-RisC). Worldwide trends in underweight and obesity from 1990 to 2022: a pooled analysis of 3663 population-representative studies with 222 million children, adolescents, and adults. Lancet. 2024;403(10431):1027–1050.
8 Thorpe KE, Joski PJ. Estimated Reduction in Health Care Spending Associated With Weight Loss in Adults. JAMA Netw Open. 2024;7(12):e2449200.
9 Tandon A, Hashemi S, Parks WJ, Kelleman MS, Sallee D, Slesnick TC. Improved high-resolution pediatric vascular cardiovascular magnetic resonance with gadofosveset-enhanced 3D respiratory navigated, inversion recovery prepared gradient echo readout imaging compared to 3D balanced steady-state free precession readout imaging. J Cardiovasc Magn Reson. 2016;18(1):74.
10 Craft J, Weber J, Li Y, Cheng JY, Diaz N, Kunze KP, et al. Inversion recovery and saturation recovery pulmonary vein MR angiography using an image based navigator fluoro trigger and variable-density 3D cartesian sampling with spiral-like order. Int J Cardiovasc Imaging. 2024;40(6):1363–1376.
11 Sperry BW, Vamenta MS, Gunta SP, Thompson RC, Einstein AJ, Castillo M, et al. Influence of Body Mass Index on Radiation Exposure Across Imaging Modalities in the Evaluation of Chest Pain. J Am Heart Assoc. 2024;13(8):e033566.
12 Mazzolai L, Teixido-Tura G, Lanzi S, Boc V, Bossone E, Brodmann M, et al. 2024 ESC Guidelines for the management of peripheral arterial and aortic diseases. Eur Heart J. 2024;45(36):3538–3700.
13 Habets J, Zandvoort HJ, Reitsma JB, Bartels LW, Moll FL, Leiner T, et al. Magnetic resonance imaging is more sensitive than computed tomography angiography for the detection of endoleaks after endovascular abdominal aortic aneurysm repair: a systematic review. Eur J Vasc Endovasc Surg. 2013;45(4):340–50.
14 Ammannaya GKK. Implantable cardioverter defibrillators – the past, present and future. Arch Med Sci Atheroscler Dis. 2020;5:e163–e170.
15 Bhatia N, El-Chami M. Leadless pacemakers: a contemporary review. J Geriatr Cardiol. 2018;15(4):249–253.
16 Ibrahim EH, Runge M, Stojanovska J, Agarwal P, Ghadimi-Mahani M, Attili A, et al. Optimized cardiac magnetic resonance imaging inversion recovery sequence for metal artifact reduction and accurate myocardial scar assessment in patients with cardiac implantable electronic devices. World J Radiol. 2018;10(9):100–107.
17 Varga-Szemes A, Halfmann M, Schoepf UJ, Jin N, Kilburg A, Dargis DM, et al. Highly Accelerated Compressed-Sensing 4D Flow for Intracardiac Flow Assessment. J Magn Reson Imaging. 2023;58(2):496–507.
18 Neuhaus E, Weiss K, Bastkowski R, Koopmann J, Maintz D, Giese D. Accelerated aortic 4D flow cardiovascular magnetic resonance using compressed sensing: applicability, validation and clinical integration. J Cardiovasc Magn Reson. 2019;21(1):65.
19 Hess AT, Bissell MM, Ntusi NA, Lewis AJ, Tunnicliffe EM, Greiser A, et al. Aortic 4D flow: quantification of signal-to-noise ratio as a function of field strength and contrast enhancement for 1.5T, 3T, and 7T. Magn Reson Med. 2015;73(5):1864–71.

Contact

Jason Craft, M.D.
Director, Cardiac MRI
Good Samarian University Hospital
West Islip, NY, USA

Associate Director, Cardiac MRI
St Francis Hospital & Heart Center
100 Port Washington Blvd
Roslyn, NY 11576
USA
Jason.craft@chsli.org

Non-Contrast Portal Vein Imaging Using *syngo* NATIVE MR Angiography

Marcelo Fernandes Arêas

Siemens Healthineers, Erlangen, Germany

Evaluation of the portal venous system is an important part of abdominal magnetic resonance imaging (MRI) studies, particularly in patients with chronic liver disease, suspected portal vein thrombosis, or portal hypertension, or before interventional and surgical procedures. Contrast-enhanced MR angiography is commonly used for this purpose; however, in daily practice a non-contrast technique is desirable in many situations. These include impaired renal function, repeated follow-up examinations, limited intravenous access, or even allergies. Ultrasound is often the first-line imaging method, but MRI offers a larger field of view and a better anatomical overview [1, 2].

The aim of our protocol is to provide a reproducible, patient-friendly, and clinically useful examination of the portal venous system without the need for gadolinium. The protocol can be done using a 1.5T or 3T system. The examples below are from two 1.5T systems (MAGNETOM Sola and MAGNETOM Flow) and one 3T system (MAGNETOM Lumina), respectively. We can use either the Contour or Body Matrix coils together with the Spine coil integrated into the table.

We can benefit from BioMatrix Technology integrated into the Spine coil and use the respiratory signal to gate and trigger the data acquisition. You can take the native_trufi3d_tra_resp_trig protocol directly from the Siemens Healthineers protocol tree (Fig. 1). You still have the possibility to use the Resp. control on the Physio card and PACE (Fig. 2).

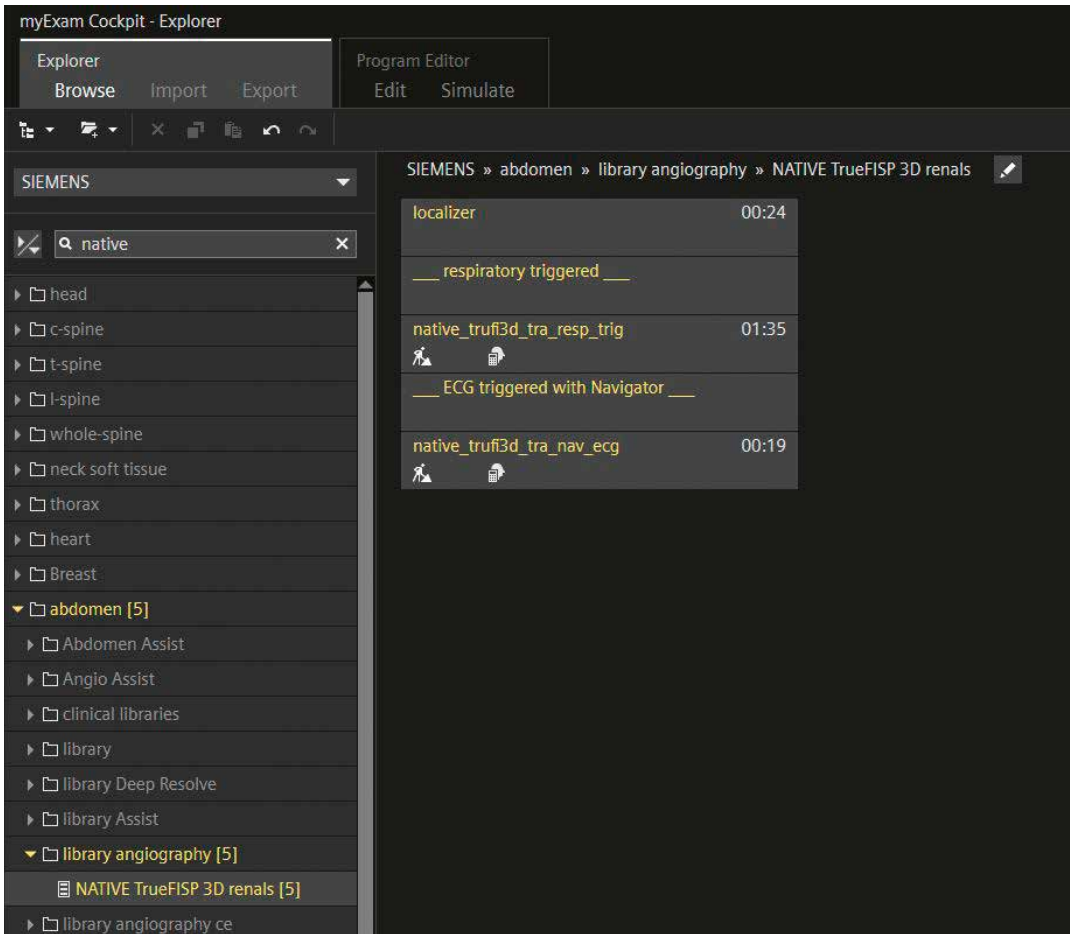

1 Where to find the native_trufi3d_tra_resp_trig protocol.

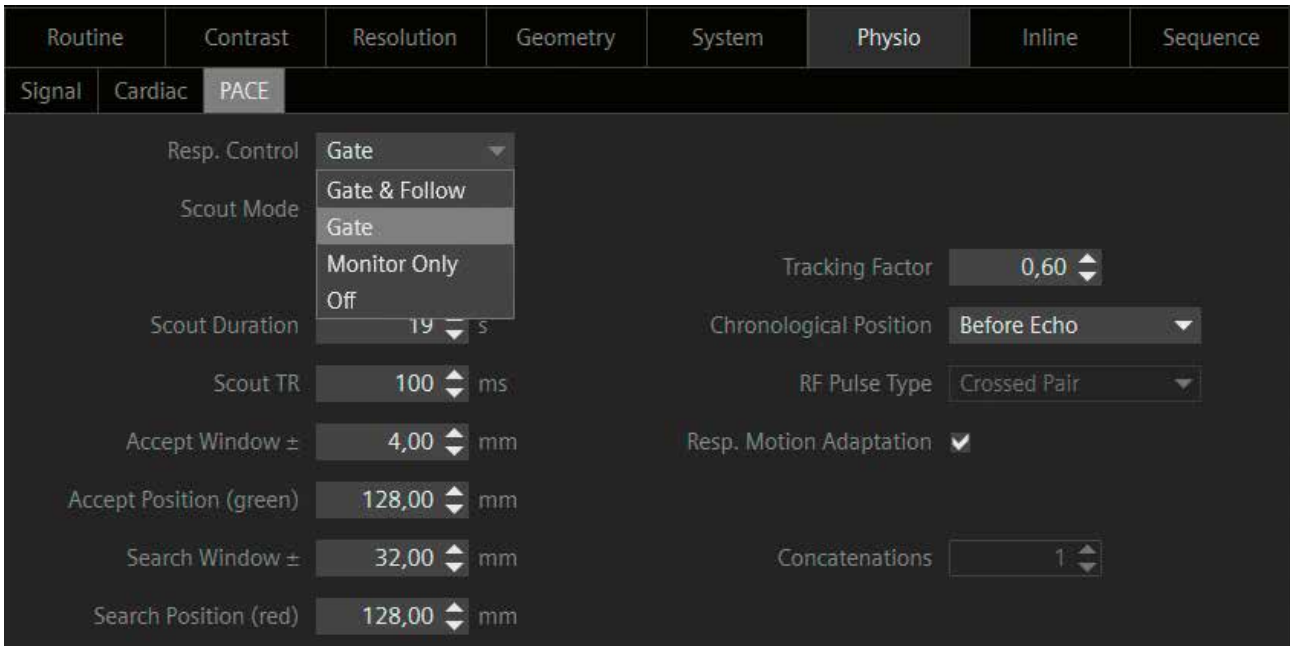

2 Respiratory gating options.

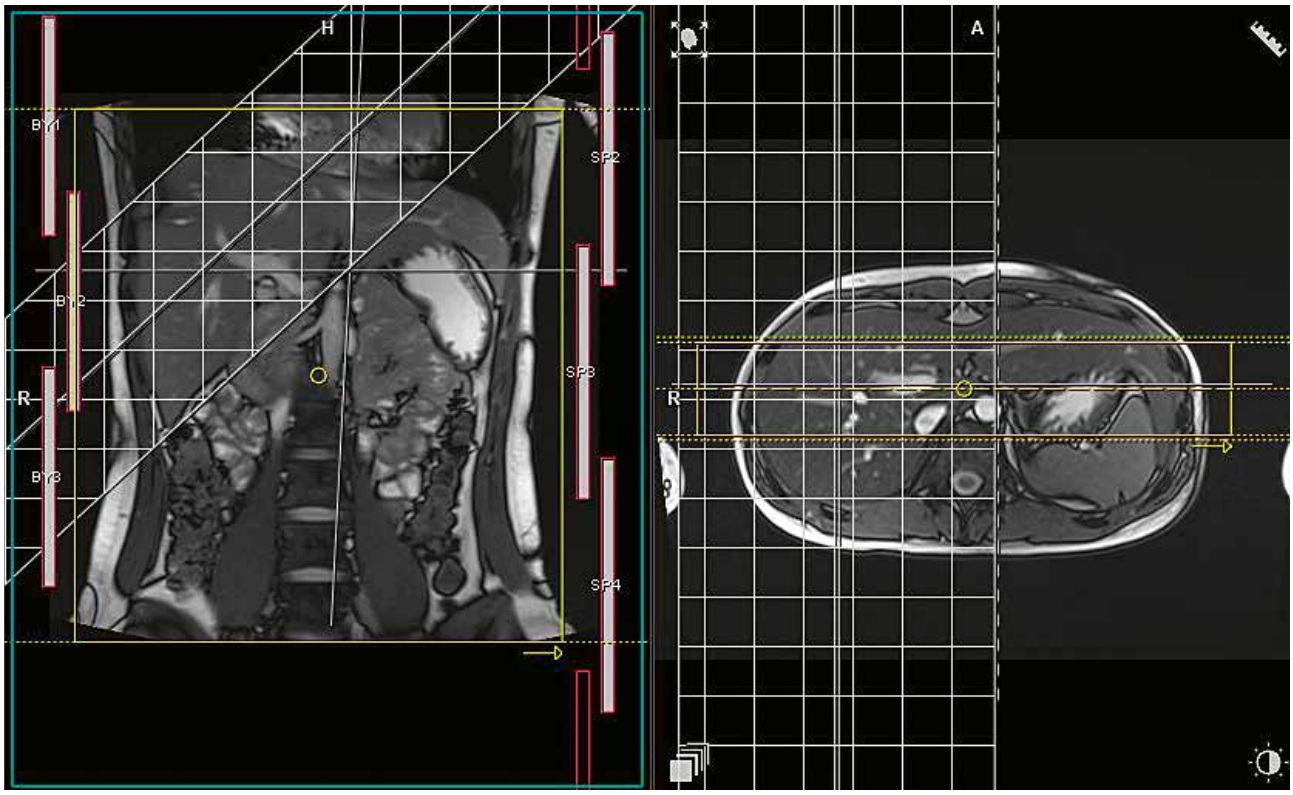

3 How to position the slices and the inversion graphics.

Some sequence adjustments are needed. Change the acquisition orientation to coronal. Increasing the slice thickness to 1.5 mm helps to get more signal. The inversion graphics and the inversion time (TI) values are important. We used two inversion graphics positioned diagonally to the liver and perpendicular to the portal vein (Fig. 3). At 1.5T, we set the TI value at 1500 ms. Depending on the size of the patient, you can increase the slice oversampling. The sequence can be modified to be bright blood with Trufi 3D (Fig. 4), or dark blood with GRE_3d (Fig. 5). Changing the sequence type is easy to do on the sequence tab (Fig. 6).

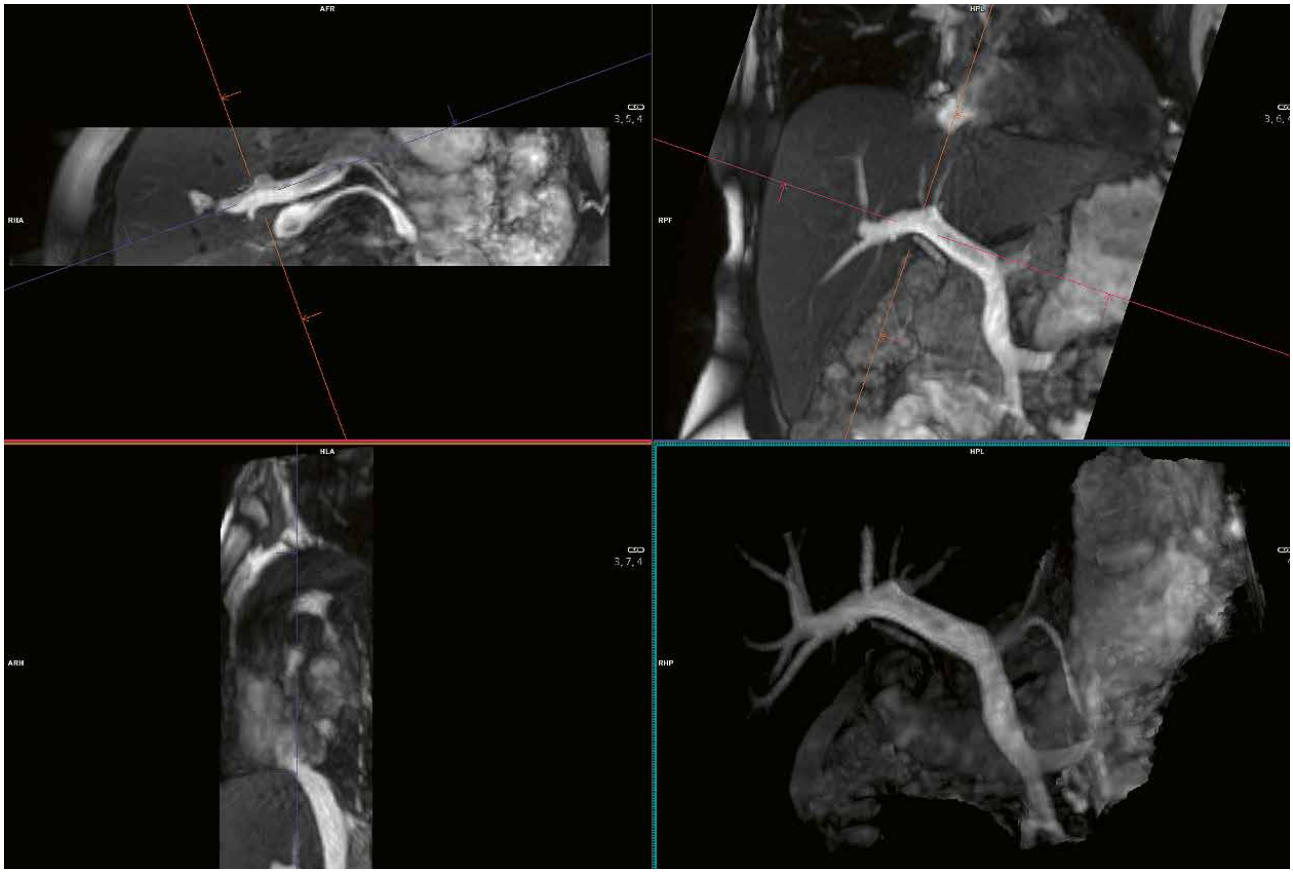

Study ID: 1aaaa6381

4 The sequence can be modified to be bright blood with Trufi 3D. Images acquired on a 1.5T MAGNETOM Sola.

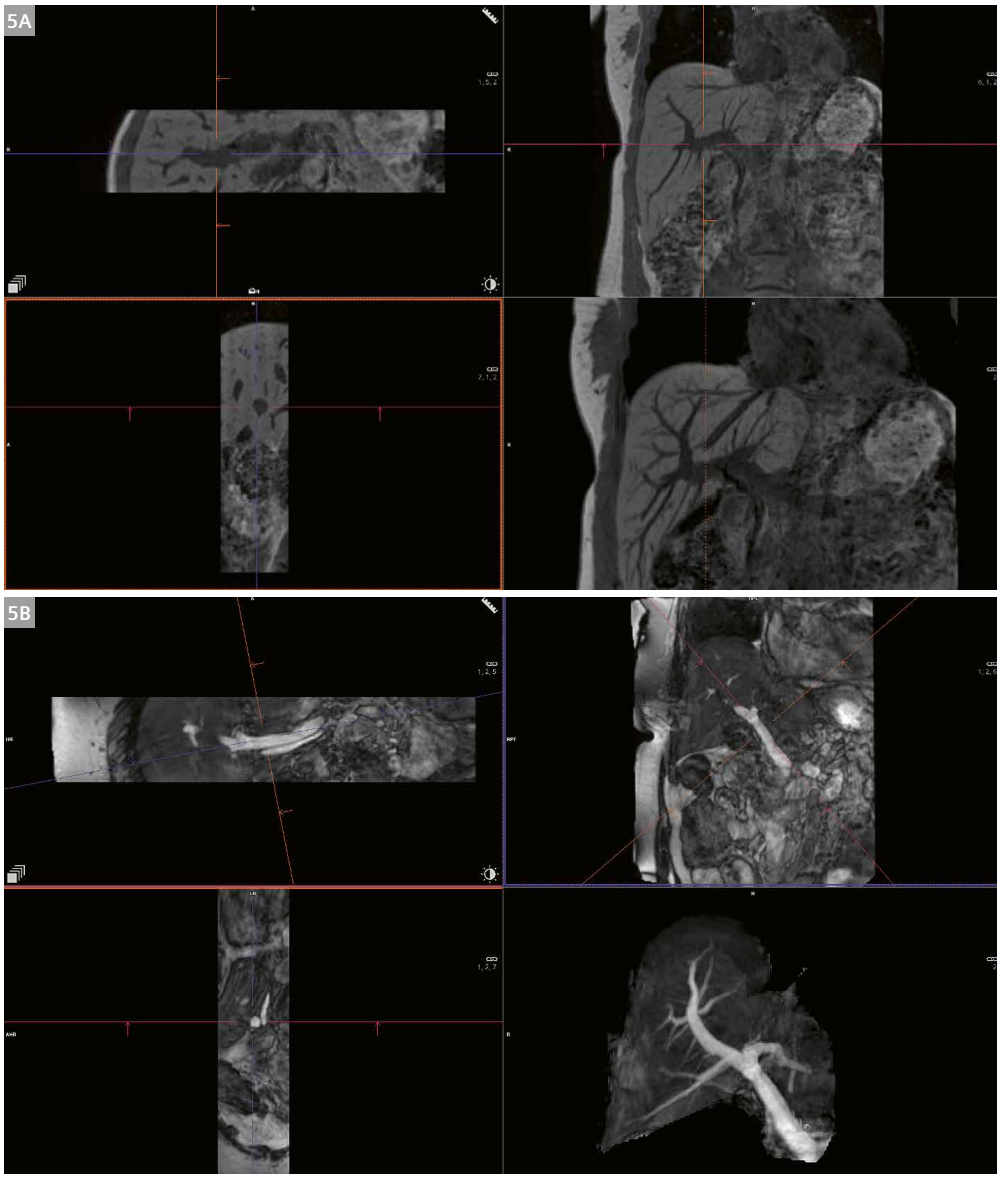

Study ID: 1aaaa6442

5 The sequence can be modified to be dark blood with GRE_3d MR. Images acquired on a 1.5T MAGNETOM Sola **(5A)** and MAGNETOM Flow **(5B)**.

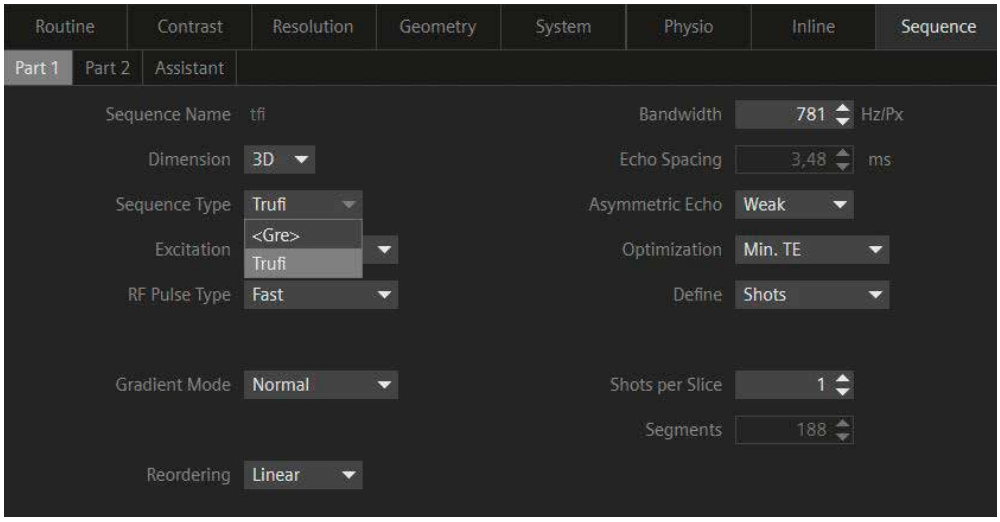

6 Changing the sequence between Trufi and GRE.

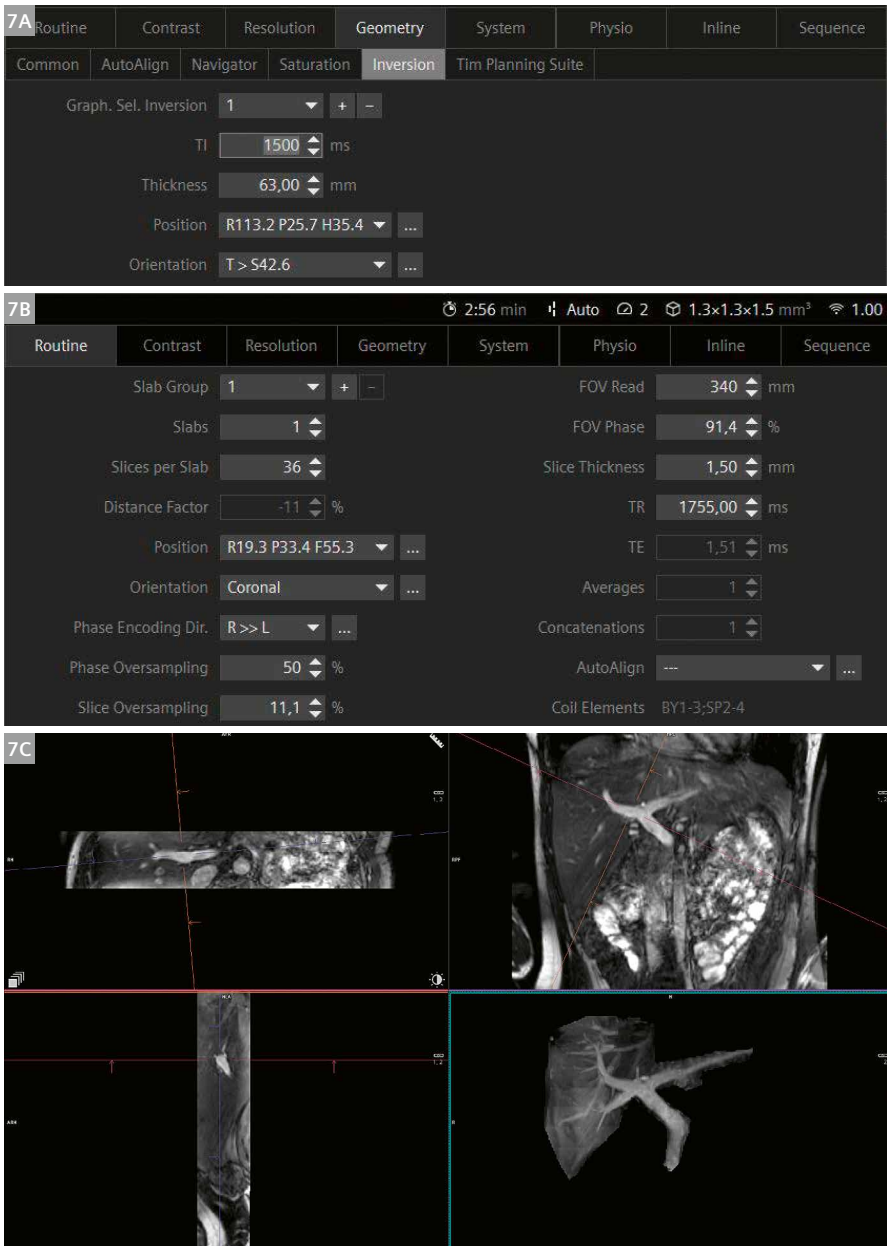

7 The MAGNETOM Lumina 3T protocol.

Study ID: 2aaaa4901

Conclusion

Native non-contrast MRI of the portal vein is a useful addition to abdominal MRI at 1.5T. With careful planning, patient coaching, and source-image review, the technique can provide clinically relevant information about portal venous patency and anatomy.

Contact

Marcelo Fernandes Arêas
Siemens Healthineers
SHS DI MR M&S S CVP
Allee am Röthelheimpark 2
91052 Erlangen
Germany
marcelo.areas@siemens-healthineers.com

References

1 Ohno T, Isoda H, Furuta A, Togashi K. Non-contrast-enhanced MR portography and hepatic venography with time-spatial labeling inversion pulses: comparison at 1.5 Tesla and 3 Tesla. Acta Radiol Open [Internet]. 2015;4(5):2058460115584110. Available from: http://dx.doi.org/10.1177/2058460115584110

2 Lee CH. Portal vein thrombosis on unenhanced MRI: a case series. BJR Case Rep [Internet]. 2022;9(1):20220059. Available from: http://dx.doi.org/10.1259/bjrcr.20220059

Meet Siemens Healthineers

Siemens Healthineers: Our brand name embodies the pioneering spirit and engineering expertise that is unique in the healthcare industry. The people working for Siemens Healthineers are totally committed to the company they work for, and are passionate about their technology. In this section we introduce you to colleagues from all over the world — people who put their hearts into what they do.

Jing An, MS

Jing An did not arrive at MRI from a single straight path. She first trained in clinical medicine and worked in cardiology, then later studied computer science. Looking back, that combination turned out to be a good fit for MRI: It gave her a way to think about patients and physiology, but also about signals, sequences, and how technology is actually built.

At Siemens Shenzhen Magnetic Resonance Ltd., she works closely with clinical partners on advanced MR applications. Over the years, she has supported many research collaborations, including work-in-progress sequences, external system testing, cardiovascular MRI education, and early 7T MRI activities in China. What she values most is not only the number of papers and abstracts that came out of these collaborations, but also the process of helping a clinical idea become something that can be tested, discussed, and improved.

How did you first come into contact with MRI?
I came to MRI through cardiology, so at the beginning I was not thinking only about images. I was thinking about what those images could tell us about the heart. When I worked in New York, I had the chance to develop pulse sequences for myocardial perfusion and pulmonary function analysis. That was when I really started to appreciate MRI. It is very technical, of course, but it is never just technology. A small change in a sequence or protocol can change what we are able to understand clinically.

What do you find motivating about your job?
For me, the interesting part is usually not the perfect final result, but the questions that come before it. A collaborator may say, "We want to see this more clearly" or, "This protocol is difficult in our patients." Then we need to understand whether the issue is timing, motion, contrast, workflow, or something else. I like that kind of problem-solving. It is practical, but it also keeps you learning.

What are the biggest challenges in your job?
The difficult part is that the same technical answer does not work everywhere. One site may be very experienced with coronary MR angiography, while another may be starting with stress perfusion or lung imaging. Even when the topic is familiar, the scanner, patient group, team experience, and research goal can be different. I have learned that collaboration starts with listening carefully. Before giving suggestions, you have to understand what the partner is really trying to achieve and what limitations they face in their daily work.

What do you think are the most important developments in MRI?
To me, a key development is the integration of AI across the entire MRI workflow. It is exciting because AI is not only about improving images after the scan. It can also support sequence design, scan planning, acquisition, reconstruction, and post-processing, helping make MRI faster, more robust, and easier for clinical teams to use. This is especially meaningful in cardiovascular MRI. I have seen how valuable techniques like free-breathing imaging, stress perfusion, vessel wall imaging, and non-contrast angiography can be, but also how demanding they are in daily practice. AI may help shorten scan times, handle motion better, improve image quality, and make quantitative analysis less manual.

What would you do if you could spend a month doing whatever you wanted?
I would probably keep it very simple. I would read more, take a slow trip somewhere, and spend proper time with family and friends — sharing good meals, taking walks, and simply being happy without always checking the next thing on my calendar. Work can easily become a series of meetings, questions, and problems to solve. Having a quiet month away from that rhythm would give me time to pause, look back on what I have learned, and think about what I still care about. I hope I would come back not only rested, but also a little clearer about where to put my energy next.

Not for distribution in the US

On account of certain regional limitations of sales rights and service availability, we cannot guarantee that all products included in this brochure are available through the Siemens Healthineers sales organization worldwide. Availability and packaging may vary by country and is subject to change without prior notice. Some/All of the features and products described herein may not be available in the USA.

The information in this document contains general technical descriptions of specifications and options as well as standard and optional features which do not always have to be present in individual cases, and which may not be commercially available in all countries. Due to regulatory reasons their future availability cannot be guaranteed. Please contact your local Siemens Healthineers organization for further details.

Siemens Healthineers reserves the right to modify the design, packaging, specifications, and options described herein without prior notice. Please contact your local Siemens Healthineers sales representative for the most current information.

Note: Any technical data contained in this document may vary within defined tolerances. Original images always lose a certain amount of detail when reproduced.

Siemens Healthineers Headquarters
Siemens Healthineers AG
Siemensstr. 3
91301 Forchheim, Germany
Phone: +49 9191 180
siemens-healthineers.com

Published by Siemens Healthineers AG · Order No. A91MR-01000-0010M-7600 · Printed in Germany · 18493 1026 · *©Siemens Healthineers AG, 2026*